UNIVERSITAT POLITÈCNICA DE CATALUNYA

Doctoral Programme:

AUTOMÀTICA, ROBÒTICA I VISIÓ

Doctoral Thesis:

Modelling and control of high-temperature proton exchange membrane fuel cells for combined heat and power comfort applications

Víctor Sanz i López

Advisors:

Ramon Costa Castelló, Dr.

Carles Batlle Arnau, Dr.

July 2022

Universitat Politècnica de Catalunya

Departament d'Enginyeria de Sistemes, Automàtica i Informàtica Industrial

Programa de doctorat:
Automàtica, Robòtica i Visió

Aquesta tesi ha estat realitzada a:

Institut de Robòtica i Informàtica Industrial, CSIC-UPC

Directors de tesi:
Dr. Ramon Costa Castelló i Dr. Carles Batlle Arnau

Als meus pares, Luis i Pilar, pels mals moments que els he fet passar.
Al meu germà Daniel, per haver estat tan injust amb ell.

Acknowledgement

To my supervisors, Ramon and Carles, for their patience during all these years. To Guillermo and David, for their work in the first simulations. To my office colleagues (Andreu, Anaís, Ricard, Carlos, Luis, Antonio, Alejandro, Yashan, Ali, Unni, Siro, Juan Pablo, Thomas and Tomás) for helping me solve so many technical problems during my thesis. To all those nice people I have met at IRI, specially those coming for lunch everyday to share our life experiences.

Resum

En aquesta tesi es presenta un model de sistema de gestió d'energia basat en control predictiu per a una casa específica alimentada per una pila de combustible amb membrana d'intercanvi de protons d'alta temperatura. Les piles de combustible i les tecnologies de cogeneració es mostren com una possible solució a causa de la seva capacitat de proporcionar energia elèctrica i tèrmica de forma més eficient en comparació amb els mètodes tradicionals. En relació amb això, les piles de combustible amb membrana d'intercanvi de protons d'alta temperatura ofereixen la possibilitat d'implementar sistemes que combinen energia elèctrica i tèrmica, essent a la vegada una tecnologia eficient i amb menors emissions de gasos d'efecte hivernacle.

Per a aquest propòsit, s'han desenvolupat i analitzat diferents models per a la pila de combustible, fins que se n'ha seleccionat un d'adequat per a la seva simulació juntament amb els altres elements del sistema de cogeneració. Els models dels elements dels sistema global de cogeneració, bateria elèctrica, acumuladors d'aigua, panell solar i electrolitzador, han estat dissenyats i combinats. Els panells solars s'han inclòs per alimentar un electrolitzador responsable de generar l'hidrogen per a la cel·la de combustible, mentre que la bateria elèctrica i els acumuladors d'aigua s'han implementat per assegurar el compliment de la demanda i la continuïtat del sistema al llarg del temps, ajudant pila de combustible a fer front als canvis bruscos de demanda. A més a més, s'han permès connexions a la xarxa en cas de necessitat puntual, així com una certa generació de calor a partir d'energia elèctrica. A continuació, es presenten models per la simulació i control del sistema, juntament amb les dimensions i els perfils d'energia utilitzats. Es detallen els objectius de control i l'algorisme de control proposat, i es discuteixen els resultats quan intentant seguir la demanda elèctrica i tèrmica, intentant a la vegada garantir l'eficiència energètica i reduir la degradació de les piles de combustible.

Finalment, es detalla un procés d'ajust de paràmetres basat en fronts de Pareto per donar prioritat a alguns objectius per sobre d'altres i s'obtenen els resultats del sistema global per a una casa prototipus simulada en diferents escenaris. Aquests escenaris han estat seleccionat basant-se en diferents períodes de l'any amb diferents exigències tèrmiques i condicions climàtiques, afectant tant les demandes com el funcionament del panell solar.

Abstract

In this thesis, a model predictive control-based energy management system for a specific house powered by a high temperature proton exchange membrane fuel cell is presented. Fuel cells and combined heat and power technologies are presented as a possible solution due to their ability to provide both electrical and thermal energy more efficiently compared to traditional methods. Related to this, high temperature proton exchange membrane fuel cells offer the possibility of implementing combined heat and power systems, and they are also considered an efficient technology that emits less greenhouse gases.

For this purpose, different models for the fuel cell are developed and analysed, until one suitable for simulation together with the other elements is selected. Models for elements in the whole combined heat and power system are designed and combined, that is, electrical battery, water accumulators, solar panel and electrolyser. Solar panels have been included to feed an electrolyser responsible of generating hydrogen for the fuel cell, while the electrical battery and a water accumulator have been implemented to ensure demand and thermal continuity along time, helping the fuel cell when dealing with abrupt demand changes. Additionally, grid connections have been allowed in case of punctual need, as well as a certain heat generation from electrical power. Simulation and control models of the system are presented, together with dimensions and energy profiles used. Control objectives and the proposed control algorithm are detailed, and the results when trying to match residential heat and power demands are discussed, while trying to ensure energy efficiency and reduce fuel cell degradation.

Finally, a tuning process based on Pareto fronts is studied to prioritise some objectives above others and the global system results are obtained for a typical simulated house in different scenarios. These scenarios have been selected based on different peri-

ods of the year with different thermal demands and climatic conditions, affecting both demands and solar panel operation.

Contents

List of Tables

List of Figures

Glossary

Acronyms

LT: Low temperature
HT: High temperature
PEMFC: Proton exchange membrane fuel cell
LT-PEMFC: Low-temperature proton exchange membrane fuel cell
HT-PEMFC: High-temperature proton exchange membrane fuel cell
DMFC: Direct methanol fuel cell
AFC: Alkaline fuel cell
PAFC: Phosphoric acid fuel cell
MCFC: Molten carbonate fuel cell
SOFC: Solid oxyde fuel cell
ECSA: Electrochemical active surface area
SOC: State of charge of a battery or other storage element
CHP: Combined heat and power
PI: Proportional-integral
PID: Proportional-integral-derivative
MPC: Model predictive control

Distributed fuel cell model's variables

V_N: Reversible Nernst potential [V]
Δg_f^0: Gibbs free energy to form a mole of vapour water [kJ/mol]
R: ideal gas constant [J/(K mol)]

F: Faraday's constant [C/mol]

T: Temperature [K]

P_{H_2}: Hydrogen's partial pressure [Pa]

P_{O_2}: Oxygen's partial pressure [Pa]

P_{H_2O}: Water vapour's pressure [Pa]

Q_r: Heat released in an exothermic reaction [J/mol]

ΔS: Entropy variation in a reaction [J/(K mol)]

I: Electrical current [A]

S: Electrode area [m^2]

j: Electrode's current density [A/m^2]

V_{cell}: Fuel cell voltage [V]

η^a_{act}: Voltage drop due to the activation at the anodic electrode [V]

η^c_{act}: Voltage drop due to the activation at the cathodic electrode [V]

η^a_{ohm}: Voltage drop due to ohmic resistance [V]

η^a_{conc}: Voltage drop due to matter transport at the anodic electrode [V]

η^c_{conc}: Voltage drop due to matter transport at the cathodic electrode [V]

V_{stack}: Fuel cell stack voltage [V]

V^i_{cell}: Fuel cell i voltage [V]

N: Number of cells in a fuel cell stack

E^0: Fuel cell open circuit voltage [V]

E_N: Reversible Nernst potential [V]

P_0: Atmospheric pressure [Pa]

t: Time variable [s]

$c^A_{H_2}$: Hydrogen concentration on the anode channels [mol/m^3]

$c^A_{H_2O}$: Water vapour concentration on the anode channels [mol/m^3]

v^A: Anode gas velocity [m/s]

$\dot{n}^A_{H_2}$: Hydrogen molar flux density transferred to the gas diffusion layers [$mol/(m^2\ s)$]

$\dot{n}^A_{H_2O}$: Water vapour molar flux density transferred to the gas diffusion layers [$mol/(m^2\ s)$]

y: Dimension across the fuel cell, from anode to channel [m]

δ^A: Anode gas channel's height along direction y [m]

$\dot{n}^A_{H_2,in}$: Hydrogen molar flux densities at the anode channel inlet [$mol/(m^2\ s)$]

$\dot{n}^A_{H_2O,in}$: Water vapour molar flux density at the anode channel inlet [$mol/(m^2\ s)$]

p^A: Anode pressure [Pa]

K^A: Anode diffusion coefficient [m^2/(Pa s)]

z: Dimension along the fuel cell channel [m]

L_z: Fuel cell channel length [m]

p^{amb}: Ambient pressure [Pa]

$(\rho u)^A$: Internal energy of the anode channels [J/m^3]

$h_{H_2}(T^A)$: Hydrogen's molar enthalpy at anode temperature [J/mol]

$h_{H_2O}(T^A)$: Water vapour's molar enthalpy at anode temperature [J/mol]

λ^A: Heat conductivity on the anode [W/(m K)]

α_1: Fuel cell's internal heat transfer coefficient [W/(m^2 K)]

δ^A: Anode channels' width [m]

T^S: Fuel cell internal solid parts temperature [K]

$h_{H_2}(T^A_{in})$: Hydrogen's molar enthalpy at anode's inlet temperature [J/mol]

$h_{H_2O}(T^A_{in})$: Water vapour's molar enthalpy at anode's inlet temperature [J/mol]

$c_p^{H_2}$: Hydrogen's specific heat [J/(K mol)]

$c_p^{H_2O}$: Water vapour's specific heat [J/(K mol)]

$\nabla\chi^A_{H_2}$: Gradient of hydrogen's molar fraction in the anode channels

$\chi^A_{H_2}$: Hydrogen's molar fraction in the anode channels

$\chi^A_{H_2O}$: Water vapour's molar fraction in the anode channels

$\chi^{CA}_{H_2}$: Hydrogen's molar fraction in the anode catalyst layers

$\chi^{CA}_{H_2O}$: Water vapour's molar fraction in the anode catalyst layers

$D^{eff}_{H_2,H_2O}$: Effective diffusion coefficient of hydrogen through water vapour [m^2 s]

δ^{GA}: Anode's gas diffusion layer's width [m]

$D^{eff}_{H_2,k}$: Effective diffusion coefficient of hydrogen through chemical species k [m^2 s]

χ^A_k: k chemical species' molar fraction in the anode channels

$\dot{n}^A_k$: Chemical species k molar flux density [mol/(m^2 s)]

$D^{eff}_{H_2,H_2}$: Effective diffusion coefficient of hydrogen through hydrogen [m^2 s]

$D^{eff}_{H_2O,H_2O}$: Effective diffusion coefficient of water vapour through water vapour [m^2 s]

$D^{eff}_{H_2O,H_2}$: Effective diffusion coefficient of water vapour through hydrogen [m^2 s]

$\dot{n}^{AM}_{H_2}$: Hydrogen's molar flux density in the membrane (anode side) [mol/(m^2 s)]

$\dot{n}^{AM}_{H_2O}$: Water vapour's molar flux density in the membrane [mol/(m^2 s)]

r^A: Molar rate reacting in the anode [mol/(m^2 s)]

f^v: Catalyst platinum content coefficient

i_{A0}: Open-circuit anode current [A]

$p_{H_2,ref}$: Hydrogen's reference pressure [Pa]

$\Delta\Phi^A$: Protonic potential difference in the anode [V]

$\Delta\Phi^A_{ref}$: Protonic potential difference's reference value in the anode [V]

$c^C_{O_2}$: Oxygen concentration in the cathode channels [mol/m^3]

$c^C_{N_2}$: Nitrogen concentration in the cathode channels [mol/m^3]

$c^C_{H_2O}$: Water vapour concentration in the cathode channels [mol/m^3]

v^A: Cathode gas velocity [m/s]

$\dot{n}^C_{O_2}$: Oxygen molar flux density transferred to the gas diffusion layers [mol/(m^2 s)]

$\dot{n}^C_{N_2}$: Nitrogen molar flux density transferred to the gas diffusion layers [mol/(m^2 s)]

$\dot{n}^C_{H_2O}$: Water vapour molar flux density transferred to the gas diffusion layers [mol/(m^2 s)]

δ^C: Cathode gas channel's height along direction y [m]

$\dot{n}^C_{O_2,in}$: Oxygen molar flux density in the cathode channel inlet [mol/(m^2 s)]

$\dot{n}^C_{N_2,in}$: Nitrogen molar flux density in the cathode channel inlet [mol/(m^2 s)]

$\dot{n}^C_{H_2O,in}$: Water vapour molar flux density in the cathode channel inlet [mol/(m^2 s)]

p^C: Cathode pressure [Pa]

K^C: Cathode diffusion coefficient [m^2/(Pa s)]

$(\rho u)^C$: Internal energy of the cathode channels [J/m^3]

$h_{O_2}(T^C)$: Oxygen's molar enthalpy at cathode temperature [J/mol]

$h_{N_2}(T^C)$: Nitrogen's molar enthalpy at cathode temperature [J/mol]

$h_{H_2O}(T^C)$: Water vapour's molar enthalpy at cathode temperature [J/mol]

λ^C: Heat conductivity on the cathode [W/(m K)]

δ^C: Cathode channels' width [m]

$h_{O_2}(T^C_{in})$: Oxygen's molar enthalpy at cathode's inlet temperature [J/mol]

$h_{N_2}(T^C_{in})$: Nitrogen's molar enthalpy at cathode's inlet temperature [J/mol]

$h_{H_2O}(T^C_{in})$: Water vapour's molar enthalpy at cathode's inlet temperature [J/mol]

$c_p^{O_2}$: Oxygen's specific heat [J/(K mol)]

$c_p^{N_2}$: Nitrogen's specific heat [J/(K mol)]

$\nabla\chi^C_{O_2}$: Gradient of oxygen's molar fraction in the cathode channels

$\chi^C_{O_2}$: Oxygen's molar fraction in the cathode channels

$\chi^C_{N_2}$: Nitrogen's molar fraction in the cathode channels

$\chi^C_{H_2O}$: Water vapour's molar fraction in the cathode channels

$\chi_{O_2}^{CC}$: Oxygen's molar fraction in the cathode catalyst layers

$\chi_{N_2}^{CC}$: Oxygen's molar fraction in the cathode catalyst layers

$\chi_{H_2O}^{CC}$: Water vapour's molar fraction in the cathode catalyst layers

D_{O_2,H_2O}^{eff}: Effective diffusion coefficient of oxygen through water vapour [m^2 s]

D_{N_2,H_2O}^{eff}: Effective diffusion coefficient of nitrogen through water vapour [m^2 s]

D_{O_2,N_2}^{eff}: Effective diffusion coefficient of oxygen through nitrogen [m^2 s]

D_{O_2,H_2O}^{eff}: Effective diffusion coefficient of nitrogen through oxygen [m^2 s]

δ^{GC}: Cathode's gas diffusion layer's width [m]

$D_{O_2,k}^{eff}$: Effective diffusion coefficient of oxygen through chemical species k [m^2 s]

χ_k^C: k chemical species' molar fraction in the cathode channels

$\dot{n}_k^C$: Chemical species k molar flux density [mol/(m^2 s)]

D_{O_2,O_2}^{eff}: Effective diffusion coefficient of oxygen through oxygen [m^2 s]

D_{H_2O,O_2}^{eff}: Effective diffusion coefficient of water vapour through oxygen [m^2 s]

$\dot{n}_{O_2}^{CM}$: Oxygen's molar flux density in the membrane [mol/(m^2 s)]

$\dot{n}_{H_2O}^{CM}$: Water vapour's molar flux density in the membrane (cathode side) [mol/(m^2 s)]

r^C: Molar rate reacting in the cathode [mol/(m^2 s)]

ΔG_0: Gibbs free energy of the open-circuit reaction [J/mol]

T^{ref}: Reference temperature [K]

i_{C0}: Open-circuit cathode current [A]

$p_{O_2,ref}$: Oxygen's reference pressure [Pa]

α: Stoichiometric adjusting coefficient

$\Delta\Phi^C$: Protonic potential difference in the cathode [V]

$\Delta\Phi_{ref}^C$: Protonic potential difference's reference value in the cathode [V]

$\dot{n}_{H+}$: Proton flux density [mol/(m^2 s)]

k: Fuel cell's electrode electrical conductivity [C]

$\nabla\mu_{H+}$: Gradient of proton electrical potential [J/mol]

$\Delta\Phi^M$: Membrane potential difference [V]

δ^M: Membrane's width [m]

i^M: Membrane's electrical current density [A/m^2]

$(\rho e)^S$: Fuel cell's total energy [J/m^3]

δ^S: Fuel cell's internal solid part's width [m]

α_2: Fuel cell's internal heat transfer coefficient [W/(m^2 K)]

λ^S: Fuel cell's internal solid part's heat conduction coefficient [W/(m K)]

C^A: Anode's capacity [F/m^3]

C^C: Cathode's capacity [F/m^3]

δ^{AC}: Anode catalyst layers' width [m]

δ^{CC}: Cathode catalyst layers' width [m]

$\Delta\Phi^A$: Anode's protonic potential difference [V]

$\Delta\Phi^C$: Cathode's protonic potential difference [V]

$\Delta\Phi^C$: Membrane's protonic potential difference [V]

$(\rho u)^S$: Solid parts' internal energy [J/m^3]

$(\rho h)^S(T^S)$: Solid parts' enthalpy [J/m^3]

$(\rho h)^S(T^S)$: Total enthalpy in the membrane [J/m^3]

$\rho^M_{H_2O} h_{H_2O}(T^S)$: Water vapour's enthalpy in the membrane [J/m^3]

U: Fuel cell voltage difference [V]

I: Fuel cell total current [A]

x: Fuel cell's third direction [m]

L_x: Fuel cell's length along x direction [m]

P: Fuel cell's electrical power [V]

T_{cool}: Coolant temperature [K]

Simulation model's variables

E_{oc}: Fuel cell's open circuit voltage [V]

K_c: Voltage constant at nominal condition of operation

E_n: Nernst voltage [V]

i_0: Fuel cell's exchange current [A] z: Number of moles of moving electrons in the fuel cell reaction [mol]

k: Boltzmann's constant [J/K]

h: Planck's constant [Js]

Δv: Reaction's activation barrier volume factor [m^3]

ΔG: Size of the reaction's activation barrier [J/mol]

T: Fuel cell temperature [K]

U_{fH_2}: Hydrogen conversion rate

U_{fO_2}: Oxygen conversion rate

χ_w: Water's molar fraction

P_{fuel}: Fuel pressure [Pa]

P_{air}: Air pressure [Pa]

i_{fc}: Fuel cell current [A]

$V_{lpm(fuel)}$: Fuel flow rate [l/min]

$V_{lpm(air)}$: Air flow rate [l/min]

N: Number of cells in the stack

E_{pre}: Fuel cell's internal voltage [V]

U_{fc}: Fuel cell voltage [V]

T_d: Time delay for computational reasons [s]

μ_{conv}: Electrical converter's efficiency

U_{out}: Voltage going out of the electrical converter [V]

I_{out}: Current going out of the electrical converter [A]

U_{in}: Voltage going into the electrical converter [V]

I_{in}: Current going into the electrical converter [A]

N_c: Number of fuel cells in the stack

$n_{H_2,comp}$: Number of hydrogen moles in the fuel composition [mol]

$n_{H_2,used}$: Number of hydrogen moles used in the reaction [mol]

U_{El}: Electrolyser voltage [V]

I_{El}: Electrolyser current [A]

$I_{El,0}$: Electrolyser's open-circuit current [A]

E_{oc}; Electrolyser's open-circuit voltage [V]

N_e: Electrolyser layers

A_e: Electrolyser's active area [m^2]

τ: Electrolyser's time constant for computational reasons [s]

U_{PV}: Solar panel voltage [V]

R_{sh}: Solar panel's shunt resistance [Ω]

R_s: Solar panel's resistance [Ω]

I_L: Solar panel's internal current [A]

I_d: Solar panel's internal diode's current [A]

I_{PV}: Solar panel's output current [A]

E_0: Battery's open-circuit voltage [V]

Q: Battery capacity [Ah]

Q_{max}: Maximum battery capacity [Ah]

I_{batt}: Battery current [A]

I^*_{batt}: Low frequency current dynamics in the battery [A]

K: Battery's polarisation constant [V/Ah]

A: Battery's exponential voltage [V]

B: Battery's exponential capacity [A/h]

U_{batt}: Battery voltage [V]

E_{batt}: Nonlinear internal voltage in the battery [V]

R_i: Battery internal resistance [Ω]

T^{oil}_{acc}: Oil accumulator temperature [K]

m^{oil}_{tank}: Oil mass in the accumulator [kg]

c^{oil}_p: Oil's specific heat [J/(K kg)]

$P_{t,fc}$: Heat generated by the fuel cell [W]

$T^{H_2O}_{tank}$: Water accumulator temperature [K]

K_{exch}: Oil tank exchange losses constant [W/m]

μ_{exch}: heat exchanger's efficiency

Q_{HW}: Power corresponding to hot water extracted from the accumulator [W]

K_{env}: Environment losses constant [K/W]

T_{env}: Environment temperature [K]

Q_{loss}: Thermal energy exchange between the house and the environment [J]

T_{house}: Internal temperature of the house [K]

T_{out}: External temperature of the house [K]

R^{house}_{eq}: Equivalent thermal resistance of the house [K/W]

M_{air}: Mass of air inside the house [kg]

Q_{heater}: Heater's thermal energy [J]

T_{heater}: Heater temperature [K]

$\dot{M}$: Air mass flow rate through the heater [kg/s]

I_{load}: Load current [A]

Q_c: Capacitor's charge [C]

C: Capacitor's capacity [F]

U_c: Capacitor voltage [V]

$\dot{m}_{HW}$: Mass flow extracted from the water accumulator for consumption needs [kg/s]

Control and mathematical variables

$\mathbf{x}(t)$: Vector of state variables

$f|_{z,t}$: Evaluate function f at dimension value z and time

$x(i)$: Value of variable x at node i

$\overrightarrow{\mathbf{x}}$: Vector of fuel cell's state variables

$\mathbf{A}$: State matrix in a state-space representation

$\mathbf{B}$: States-inputs matrix in a state-space representation

$\mathbf{C}$: Outputs-states matrix in a state-space representation

$\mathbf{D}$: Outputs-inputs matrix in a state-space representation

$\mathbf{x}(t)$: State variables in a state-space representation

$\mathbf{u}(t)$: Input variables in a state-space representation

$\mathbf{y}^*$: Output's equilibrium value in a state-space representation

$\mathbf{x}^*$: State's equilibrium value in a state-space representation

$\mathbf{u}^*$: Input's equilibrium value in a state-space representation

$\mathbf{y}^*$: Output's equilibrium value in a state-space representation

λ_i: Matrix's eigenvalue number i

$\mathbf{M_{con}}$: Controllability matrix

$\mathbf{M_{obs}}$: Observability matrix

U^*: Fuel cell voltage's equilibrium point [V]

T^*_{cool}: Coolant temperature's equilibrium point [K]

N_{total}: Prediction horizon

f_i: Subfunction summarising control objective i

$\mathbf{x}_k$: State vector at instant k

$\mathbf{u}_k$: Input vector at instant k

$u_{k,i}$: i-component of the control input vector at instant k

e_k: Variable governing control system's energy

$I_{fc,max}$: Upper boundary for the fuel cell current [A]

$I_{fc,min}$: Lower boundary for the fuel cell current [A]

P^{max}_{tra}: Upper boundary for the electrical energy transferred to thermal [J]

P^{min}_{tra}: Lower boundary for the electrical energy transferred to thermal [J]

$P^{max}_{e,loss}$: Upper boundary for the electrical energy [J]

$P^{max}_{t,loss}$: Upper boundary for the thermal energy [J]

w_i: Weight function corresponding to control objective i

$J(\mathbf{x}_k, \mathbf{u}_k)$: Objective function

E_{elec}^{bat}: Stored electrical energy in the battery [J]

E_{therm}^{acc}: Stored thermal energy in the water accumulator [J]

I_{fc}: Fuel cell current [A]

W_{tra}: Electrical to thermal energy transfer variable if necessary for demand purposes [J]

$W_{grid_{in}}$: Electrical energy supplied by the grid if necessary [J]

$W_{grid_{out}}$: Electrical energy supplied to the grid if necessary [J]

$W_{accum_{out}}$: the accumulator if necessary [J]

$W_{d_{elec}}$: Electrical demand considered as perturbation [J]

$W_{d_{therm}}$: Thermal demand considered as perturbation [J]

K_{env}: Environment losses constant

T_s: MPC's sampling time [s]

m_{acc}: Water mass in the accumulator [kg]

C_{H_2O}: Water's specific heat [J/(kg K)]

η_{conv}: Converter efficiency

η_{exch}: Heat exchanger efficiency

η_{tra}: Electrical to thermal transfer efficiency

V_{fc}^{nom}: Electrical fuel cell voltage due to linearisation [V]

V_q^{nom}: Thermal voltage due to linearisation [V]

$dI_{fc,max}$: Fuel cell current variation limit [A]

$E_{e,max}$: Upper boundary for the electrical energy [J]

$E_{e,min}$: Lower boundary for the electrical energy [J]

$E_{t,max}$: Upper boundary for the thermal energy [J]

$E_{t,min}$: Lower boundary for the thermal energy [J]

$E_{e,hlim}$: Soft constraint's higher limit for the electrical energy [J]

$E_{e,llim}$: Soft constraint's lower limit for the electrical energy [J]

$Batt_{ll}$: Battery current's lower limit [A]

$Batt_{hl}$: Battery current's higher limit [A]

$Accu_{hl}$: Water accumulator's thermal energy stored higher limit [J]

y_k Binary variable to implement soft constraints

$\mathbf{d}_k$: Perturbation vector

D_{elec}: Electrical demand [J]

D_{therm}^{HW}: Thermal demand for hot water purposes [J]

D_{therm}^{SH}: Thermal demand for space heating purposes [J]

$\hat{\mathbf{d}}_{k+i}$: Expected perturbation value for i iterations in the future

$\hat{\mathbf{x}}_{k+i}$: Expected state value for i iterations in the future

k: Current iteration instant

f_C: Objective function to minimise fuel cell current

f_{CV}: Objective function to minimise fuel cell current variation

f_{C+CV}: Objective function to minimise fuel cell current plus its variation

f_{SC}: Objective function to minimise violating soft constraints in the ancillary systems

f_{SE}: Objective function to minimise activation of security elements (ancillary systems)

f_C: Weight function to minimise fuel cell current

f_{CV}: Weight function to minimise fuel cell current variation

W_{C+CV}: Weight function to minimise fuel cell current plus its variation

W_{SC}: Weight function to minimise violating soft constraints in the ancillary systems

W_{SE}: Weight function to minimise activation of security elements (ancillary systems)

Chapter 1

Introduction

Experience, though noon auctoritee

Were in this world, is right ynough for me

From *The Canterbury Tales*, by Geoffrey Chaucer

Potential energy shortage and issues caused by climate change are among the first problems nowadays, as various international institutions highlight. For instance, a recent increase of 2.5% in primary energy consumption has been reported [30]. These studies also highlight last decade's increase in coal consumption up to a maximum of 29.9% of world's primary energy, corresponding to year 2012. Simultaneously, consequences of natural disasters that led to Fukushima's nuclear power plant accident, forced the Japanese government to move away from nuclear energy, reducing its dependence by 89% (6.9% around the world). Knowing that coal-fired power plants are able to reach efficiencies up to 41% reducing heat waste rate appears as a key goal to envisage in the immediate future, both from a technological and economical viewpoint.

In reaction to this, political authorities are being forced to look for alternatives that deal with waste energy management while they operate. In the case of residential applications, energy consumption represents 27% of the electrical energy and 38% of the thermal energy consumed globally. The specific usage of this energy changes from one country to the other. Some examples of residential energy usage can be seen in Figure 1.1.

In this context, combined heat and power (CHP) has arisen as a promising option

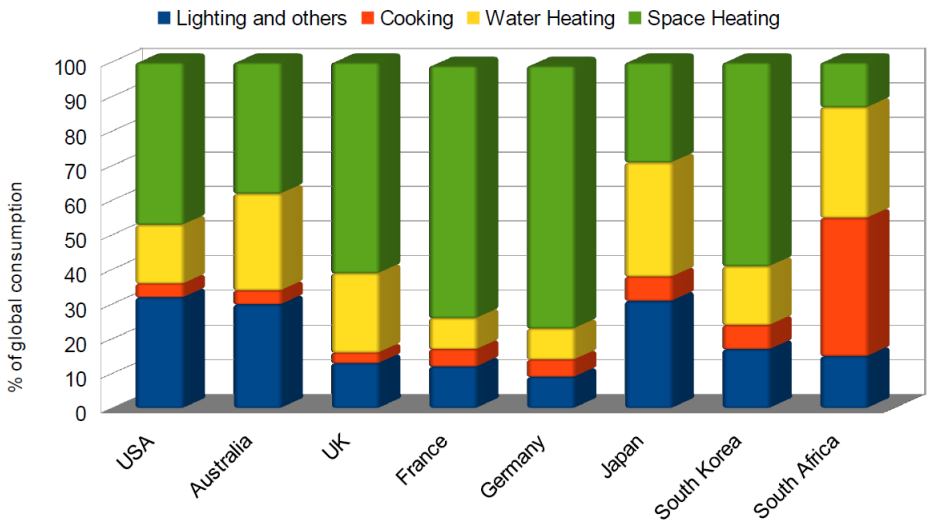

Figure 1.1: Residential energy usage in different countries [30]

due to its ability to use both electrical and thermal energy. Among the different kinds of CHP technologies, fuel cells are one of the main options being proposed as a way of changing part of the world's energy generating system. This thesis focuses specifically on high-temperature proton exchange membrane fuel cells (HT-PEMFC) and, more precisely, the chemical and physical principles behind them and their technical specifications.

1.1 Motivation

In this state of events, what is called "green hydrogen" [48], consisting on using hydrogen as fuel, represents a sustainable solution to replace traditional energy sources in their applications. This hydrogen is produced using electrolysers able to split water into hydrogen and oxygen. These electrolysers need electrical energy to operate, so this should also come from sustainable energy sources, like solar panels, thus forming a cycle between solar panel, electrolyser and hydrogen fuel cells to operate residential applications.

Fuel cells are seen as a possible solution to replace traditional energy sources in many applications of this kind [48]. This is because, apart from generating electrical energy, as it is their supposed role, high-temperature fuel cell technologies release heat

resulting from the operation, something that can be used for heating. Systems using this heat released for practical applications are known as combined heat and power (CHP) systems, and represent an option to lead with energy waste and increase efficiency. Among different CHP systems, fuel cells are seen as a tool for helping the global energy system to reshape [61]. The current article focuses on high-temperature proton exchange membrane fuel cells (HT-PEMFC) and, specifically, their chemical and physical characteristics and technological issues specific to them.

1.2 Thesis objectives

The main goal of the proposed doctoral thesis is designing and implementing suitable control strategies for a combined heat and power PEM fuel cell system for residential usages. When studying fuel cells, several aspects are being taken into consideration. Among these aspects, the studied ones are:

- *Energy efficiency*: the main effort is driven towards reducing energy losses and avoiding extra internal consumption.
- *Lifetime*: mitigating the main causes of deterioration of the fuel cell systems.

For this reason, a control optimization index including terms for both fuel cell efficiency and lifetime needs to be included. Both properties are related and can not be optimised separately. For instance, output electrical power is increased imposing high voltages, which cause degradation of the fuel cell, or high current, implying higher hydrogen consumption. This high voltage affects the mechanical elements of the fuel cell thus reducing its lifetime expectancy. That is the reason why a combined optimization needs to be done. To sum up, the global objectives in this thesis are the following ones:

1. Defining a mathematical model to describe the fuel cell's behaviour. This model should be used to find an operation point and should be reduced afterwards to facilitate its manipulation and application to the CHP system.
2. Investigate different control techniques, presumably model predictive control (MPC), in order to stablish control from the CHP system to match the comfort specifications and favouring efficiency and degradation. Analyse whether this can be

done using a reduced order version of the original linearised system's model or a simplified version of it must be used.

3. Design a control index in the shape of an objective function including terms affecting the HT-PEMFC's degradation and its related variables such as cell voltage, current, temperature and gas flow. The selected variables included in this index must be available externally so that they can be manipulated and controlled.

4. Stablish energy (heat and electrical power) profiles to be achieved by the CHP-HT-PEMFC in an specific house so that the defined comfort conditions, specifically temperature, are met. This will allow to test the control system with real values when simulating the whole CHP system and come close to a real system accordingly.

5. Compare results to the ones expected for equivalent housing facilities. The global system includes HT-PEMFC, compressors, heat exchangers and other equipments used for CHP in housing facilities.

These objectives need to be fulfilled along the thesis and the following sections will cover them in an order similar to the one presented.

1.3 Thesis outline

This thesis has the following structure:

1. State of the art
2. High-temperature PEM fuel cell distributed model
3. Simulation model
4. Control system structure
5. Energy management strategy
6. System objectives' tuning using Pareto fronts
7. Results and discussion
8. Conclusions

Chapter 2

State of the art

Demonstratio longe optima est experientia.

From *Novum Organum*, by Francis Bacon

In this chapter, an overview of the current state of the research in the studied fields is presented. Among other topics, the current state of fuel cell technologies, more specifically their characteristics, modelling and control, as well as combined heat and power systems will be classified and explained.

2.1 Fuel cell technologies

A fuel cell (FC) is defined [43] as "an electrochemical converter which continuously converts the chemical energy from a fuel and an oxidant into electrical energy, heat and other reaction products". Both fuel and oxidant are continuously supplied and being consumed during the process. There exist different fuel cell technologies, classified according to its components, chemical reaction and operation temperature [43]. Each of these have different advantages and drawbacks that make them suitable for specific applications, stationary or non-stationary depending on the case. Table 2.1 summarises different fuel cell technologies and their characteristics:

Table 2.1: Fuel cell technologies and their characteristics

Type	Electrolyte	Temp. (°C)	Fuel	Advantages	Problems
Polymeric (PEMFC)	Polymeric membrane	30-100 (LT) 120-200 (HT)	H_2	- Fast start-up - Solid electrolyte	- Pure H_2 needed - Expensive catalyst
Direct Methanol (DMFC)	Polymeric membrane	30-100	CH_3OH	- Liquid fuel - No reforming step for fuel	- Slow reaction - Fuel crossover from anode to cathode
Alkaline (AFC)	KOH (liquid)	65-220	KOH	-Better current response (fast cathodic reaction)	- Reactants must be removed
Phosphoric Acid (PAFC)	H_3PO_4	150-220	H_2	- High efficiency with heat cogeneration	- Low power and current - Expensive catalysts
Molten Carbonate (MCFC)	Carbonates (Li, Na, K)	600-1000	H_2	- Better conductivity - High current density	- Slow start-up - Material problems
Solid Oxide (SOFC)	(Zr, Y) O_2	600-1000	H_2	- Solid electrolyte - Low cost material	- Material problems - Corrosion of metal

Regarding their applications, fuel cell technologies such as DMFC, AFC and other low-temperature technologies such as LT-PEMFC are useful for non-stationary applications like vehicles, portable devices and other. In the case of non-stationary applications such as vehicles, where fuel cells are used together with battery systems to replace traditional engines, only electrical energy is used, and heat is not used for heating inside the car, so it needs to be dissipated or cooled down. For this reason, LT-PEMFC are a preferable technology, as higher temperatures could cause problems in mechanical

elements involved in vehicle operation. Additionally, LT-PEMFC are better for vehicles, as they are more prepared for fast start-stop operation, as start-up is easier when operation temperature needed is easier to reach when this is low. On the other hand, high-temperature fuel cell technologies are mainly used for stationary applications where heat can be used for combined heat and power (CHP). These include industrial usages of MCFC or SOFC and residential usages such as those based on HT-PEMFC. This last application in housing facilities is the one explored and described in the following sections, focusing on HT-PEMFC modelling, residential CHP systems in particular and energy management strategies involved.

2.2 Proton exchange membrane fuel cells

In the case of PEMFC, several cells are usually assembled together to form a fuel cell stack, or simply known as fuel cell, which consists of different layers. These are presented as follows and the whole process is depicted in Figure 2.1:

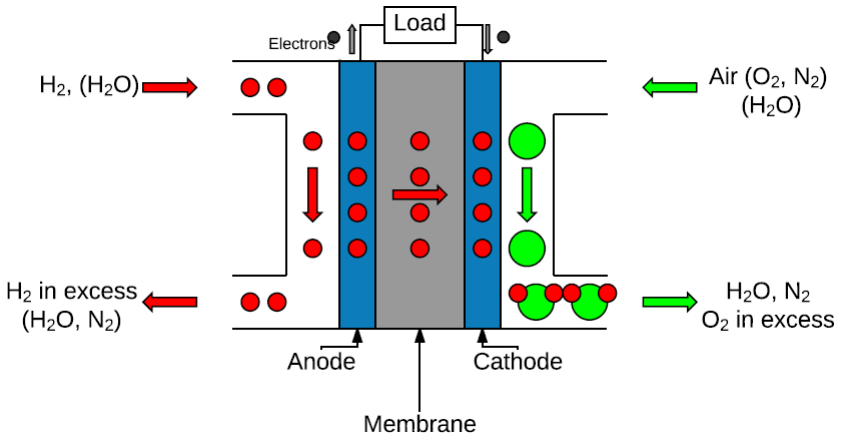

Figure 2.1: Fuel cell scheme

- *Anode*: corresponding to the left part of Figure 2.1. Fuel in the shape of gas goes through these pores to reach the interface with the electrolyte, responsible of conducting ions and place where fuel oxidises; electrons move across an external circuit, from anode to cathode.
- *Cathode*: corresponding to the right part of Figure 2.1. The oxidant goes through cathode's pores until the electrolyte's interface, where reduction takes place.

- *Membrane*: constituting an electrolyte, at the center of Figure 2.1, is responsible of conducting ions between electrodes.
- *Bipolar plates*: place where the anode and cathode channels are located, responsible of conveying electrons and reactants to the electrodes, as well as evacuating their excess and reaction's products. Heat released by the system needs to be handled adequately with additional devices.

These layers are sealed using silicon to prevent fluid leakages to form what is known as a fuel cell stack.

Pure hydrogen (H_2) is what is needed in the anode for PEMFC's reaction and oxygen and, as air is mainly composed by nitrogen and oxygen, can be directly fed into the cathode. Hydrogen oxidation occurs at the anode to produce protons (H^+) that are forced across the membrane connecting anode and cathode. At the same time, cathode receives electrons assembled by the mentioned bipolar plates. Reaction is accelerated using a catalyst such as platinum, whose active area is a key value to improve the process. This electrochemical active surface area (ECSA) should be increased and is one of the first elements to be degraded, as active parts are easily damaged or catalyst particles are lost during operation. Finally, it is at the cathode where protons and oxygen combine and generate water, as seen in Figure 2.1. Chemical redox semi-reactions corresponding to this process are [43]:

$$\mathrm{H_2} \longrightarrow 2\mathrm{H^+} + 2\mathrm{e^-}$$
$$\tfrac{1}{2}\mathrm{O_2} + 2\mathrm{e^-} + 2\mathrm{H^+} \longrightarrow \mathrm{H_2O}.$$

As a result of this process, electrical and thermal energy, as well as water, are produced. If process losses are neglected, reversible Nernst potential V_N is defined as presented in [43]:

$$V_N = -\frac{\Delta g_f^0}{2F} + \frac{R \cdot T}{2F} \ln\left(\frac{P_{H_2} P_{O_2}^{\frac{1}{2}}}{P_{H_2O}}\right), \tag{2.1}$$

where $\Delta g_f^0 = -228.59$ kJ/mol is the Gibbs free energy to form a mole of vapour water, $R = 8.31$ J/(K mol) is the ideal gas constant, $F = 96485.34$ C/mol is Faraday's

constant, T is the temperature, P_{H_2} is hydrogen's partial pressure, P_{O_2} is oxygen's partial pressure, P_{H_2O} is water vapour's pressure.

In terms of heat released by the fuel cell during its operation, there are several phenomena contributing to it [86]:

- Half reactions shown above have an entropy variation related to heat.
- The electrochemical reaction itself releases heat during its activation.
- Gas diffusion layers in the fuel cell, responsible of conveying gases from anode to the catalyst layer, undergo processes of sorption and desorption, contributing or diminishing heat released depending on the case.
- Heat is released in the electrical part of the system by Joule effect.
- Water phase change in the gas diffusion layer, in the case of low-temperature fuel cells, absorbs heat from the cell.

The global redox reaction is exothermic, meaning that it releases heat Q_r. This heat is connected to the reaction's entropy variation ΔS with the following relation:

$$Q_r = T\Delta S. \tag{2.2}$$

ΔS is calculated using formation entropies characteristic of each substance, i.e. hydrogen, water, oxygen and nitrogen. The relation between hydrogen flow and the electrical current, I, is directly proportional, so identifying a similar relation between current and released heat is also desired. However, in real applications, fuel cells present voltage drop in comparison with Nernst reverse voltage V_N, be it with or without load. This decreasing mainly causes losses in the cell to increase, causing problems in the short and long run. Issues related are described as follows:

- Redox reactions need an activation energy to start, specially important in low-current scenarios.
- Ion transport across the membrane, as well as electrodes involve ohmic resistance, neglected in the case of bipolar plates.

- There is a drop in voltage due to matter transport through porous electrodes, specifically gas diffusion layer. This phenomenon is specially harsh at high current and is related with current I, function of electrode's area S, considering current density j,

$$j = \frac{I}{S}. \tag{2.3}$$

A single cell voltage can be defined as:

$$V_{cell} = V^N - \eta^a_{act} - \eta^c_{act} - \eta_{ohm} - \eta^a_{conc} - \eta^c_{conc}, \tag{2.4}$$

where

- V^N is the Nernst reversible potential.
- η^a_{act} and η^c_{act} is the voltage drop provoked by the activation at the anodic and cathodic electrode respectively.
- η^a_{ohm} is the voltage caused by ohmic resistance.
- η^a_{conc} and η^c_{conc} are the voltage drop due to matter transport at the anodic and cathodic electrode respectively, also known as concentration losses.

As mentioned before, in real applications, voltage provided by a single cell is too low to be useful (less than 1 V). For this reason, it is common to arrange several cells in N-cell stack terminals. The amount of layers selected is, consequently, adapted to the specific application, depending on the voltage desired, space available for the fuel cell and other implementation issues. The resulting voltage of the whole stack must be defined accordingly, as seen in equation (2.5):

$$V_{stack} = \sum_{1}^{N} V^i_{cell} \tag{2.5}$$

The typical values for the nominal current density of the whole stack are between 0.5 and 1 A/cm^2 with a corresponding mean cell voltage around 0.7 V. The residual power obtained by Joule's effect as well as process heat represents a 37.5% of the output

energy released (30% of the energy supplied by the fuel) can be reused for the CHP system [30].

In order to characterise PEMFC's performance, a polarisation curve is defined [43], relating PEMFC's voltage versus current density. This polarisation curve changes depending on the operation temperature. This polarisation curve has activation losses as the dominant ones when current is low, concentration losses when current is high and ohmic losses for intermediate current values. Activation and concentration losses force an asymptotic tendency in the curve. An example of polarisation curve for a HT-PEMFC is depicted in Figure 2.2a, with current corresponding to a stack of 20 cells and an area of 1 cm^2 operating at a temperature of 127ºC. The same is done for the electrical and thermal power generated by a fuel cell, as seen in Figure 2.2b.

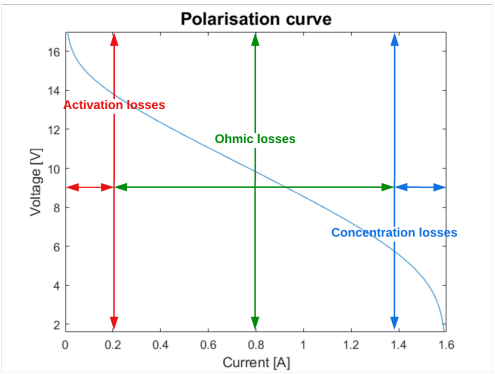

(a) Polarisation curve of a HT-PEMFC (20 cells, area of 1 cm^2 and temperature of 127ºC)

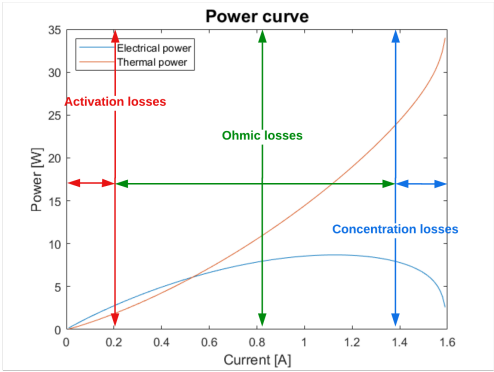

(b) Electrical and thermal power curves of a HT-PEMFC (20 cells, area of 1 cm^2 and temperature of 127ºC)

Regarding differences between low-temperature PEM fuel cells (LT-PEMFC) and their high-temperature counterparts (HT-PEMFC), they are mainly related to their operation temperature. While the former operate at 60-80ºC, the latter work between 120ºC and 200ºC [43]. Advantages and drawbacks of these technologies when comparing them are:

- Generation of liquid water in the case of LT-PEMFC causes problems when managing this water and its distribution along the system. In LT-PEMFC, membrane's humidity should be kept between limits so that it operates properly. This

humidity should not be too low, as a dry membrane does not work properly, but should neither be too high, as this can lead to membrane flooding. This is not a problem in the case of HT-PEMFC, as temperatures above water's boiling point turns it into vapour and membrane operation is not as restrictive as in LT-PEMFC [3, 69].

- The electrochemical reaction at cathode side is slowed down in LT-PEMFC. This may cause cathode overpotential, responsible of cell voltage losses [43].
- High concentrations of carbon monoxyde (CO, above 10 ppm) reduces performance, as it causes platinum poisoning, platinum being used as an electro-catalyst. Although platinum poisoning cannot be completely eliminated, this is substantially reduced in the case of HT-PEMFC, as higher temperatures (above 140°C) allow higher CO tolerance. This is because higher temperatures catalyse the chemical reaction between CO and water vapour to form CO_2 and hydrogen [30].
- Pure hydrogen is required for both LT-PEMFC and HT-PEMFC, but HT-PEMFC are more tolerant to impurities, which may reduce the production cost of the global system [43, 69].
- Higher temperatures cause changes in charge and transfer, as resistance is reduced. Consequently, the efficiency of the kinetic reaction increases, thus enhancing the global fuel cell efficiency [3, 43]. Additionally, higher temperatures make heat released easier to be used for practical applications.

2.2.1 Proton exchange membrane fuel cell models

In the scientific literature, several ways of modelling can be found. Each type of model is suitable to specific applications and approaches [2, 3]. Some approaches move towards concentrated parameters [9, 48] in order to simplify the formulation and make the resulting simulation of the system less demanding from a computational point of view. Another advantage of this kind of models is their clarity when it comes to analyse the results to prove their reliability. However, this simplicity can lead to errors when neglecting too many interactions and dependences between some system variables as well as their lack of resemblance to the original system's geometry.

Another way of modelling is by going to the original physical equations of fluid dynamics, diffusion and heat transfer [53, 64, 96]. These equations in their differential form include derivatives which make the system variables depend on both spatial (typically x,y,z) and temporal conditions for each part of the geometry and moment. Therefore, partial differential equations (PDE) are the ones used to determine the fuel cell system's variables evolution. Their dependence on the system's geometry up to a derivative order of two makes these models reliable in terms of precision, but too complex at the same time. This complexity needs to be simplified accordingly in order to be able to simulate them. For this reason, the number of dimensions has occasionally been reduced to two [12, 34] or one [11, 100]. Due to this fact, the complexity of the system may resemble the one of the concentrated-parameters models and that is the reason why certain authors propose three-dimensional models [9, 64]. Reducing model dimensions can reduce the reliability of the results but, in certain cases, the obtained results are reliable and easily computed. Therefore, simple models are suitable for the presented study and the simplified model can therefore be easily used for simulation and especially control design and implementation.

This thesis focuses more specifically on high-temperature proton exchange membrane fuel cells. As mentioned previously, the applications for this kind of cells have recently focused more on stationary applications. Non-stationary ones are usually the target of low-temperature fuel cells, even though some automotive applications with HT-PEMFC are being studied. Unlike LT-PEMFC, HT-PEMFC do not produce liquid water (it evaporates). For this reason, gas transport models have been considered using stationary Navier-Stokes equations [53, 64] or Darcy's law [73]. There exists a trade-off between the reliability of the model results and its usefulness when trying to implement control strategies. Another fuel cell technology operating at high temperatures is SOFC, but their really high operation temperatures (600-1000℃) make them unable to be implemented in housing facilities due to its start and stop issues, high sensibility to temperature gradients and the heat exhaustion devices needed to get rid of extra heat released by them. This makes this kind of fuel cells more adequate for industrial environments and manufacturing industry where CHP is needed for the process. Summarising, the current research in the field of PEMFC and its modelling techniques can be summarised as seen in Table 2.2.

Table 2.2: PEMFC models and characteristics

	Characteristics	Concentrated parameters models	PDE models	Experimental studies	HT models	LT models	1D models	2D and 1D +1D models	3D models
PEMFC models	[69], [90], [107], [84], [47], [3], [7], [73]	[74], [11],[48], [88], [6]	[53], [96], [99], [64], [3], [2], [12], [34], [100], [73]	[53], [99], [64], [88]	[48], [64], [88], [3], [2], [12], [34]	[53], [96], [74], [99], [11], [100], [73]	[99], [11], [48], [88], [6], [100]	[12], [34], [73]	[53], [64], [3], [2]
PEMFC annex systems models	[48], [98], [69], [90], [7]	[48], [6]		[7], [45]	[48], [98], [69], [90], [7], [45]		[48], [6]		
CHP systems	[48], [78], [40], [18], [31]	[48], [75], [18]			[48], [75], [78], [89], [40], [18]		[48], [75], [18]		

2.2.2 Proton exchange membrane fuel cell control strategies

When using HT-PEMFC, there are several variables that can be controlled. Selecting one or the other for control depends on the specific application, meaning that not all of them can be controlled at the same time. Some of these variables that can be selected as control variables are the following:

- *Operating temperature*: to prevent excess damage of the cell materials and meet the required output heat released.
- *Fuel cell stack voltage or fuel cell stack current*: to match the electrical demand

required from the fuel cell. If voltage is fixed, current is fixed consequently, as the polarisation curve establishes a direct relation between both. Similarly, if current is chosen as control variable, voltage follows its behaviour. Choosing current instead of voltage has the advantage of establishing a direct link with hydrogen flow, as current is directly related to it, while imposing voltage is done from an electrical point of view through voltage converters.

- *Input gases*: the amount of each gas injected, as well as their pressure and humidity, influence the stoichiometry and reaction's initial conditions. These flows can be controlled to match a particular reactant balance.

There exist several proposed control strategies for PEMFC, the most relevant of which are presented in Table 2.3.

Table 2.3: Control strategies for PEMFC systems

	State feedback control	**Non-linear plant control**	**Linearised plant control**	**Predictive control**	**PID controllers**	**LPV**	**Neural networks control**
PEMFC	[73]	[26], [13], [95], [71]	[10], [103], [68], [23]	[103], [65], [23], [71]	[10], [23]	[26], [13]	[1], [23]
PEMFC annex systems		[26], [13], [95]	[10], [103]	[103]	[10]	[26], [13]	
CHP systems		[95]					

When thinking about suitable control strategies for HT-PEMFC, the first step to follow is defining their control objectives. In this case, a low-level control must be applied to adjust the fuel cell's variables and a high-level supervisory control to ensure the system's efficiency and reduce fuel cell degradation. Regarding low-level control strategies, some authors propose the well-known proportional, integral and derivative (PID) controllers [10, 23] which are easier to design in linear systems but difficult to

tune in the case of nonlinear systems like fuel cells. PID controllers are better designed for linear systems around selected operating points for nonlinear ones, which implies that the system must have been linearised and some information may be lost in the process.

Another option used in certain PEMFC systems is linear parameter-varying (LPV) control [13, 26], based on considering different operation points of a nonlinear system and work with its linearised version around those points. Several operation modes may be defined so that the state-space representation is linear and time-invariant around the selected operation point. A range of operation points need to be selected based on real physical states of the PEMFC system obtained from the literature or from simulations using multiphysics' software like Comsol®. This information obtained from the literature or other simulations is the one to be used to know the range of operation of system variables. Once this range of operation is known, equilibrium points can be found solving the system of equations around this operation zone. Afterwards, this system needs to be linearised accordingly to be controlled around each of these equilibrium points. This kind of control is presented as a way of treating nonlinear systems like the ones resulting from Navier-Stokes equations or Darcy's law for gas transport in HT-PEMFC.

Finally, there exist other alternatives in HT-PEMFC control, for instance adaptive control based on neural networks [1, 23]. The aforementioned control technique is much more complex than other ones used in the literature and may be an option depending on the system requirements.

2.2.3 Proton exchange membrane fuel cell degradation

One of the main challenges nowadays in the field of PEMFC is the study of their degradation, not only their effects but also their causes and the way of acting to prevent or mitigate them. Degradation is one of the objectives tackled by control strategies as the ones presented in the previous section. The reason for doing so is that fuel cell systems are easily degraded and certain control strategies can help mitigate some of these phenomena. Degradation causes in PEMFC can be classified as follows:

- *Chemical and mechanical membrane degradation*: damages in the membrane affecting the subsequent proton exchange [28].
- *Starvation*: when the stoichiometry of the reactants (hydrogen and oxygen) is insufficient for the reaction to take place.
- *Thermal degradation*: materials degradation caused by excessive exposure to heat [43].
- *Catalyst carbon corrosion*: carbon structure of the catalyst is damaged [57].
- *Catalytic layer separation*: loss of contact between the layers impeding a proper chemical reaction [97].
- *Platinum agglomeration and dissolution*: loss of active area of platinum in the catalyst, thus reducing its effect [57].
- *Catalyst poisoning*: loss of effectiveness of the catalyst due to excessive contact with carbon monoxide (CO) [43].
- *Hydrophobic losses in the gas diffusion layer (GDL)*: transport problems of gases through the porous environment [57].

According to these criteria, the current literature on the field of PEMFC degradation has been classified, as shown in Table 2.4.

There are some differences in phenomena causing degradation in LT-PEMFC or HT-PEMFC. For instance, as it can be seen in the literature [28, 43], thermal degradation is much more important in HT-PEMFC. The majority of references on PEMFC degradation focus on stress tests and different other experiments which try to emulate real degradation under operating conditions. However, for this thesis, when trying to mitigate degradation, it is important to select ways of mitigating it from the exterior of the system. This is the reason why variables able to affect degradation must be chosen so that they are accessible externally by control systems, without interrupting internal physical phenomena introducing internal sensors and actuators that could affect operation. These variables affecting the PEMFC degradation will need to be weighted

Table 2.4: PEMFC degradation mechanisms

	Chemical and mechanical membrane degradation	Thermal degradation	Catalyst carbon corrosion	Catalytic layer separation	Platinum agglomeration and dissolution	Catalyst poisoning	Hydrophobic losses in the GDL
HT-PEMFC	[28], [43], [56], [101], [97], [102], [5]	[28], [43], [57], [101], [62], [102], [5]	[28], [43], [56], [101], [97], [102]	[28], [97]	[28], [43], [57], [97], [102]	[43], [97]	[56]
LT-PEMFC	[17], [43], [49], [51], [19], [24], [33], [46], [58], [62], [87], [94]	[17], [33], [62], [94]	[43], [49], [15], [46], [58], [72], [83], [87], [94], [106]	[19], [24], [87]	[43], [49], [51], [19], [24], [15], [46], [58], [72], [87], [94], [106]	[43], [51], [19], [94]	[49], [51], [46], [55], [58], [62], [94], [106]

according to their contribution to the cell degradation. Certain references include mathematical relationships between electrochemical active surface area (ECSA) and the fuel cell voltage [49], but these are scarce.

Among these degradation phenomena, those that are controllable need to be tackled during this thesis. A relationship between externally controllable variables such as cell voltage, electrical current, temperature or gas flow and the internal phenomena aforementioned needs to be established. An analogous degradation index has been used for battery systems [104], even though the physical phenomena involved are completely different. There exist different kinds of degradation models for battery systems, depending on the approach adopted:

- *1-D electrochemical model*: based on theoretical electrochemical equations. Degradation phenomena are modelled according to physical laws representing degrada-

tion phenomena described, so that they can be mitigated [49, 57, 58, 63].

- *Semi-empirical degradation model*: based on theoretical regression models to be fitted with parameters experimentally. Experimental data is used to find simple correlations, much direct than the ones codified by physical degradation models. These correlations can be used to directly act against degradation by modifying variables easily accessible, something not that easy to do in the case of internal variables involved in degradation mechanisms [50, 52].

- *Empirical degradation model*: based directly on experimental results to fit a certain model. These models offer direct relations between external variables able to be manipulated and degradation, but losing physical understanding of the process studied [46, 72].

These degradation models are used to establish relations between accessible and controllable variables such as fuel cell voltage, current, gas pressure or external temperature with internal variables affecting degradation. Once models able to link these two sets of variables, internal and external, are implemented, external variables to be controlled can be detected, as well as their contribution to mitigate degradation.

2.3 Micro CHP applications

HT-PEMFC-based CHP systems are among the multiple applications where fuel cells are being used nowadays [16, 30]. Fuel cells can be used for low-power and high-power applications (from hundreds of mW to MW) in terms of electrical power [30]. A global FC-based CHP system includes the following elements (Figure 2.3) [76]:

- *Fuel cell stack*: an array of fuel cells, dimensioned depending on the power required, with characteristics described above.

- *Hydrogen tank*: supplies pure hydrogen to the fuel cell. This hydrogen can come from an electrolyser, which splits water into hydrogen and oxygen [60], or from natural gas reforming, less environmentally friendly [6].

- *Heat exchanger*: HT-PEMFC's heat needs to be processed with a cooling system in many applications, but is used in the case of CHP systems. For this reason, a heat exchanger is required to convey and adapt temperature of an external fluid that acts as a medium to transfer this heat to use it for thermal demands, although some applications use equivalent systems based on air exchange [25].

- *Power conditioning system*: aims at converting DC current generated by the fuel cell stack into the adequate shape, be it DC or AC (specifying its voltage levels). Different converters need to be designed for different parts of the system.

- *Battery systems*: Used to save electrical energy for future demands in periods when demand is not that high and the fuel cell has extra energy to be stored for later. This extra energy stored mitigates problems caused by sudden demands in future periods, preventing overwork in the fuel cell that could contribute to its fast degradation.

- *Water storage tanks*: With an equivalent role to the one corresponding to battery systems, but with the goal of storing hot water to be used later for thermal demands. Due to the fact that fuel cells generate both electrical and thermal energy simultaneously, it is quite typical that high electrical demands produce extra heat that needs to be stored for later. The opposite case is also possible, when high thermal demand is needed despite low electrical demand.

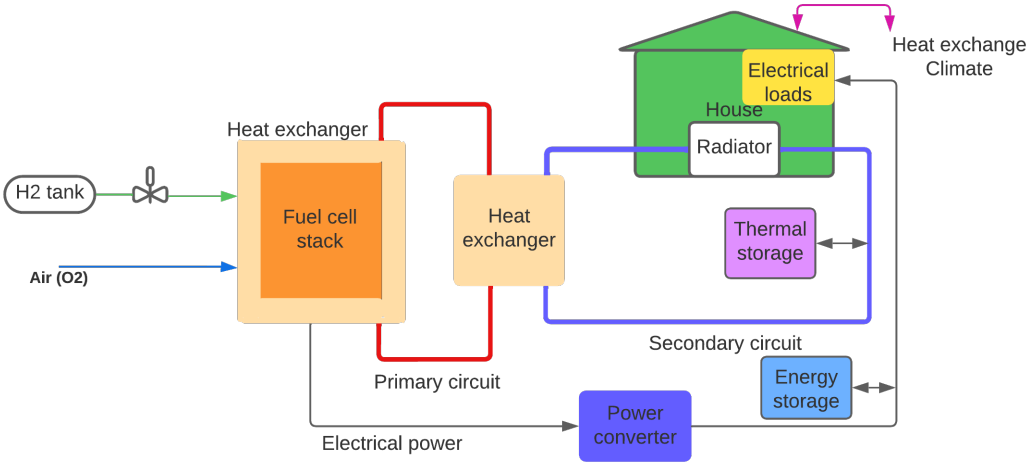

Figure 2.3: CHP system diagram

There are technologies available to integrate the fuel cell, heat recovery unit, heat exchanger, control units and its connections. A device like this has been obtained in the PACE project. Its schema and parts can be seen in Figure 2.4:

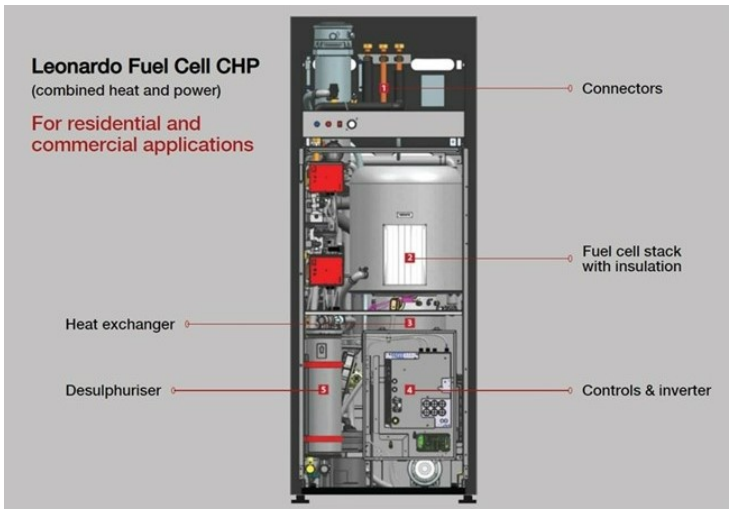

Figure 2.4: PACE project's FC-based CHP device

The main problem behind CHP systems like the one presented in Figure 2.3 is that both electrical and thermal demand need to be satisfied at all times while using thermal and electrical storage systems to mitigate sudden changes in fuel cell operation,

thus reducing fuel cell degradation and satisfying continuous operation of the global system. For this reason, different energy management strategies have been studied to deal with all these different objectives in parallel. These strategies need simple but reliable mathematical models of all elements in the CHP system [60], as detailed models based on fluid dynamics like the one in [22] are too cumbersome for control and optimisation purposes, so straightforward electrochemical equations are preferred for large scale CHP applications like the one studied.

2.4 Energy management control algorithms for housing facilities

More specifically, this thesis focuses on controlling CHP housing facilities, aiming at comfort and efficiency of the global energy consumption. The CHP system is controlled at two levels (Figure 2.5):

- *Local controllers*: aiming at controlling devices such as the fuel cell stack, thermal storage and electrical battery systems. Stability and proper operation of each device is thus ensured.
- *Supervisory control*: computing and providing system variables' values, so that electrical and thermal demand at all times are fulfilled. Among all devices involved in the CHP system, some of them need to be prioritised, depending on certain defined objectives. These can be related to efficiency, environmental reasons, mitigating degradation, among others. In Figure 2.5, systems controlled and variables provided by the supervisory control are shown: fuel cell, water storage elements and battery systems, as previously presented in Figure 2.3. Additionally, external elements such as electrical grid connections, thermal energy generated via electrical devices and thermal energy released as waste are depicted. Variable governing them are those activating them or disabling them.

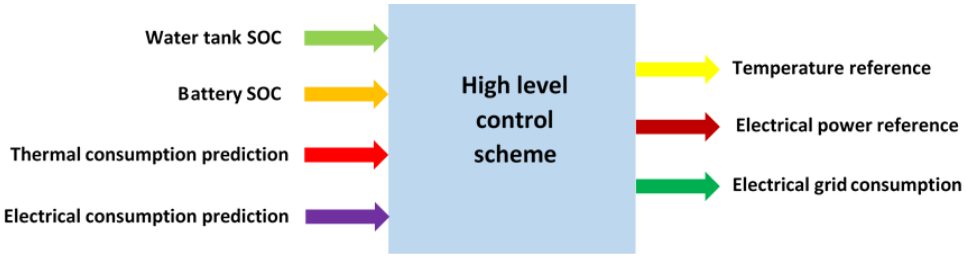

Figure 2.5: Control scheme for the CHP system

Several studies have been carried on to improve different areas of the CHP system [4]. In this line, the following research topics have been explored:

- CHP housing systems and their mathematical models.
- Algorithms for CHP energy management.

Regarding mathematical models, the field of CHP systems for housing facilities has been widely studied by many authors [37, 38, 61, 92]. As mentioned before, heat released by fuel cells needs to be used to increase the global energy efficiency of the system, thus contributing to more autonomous housing facilities. For doing so, characterisation of the parts of the system for control purposes is needed in its mathematical form. In most cases, different elements of the CHP system are designed as a result of simple energy balances, as housing applications do not require high accuracy in terms of chemical and thermal processes [20, 60]. The energy management problem consists on ensuring autonomy of the FC-based CHP system,as it is a sustainable alternative to current energy sources used nowadays, while promoting global efficiency and mitigating fuel cell degradation. The global control scheme in the CHP plant is the one seen in Figure 2.6. To implement this control problem, a multiobjective problem with the following objectives expressed as mathematical functions is defined:

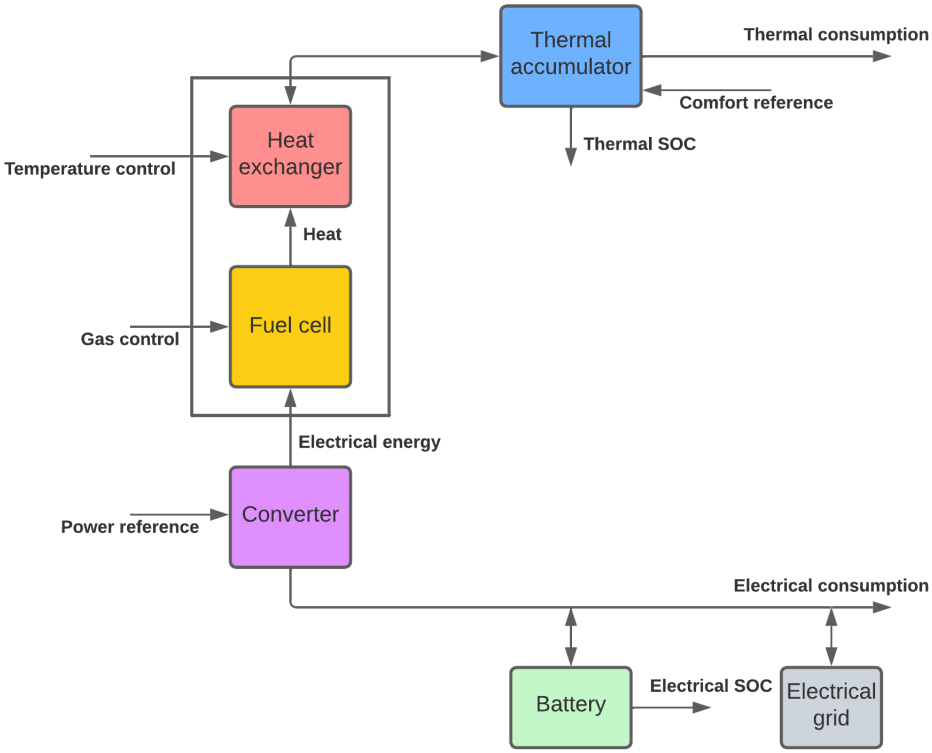

Figure 2.6: CHP plant and its controlled elements

- *Fuel cell current*: it must be the main source, instead of grid or other traditional sources, to satisfy demand. However, its variation should also be smooth to prevent degradation, as start-stop reduces fuel cell's lifetime. As a consequence, two objectives arise: one of maximising fuel cell current above other sources and another of reducing its variation along time.

- *Battery's state of charge (SOC)*: battery must be used to store electrical energy not used during periods of low demand when the fuel cell does not need to work too much. However, battery's state of charge must be kept between limits, for degradation reasons.

- *Water tank's temperature*: thermal energy must be used to heat the water tank, so that hot water can be used later to match thermal demand. This value should be below water's boiling temperature and quite stable to be ready when needed.

- *Security connections*: connection to grid must be used only when needed, avoiding fast switching between fuel cell, battery and grid. Only in extreme cases and for concrete isolated iterations should this connection be enabled. The same happens for security connections enabled such as generating thermal energy via an electric-driven space-heating device or releasing extra heat produced by the fuel cell to the environment. Both cases should be limited to exceptional occasions.

About control algorithms, several options have already been studied for CHP energy systems in the specific case of residential facilities. The main ones are the following:

- Rule-based models
- Recursive methods
- Model predictive control (MPC)

2.4.1 Rule-based models

One option studied nowadays is the use of rule-based models [92], also based on optimisation but with a different formulation, to compute CHP variables such as power generated to match both electrical and thermal demands. The method presented in [92] consists on a two-stage model aiming at following specific trajectories given while reducing computational effort, thus making it suitable for test-bench applications and embedded systems. Another method, using Markov decision methods to apply deep reinforcement learning to manage housing energy facilities, is presented on [105]. This method is reliable, as it ensures a good trajectory matching, but is highly demanding computationally. Finally, another case is the one presented in [60], which follows a logic chart to establish the different state of all CHP elements in the system. This ensures a certain tracking of variables' values and system's states.

2.4.2 Recursive methods

Other energy management methods are those ones based on recursive calculations. They are based on calculating system variables, such as fuel cell current, battery charge or thermal storage levels, assuming initial values for them, computing an algorithm's

iteration and then using this value to repeat the iteration to adjust and recalculate it. These methods have been used by some authors [20, 38]. These studies consist on updating variables along the process and going back until these are correct, i.e. they remain constant even when recalculated. In the case of [38], a forecasting unit is added to a test-bench to match energy demands in a real CHP system. This is verified in a real experimental platform and the operation of each CHP element is monitored. In the case of [20], voltage and power values of the CHP system are computed based on some initial values and, while controlled with local controllers, its values are compared to see if the final value has been reached. If that is not the case, the iteration is repeated, and this successively until the final desired value is achieved.

2.4.3 Model predictive control

Among the different techniques for controlling energy systems in general and CHP residential applications in particular, MPC has been widely used in its different versions, either linear [27, 37, 61, 70] or nonlinear MPC [14, 80]. Several studies aiming at improving performance via better prediction have been carried on by some authors [4, 108]. The ability to optimise with constraints while introducing prediction tendencies is highly valued in the case of planning demands and when trying to guarantee efficiency in advance.

MPC is a way governing CHP systems, as its algorithm is able to anticipate the system's evolution, more specifically its tendency based on prediction on the future. Electrical and thermal demands have similar behaviours from one year to the other during a specific day or season. However, some variations are always present along the day, when a minute-to-minute analysis is done. This is why the system must be resilient and adapt to variations around this predicted tendency. The MPC algorithm has an input-output structure as the one shown in Figure 2.7 and its structure, formed by its components, is the following:

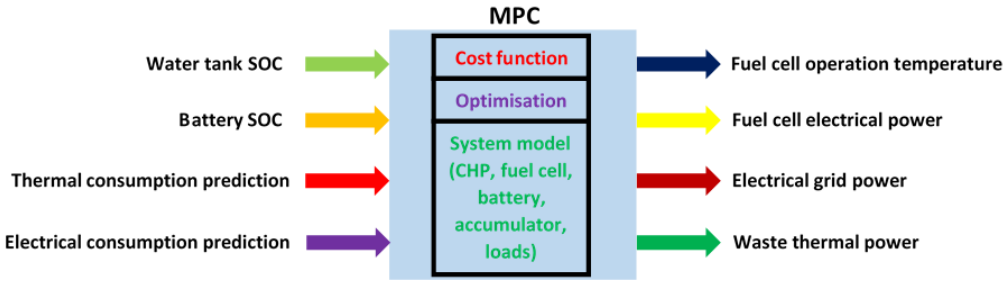

Figure 2.7: MPC scheme, with variables and mathematical components

- *An objective function*: formed by a set of subfunctions to be minimised, such as fuel cell current and its variation, battery and water tank fluctuations and energy exchanged with the grid or the environment. These subfunctions need to be multiplied by weight functions so that they can be added and form the global objective function to be minimised. These weight functions need to be selected so that some objectives are prioritised above others.

- *Variables*: system variables include fuel cell current, variables governing activation and deactivation of battery, water accumulator, grid connection and environment connection. Electrical and thermal demands are included as system disturbances. Disturbance variables have must be predicted so that the MPC can compute future scenarios, even though they cannot be predicted exactly (Figure 2.8).

- *Constraints*: these include upper and lower bounds for electrical current, battery's state of charge, water accumulator's temperature and others. Additionally, the system's equations need to be imposed as a constraint.

- *Prediction horizon*: the optimisation problem is based on the system's model and variables evaluated at the current time step iteration, but also anticipates future evolution of these variables. For this reason, a certain number of iterations in advance are predicted so that disturbances and other variables are simulated and thus prepare the system's trajectory for what is to come (Figure 2.8). Control horizon (H_u) horizon and prediction horizon (H_p) move every time the iteration k advances, predicting an extra step while computing real values for the ones already left behind. It is a way of ensuring reliability and robustness when trying to fulfill electrical and thermal demands.

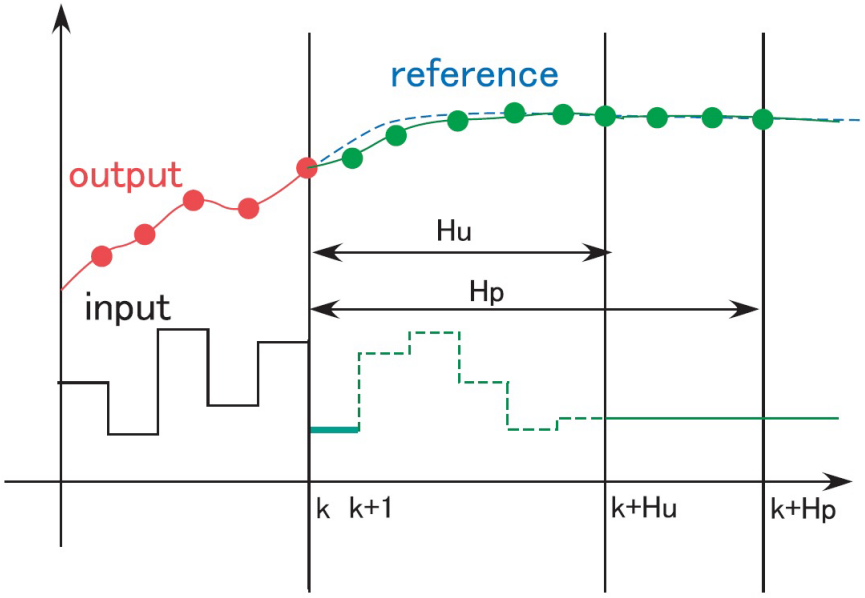

Figure 2.8: MPC variables, disturbances and prediction horizon

Regarding prediction, authors tackle its definition differently, depending on the reliability of the information they have about the system's future behaviour and its predictability in general. For example, [81] tracks prediction error in the state of charge of batteries in an energy system, so that this prediction can be improved for future scenarios.

2.4.3.1 Multiobjective problems' analysis using Pareto fronts

When dealing with multiple objectives at the same time, weighting functions need to be defined so that some objectives are prioritised above others. To guarantee the weighting functions that correspond to the optimal function, studies based on Pareto fronts have been published [29, 41, 42, 66]. In the specific of HT-PEMFC-CHP systems, several objectives to be targeted have already been presented. Among these objectives, some of them need to be prioritised, such as promoting fuel cell as the main source, mitigate its degradation via small current variation and low switching between energy sources, preventing the grid or extra thermal systems to activate every few iterations. For this reason, objectives like these are selected and a Pareto front is calculated, to find the weight functions corresponding to each objective. These objectives and weight functions

are used to build the MPC objective function [44, 82].

An energy management strategy of a CHP system, composed by different renewable systems, storage elements and heating elements, is presented in [41]. This strategy uses the concept of Pareto optimality to select efficient and less polluting operation in a multi-objective optimisation problem, connecting the CHP system to the grid when necessary. A similar approach is the one presented in [42], also prioritising efficiency and low emissions, but using an epsilon-constraint technique to solve the multi-objective problem and selecting a solution among all Pareto optimals via a fuzzy decision making.

In the case of [66], a renewable island energy system is controlled under harsh weather conditions performing a Pareto optimisation problem and a sensitivity analysis. Finally, a selection among Pareto optimal solutions in residential energy systems is used in [29], with a similar goal as the following references mentioned.

In the specific case of energy models and microgrids, approximations of these Pareto fronts to select these weighting functions have been object of study in [44, 82]. The aforementioned epsilon-constraint method is also used in the case of [82], which aims at obtaining a payoff table with points included in the Pareto front. An approximation of this Pareto front is obtained online with a filter, selecting the important points to form the structure of this trade-off surface and discarding redundant points along the process. This is done by means of a decision method based on the following steps:

1. Create a payoff table.
2. Set lower bounds for variables.
3. Calculate the range of these variables.
4. Divide this range into intervals to form the structure of the Pareto front.
5. Initialise counters.
6. Solve the problem.
7. Apply a logical loop to decide whether the point inspected belongs to the Pareto front or not.
8. Discard redundant points.

9. Add points to the Pareto front.

This algorithm is applied to a renewable-based microgrid prioritising the typical objectives of energy efficiency, environmental, security and socioeconomic issues.

A similar approach is the one presented by [44]. However, this strategy is more flexible and tackles large-scale energy applications focusing on reducing computational effort when applying the Pareto strategy in the multi-optimisation problem. This strategy is based on building a set of clusters with points obtained in the optimisation process along time. The procedure followed in the decision process is:

1. A set of clusters of points is defined successively, based on the solutions of the optimisation problem.
2. For each specific configuration, values are assigned to each cluster.
3. The average of every cluster is obtained, and a curve representative of the cluster is defined.
4. For each configuration, the centroid profile is calculated.
5. This profile's values are sorted, creating a sorted mean of it and classifying them by the order in which they appear in the original curve.
6. Values are sorted according to the order established by the cluster's representative curve.

Once this is done, Pareto fronts can be computed paying attention at low time and computing efforts. This algorithm is applied to different energy systems such as a self-sufficient building model and a prospective European network.

When implementing the multiobjective problem with the selected weight functions, all objectives are applied, but contributing to the global optimum in a way that the global set of objectives is taken into consideration. Some of these objectives are prioritised, but none of them is completely discarded. Its contribution to the global optimum is what is taken into consideration after the Pareto front has been calculated. This ensures a good fulfilment of objectives, at least to some extent not affecting others. In the case of CHP systems based of HT-PEMFC, objectives of efficiency, maximum use

of fuel cell instead of other energy alternatives, fuel cell degradation mitigation using storage systems to reduce sudden changes in fuel cell operation are among objectives to be combined, and Pareto front analysis guarantees that all of them contribute to the global problem's results [44, 82].

Chapter 3

High-temperature PEM fuel cell distributed model

Every generation laughs at the old fashions, but follows the new.

From *Walden*, by Henry David Thoreau

In this chapter, a modelling procedure of a high-temperature PEM fuel cell (HT-PEMFC) is detailed. This model is a distributed one, that is considering physical phenomena along the cell's geometry. For doing so, its characteristics presented in the previous chapter are taken into consideration, specifying the hypotheses assumed in the model described.

3.1 HT-PEMFC model equations

In order to study the fuel cell a mathematical model of all phenomena occurring in the HT-PEMFC is needed. There are several ways of modelling, depending on the approach tackled [2, 3]. Some approaches move towards concentrated parameters [9, 48] in order to simplify the formulation and make the resulting simulation of the system less demanding from a computational point of view. Another advantage of this kind of models is their clarity when it comes to analyse the results to prove their reliability. However, this simplicity can lead to errors when neglecting too many interactions and dependences between some system variables as well as their lack of resemblance to the original system's geometry.

Another way of modelling is by going to the original physical equations of fluid dynamics, diffusion and heat transfer [53, 64, 96]. These equations in their differential form include derivatives which make the system variables depend on both spatial (typically x,y,z) and time variables. Therefore, partial differential equations (PDE) are the ones used to determine the fuel cell system's variables evolution. However, these models are highly dependant on the system's geometry, with spatial derivatives up to a derivative order of two. This makes these models reliable in terms of precision, but too complex at the same time. This complexity needs to be simplified accordingly in order to be able to simulate them. For this reason, the number of dimensions has occasionally been reduced to two [12, 34] or one [11, 100]. Due to this fact, the complexity of the system may resemble the one of the concentrated models and that is the reason why certain authors propose three dimensional models [9, 64]. Reducing the model dimensions can reduce the reliability of the results but, in certain cases, the obtained results are accurate and easily computed. Therefore, simple models are suitable for the presented study and the simplified model can therefore be easily used for simulation and especially for control design and implementation.

The scope of this doctoral thesis covers high-temperature proton exchange membrane fuel cells and not their low temperature equivalents. As mentioned previously, the applications for this kind of cells have recently focused more on stationary applications. Non-stationary ones are usually the target of low temperature fuel cells, even though some automotive applications with HT-PEMFC are being studied. Unlike low temperature PEMFC, HT-PEMFC do not produce liquid water (it evaporates). For this reason, gas transport models have been considered using stationary Navier-Stokes equations [53, 64] or Darcy's law [73]. There exists a trade-off between the reliability of the model results and its usefulness when trying to implement control strategies.

The model presented is based on partial differential equations and other algebraic equations to link the different layers. The HT-PEMFC consists of:

- Anode
- Membrane
- Cathode

Both anode and cathode include the following layers and its characteristics:

- *Gas channels*: responsible of conveying the input gases (H_2 and H_2O for the anode and O_2 and H_2O for the cathode).
- *Gas diffusion layers*: transport a gas fraction to react later.
- *Catalyst layers*: place where the oxidation (anode) or reduction (cathode) reaction takes place.

The fact that temperature is above 100℃ ensures all H_2O in the system is present in its vapour form. The several existing layers have been modelled as well as their boundary conditions established. The model has the following characteristics:

- 1+1D or quasi-two dimensional representation of gas and water transport.
- Gas transport mechanisms combining diffusion.
- Variable temperature depending on the fuel cell area and time.

The relationship between fuel cell layers in the model and its disposition is depicted in figure 3.1:

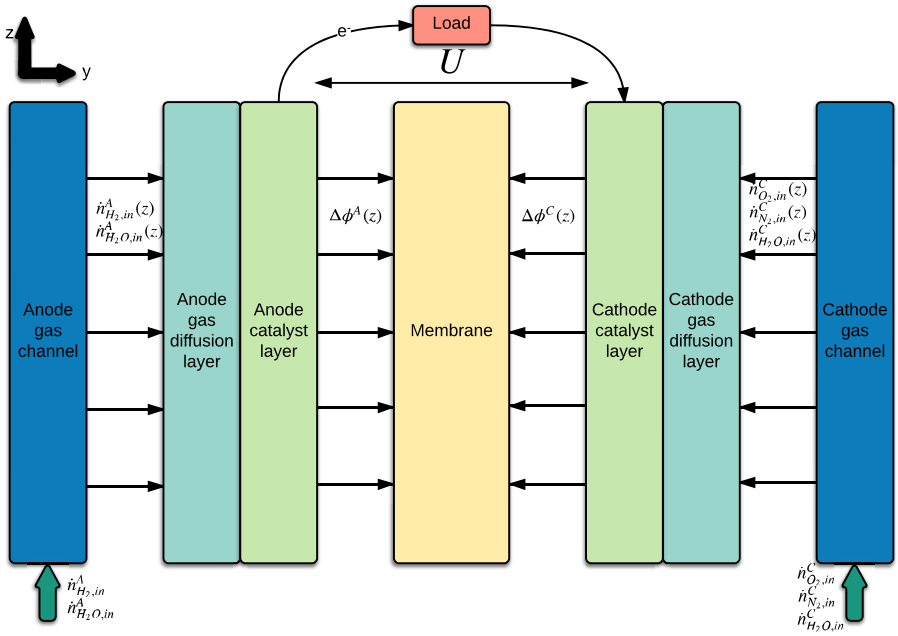

Figure 3.1: Model layers and relationship between variables

The physical and chemical mechanisms corresponding to each layer are the ones detailed henceforth:

- Convective gas transport along anode and cathode gas channels.
- Darcy's law to link pressure drop and velocity within these gas channels.
- Energy transport due to convective flow, heat conduction according to Fourier's law, heat transfer between solid fuel cell parts and gas channels and enthalpy transport caused by mass flow from gas channels to the solid.
- Caloric equations of state.
- Stefan-Maxwell diffusion for ideal gases along gas diffusion layers.
- Species balances and chemical reactions on catalyst layers using Butler-Volmer kinetic rate expressions.
- Pseudo-homogeneous energy balance for the solid parts of the fuel cell.
- Species combination on the membrane.
- Charge balances at the anode and cathode double layers.

3.2 Anode equations

3.2.1 Anode gas channels

Anode gas channels are responsible of conveying H_2 and H_2O gases. Physical mechanisms in gas channels are:

- Convective gas transport along anode and cathode gas channels.
- Darcy's law to link pressure drop and velocity within these gas channels.
- Energy transport due to convective flow, heat conduction according to Fourier's law, heat transfer between solid fuel cell parts and gas channels and enthalpy transport caused by mass flow from gas channels to the solid.
- Caloric equations of state.

Mass balances are are performed imposing convective transport along the z direction. These equations are the following:

$$\frac{\partial c^A_{H_2}}{\partial t} = -\frac{\partial v^A c^A_{H_2}}{\partial z} - \frac{\dot{n}^A_{H_2}}{\delta^A} \tag{3.1}$$

$$\frac{\partial c^A_{H_2O}}{\partial t} = -\frac{\partial v^A c^A_{H_2O}}{\partial z} - \frac{\dot{n}^A_{H_2O}}{\delta^A} \tag{3.2}$$

Their boundary conditions are:

$$v^A c^A_{H_2}\big|_{0,t} = \dot{n}^A_{H_2,in} \tag{3.3}$$

$$v^A c^A_{H_2O}\big|_{0,t} = \dot{n}^A_{H_2O,in}, \tag{3.4}$$

where

- $c^A_{H_2}$ and $c^A_{H_2O}$ are hydrogen and water vapour concentrations measured in mol/m^3.
- v^A are gas velocities measured in m/s.
- $\dot{n}^A_{H_2}$ and $\dot{n}^A_{H_2O}$ are hydrogen and water vapour molar flux densities transferred to the gas diffusion layers measured in mol/(m^2 s).
- δ^A is the height of the gas channel along direction y measured in m.
- $\dot{n}^A_{H_2,in}$ and $\dot{n}^A_{H_2O,in}$ are hydrogen and water vapour molar flux densities at the anode channel inlet measured in mol/(m^2 s).

To calculate velocities v^A a relation obtained from Darcy's law by means of pressure p^A (mesured in Pa) gradient and diffusion coefficient K^A (measured in m^2/(Pa s)) is used as shown below:

$$v^A = -K^A \frac{\partial p^A}{\partial z} \tag{3.5}$$

With boundary condition

$$p^A(L_z, t) = p^{amb}, \tag{3.6}$$

where L_z is fuel cell's channel length measured in m and p^{amb} is the ambient pressure measured in Pa. Considering ideal gases, the general ideal gases equation and Dalton's

law can be combined to relate total pressure p^A and species concentrations $c^A_{H_2}$ and $c^A_{H_2O}$ as:

$$p^A = RT^A(c^A_{H_2} + c^A_{H_2O}) \tag{3.7}$$

$R = 8.31$ J/(K mol) is the ideal gases constant and T^A is the anode temperature in K. To compute this temperature, an energy balance for the anode is needed. This must include energy transport in z-direction caused by convective flow, heat conduction according to Fourier's law, heat transfer between solid fuel cell parts at temperature T^S and gas channels and enthalpy transport caused by mass flow from channels to the solid parts [73]. The following internal energy balance as well as the caloric equation of state arise:

$$\begin{aligned}\frac{\partial(\rho u)^A}{\partial t} = &-\frac{\partial}{\partial z}\left(v^A\left(c^A_{H_2}h_{H_2}(T^A) + c^A_{H_2O}h_{H_2O}(T^A)\right)\right) + \lambda^A\frac{\partial^2 T^A}{\partial z^2} \\ &+ \frac{\alpha_1}{\delta^A}(T^S - T^A) - \frac{1}{\delta^A}\left(\dot{n}^A_{H_2}h_{H_2}(T^A) + \dot{n}^A_{H_2O}h_{H_2O}(T^A)\right) \qquad (3.8)\end{aligned}$$

$$(\rho u)^A + p^A = c^A_{H_2}h_{H_2}(T^A) + c^A_{H_2O}h_{H_2O}(T^A), \tag{3.9}$$

providing that

- $(\rho u)^A$ is the internal energy of the anode channels measured in J/m^3.
- $h_{H_2}(T^A)$ and $h_{H_2O}(T^A)$ are molar enthalpies of hydrogen and water vapour at temperature T^A measured in J/mol.
- λ^A is heat conductivity on the anode measured in W/(m K).
- α_1 is the heat transfer coefficient measured in W/(m^2 K).
- δ^A is the anode channels width measured in m.
- T^S is the solid parts temperature measured in K.

Their boundary conditions are the following:

$$\dot{n}^A_{H_2,in} h_{H_2}(T^A_{in}) + \dot{n}^A_{H_2O,in} h_{H_2O}(T^A_{in}) = v^A \Big(c^A_{H_2} h_{H_2}(T^A)\big|_{0,t} + c^A_{H_2O} h_{H_2O}(T^A)\big|_{0,t} \Big) - \lambda^A \frac{\partial T^A}{\partial z}\bigg|_{0,t} \tag{3.10}$$

$$\lambda^A \frac{\partial T^A}{\partial z}\bigg|_{L_z,t} = 0, \tag{3.11}$$

where $h_{H_2}(T^A_{in})$ and $h_{H_2O}(T^A_{in})$ are hydrogen's and water vapour's molar enthalpy at anode's inlet temperature in J/mol. Enthalpies $h_{H_2}(T^A)$ and $h_{H_2O}(T^A)$ are calculated referred to temperature using the specific heat ($c_p^{H_2}$ for hydrogen and $c_p^{H_2O}$ for water vapour) approximation for computational reasons as:

$$h_{H_2}(T^A) = c_p^{H_2} T^A \tag{3.12}$$

$$h_{H_2O}(T^A) = c_p^{H_2O} T^A \tag{3.13}$$

These equations calculate $c^A_{H_2}$, $c^A_{H_2O}$, p^A using variables $\dot{n}^A_{H_2}$ and $\dot{n}^A_{H_2O}$ coming from the anode gas diffusion layer.

3.2.2 Anode gas diffusion layer

Gas diffusion layers are introduced to limit the mass transport between gas channels and catalyst layers. Stefan-Maxwell diffusion for ideal gases is the one assumed for the transport along direction y using Euler approximation for molar fraction values instead of mean values like the one in [73]:

$$-\nabla \chi^A_{H_2} = \frac{\chi^A_{H_2O} \dot{n}^A_{H_2} - \chi^A_{H_2} \dot{n}^A_{H_2O}}{\bar{c}^A D^{eff}_{H_2,H_2O}} \tag{3.14}$$

$$\nabla \chi^A_{H_2} = \frac{\chi^{CA}_{H_2} - \chi^A_{H_2}}{\delta^{GA}} \tag{3.15}$$

$$\bar{c}^A = \frac{p^A}{RT^S} \tag{3.16}$$

$D^{eff}_{H_2,H_2O}$ $[m^2 s]$ is the effective diffusion coefficient of one gas through the other, $\nabla \chi^A_{H_2}$ is the gradient of molar fraction, $\chi^{CA}_{H_2}$ and $\chi^{CA}_{H_2O}$ are molar fractions in the anode catalyst layers and $\chi^A_{H_2}$ and $\chi^A_{H_2O}$ are molar fractions in the anode.

These equations calculate $\chi^{CA}_{H_2}$ using variables $\dot{n}^A_{H_2}$ coming from the catalyst layer. Once $\chi^{CA}_{H_2}$ is known, variable $\chi^{CA}_{H_2O}$=1-$\chi^{CA}_{H_2}$ can be calculated. If other diffusion coefficients are defined as the previous one ($D^{eff}_{H_2,H_2}$, $D^{eff}_{H_2O,H_2}$ and $D^{eff}_{H_2O,H_2O}$) The proof is the following one:

$$\chi^{CA}_{H_2} + \chi^{CA}_{H_2O} = \chi^{A}_{H_2} + \chi^{A}_{H_2O} - \frac{\delta^{GA}}{\bar{c}^A} \sum_k \Big[\frac{1}{D^{eff}_{H_2,k}} (\chi^A_k \dot{n}^A_{H_2} - \chi^A_{H_2} \dot{n}^A_k) + \tag{3.17}$$

$$+ \frac{1}{D^{eff}_{H_2O,k}} (\chi^A_k \dot{n}^A_{H_2O} - \chi^A_{H_2O} \dot{n}^A_k) \Big] = \tag{3.18}$$

$$= 1 - \frac{\delta^{GA}}{\bar{c}^A} \Big[\frac{1}{D^{eff}_{H_2,H_2}} (\chi^A_{H_2} \dot{n}^A_{H_2} - \chi^A_{H_2} \dot{n}^A_{H_2}) +$$

$$+ \frac{1}{D^{eff}_{H_2,H_2O}} (\chi^A_{H_2} \dot{n}^A_{H_2O} - \chi^A_{H_2O} \dot{n}^A_{H_2}) +$$

$$+ \frac{1}{D^{eff}_{H_2O,H_2}} (\chi^A_{H_2} \dot{n}^A_{H_2O} - \chi^A_{H_2O} \dot{n}^A_{H_2}) +$$

$$+ \frac{1}{D^{eff}_{H_2O,H_2O}} (\chi^A_{H_2O} \dot{n}^A_{H_2O} - \chi^A_{H_2O} \dot{n}^A_{H_2O}) \Big] =$$

$$= 1 \tag{3.19}$$

If all equations are arranged in only one the following expression for $\chi^{CA}_{H_2}$ is obtained:

$$-\frac{\chi^{CA}_{H_2} - \chi^A_{H_2}}{\delta^{GA}} = \frac{\chi^A_{H_2O} \dot{n}^A_{H_2} - \chi^A_{H_2} \dot{n}^A_{H_2O}}{\bar{c}^A D^{eff}_{H_2,H_2O}} \tag{3.20}$$

$$-\chi^{CA}_{H_2} \frac{\bar{c}^A D^{eff}_{H_2,H_2O}}{\delta^{GA}} + \chi^A_{H_2} \frac{\bar{c}^A D^{eff}_{H_2,H_2O}}{\delta^{GA}} = (1 - \chi^A_{H_2}) \dot{n}^A_{H_2} - \chi^A_{H_2} \dot{n}^A_{H_2O} \tag{3.21}$$

$$-\frac{\bar{c}^A D^{eff}_{H_2,H_2O}}{\delta^{GA}} \chi^{CA}_{H_2} = \dot{n}^A_{H_2} + \Big[-\frac{\bar{c}^A D^{eff}_{H_2,H_2O}}{\delta^{GA}} - \dot{n}^A_{H_2} - \dot{n}^A_{H_2O} \Big] \chi^A_{H_2} \tag{3.22}$$

$$\chi^{CA}_{H_2} = \frac{\Big[\dot{n}^A_{H_2} + \dot{n}^A_{H_2O} + \frac{2\bar{c}^A D^{eff}_{H_2,H_2O}}{\delta^{GA}} \Big] \chi^A_{H_2} - \dot{n}^A_{H_2}}{\frac{\bar{c}^A D^{eff}_{H_2,H_2O}}{\delta^{GA}}} \tag{3.23}$$

$\chi^A_{H_2O}$ is obtained as $\chi^A_{H_2O} = 1 - \chi^{CA}_{H_2}$.

3.2.3 Anode catalyst layer

Anode catalyst layers are those connecting anode and membrane and they are responsible of ensuring the reaction of the species, i.e hydrogen. It includes platinum on a carbon base to help the reaction occur. In the case of the anode, the oxidation chemical reaction takes place and its chemical equation is the following one:

$$\mathrm{H_2} \longrightarrow 2\mathrm{H^+} + 2\mathrm{e^-}$$

Based on this chemical reaction and its limiting reactant characteristics the following statements can be imposed:

$$\dot{n}^A_{H_2} = r^A \tag{3.24}$$

$$\dot{n}^A_{H_2O} = 0 \tag{3.25}$$

Using chemical kinetics as in [35, 77] and membrane characteristics [77] Butler-Volmer equation can be derived and used to compute hydrogen's molar flux density going through the cell $\dot{n}^A_{H_2}$, using reactive term r^A as follows:

$$r^A = f^V \frac{i_{A0}}{2F}\left[\exp\left(\frac{2F}{RT^S}\left(\Delta\Phi^A - \Delta\Phi^A_{ref}\right)\right)\frac{\chi^{CA}_{H_2} p^A}{p_{H_2,ref}} - 1\right], \tag{3.26}$$

where

- r^A is the molar rate reacting in the anode measured in mol/(m^2 s).
- f^v is the catalyst's platinum content coefficient.
- i_{A0} is the open-circuit anode current measured in A.
- $p_{H_2,ref}$ is hydrogen's reference pressure measured in Pa.
- $\Delta\Phi^A$ is the protonic potential difference in the anode measured in V.
- $\Delta\Phi^A_{ref}$ is the protonic potential difference's reference value in the anode measured in V.

Butler-Volmer equation needs to be replaced on the anode gas diffusion layer equations to obtain the value for $\chi^{CA}_{H_2}$ and $\chi^{CA}_{H_2O} = 1 - \chi^{CA}_{H_2}$.

3.3 Cathode equations

An analogous procedure is applied for the cathode equations. The gases considered are the reacting ones, that is, nitrogen is not considered.

3.3.1 Cathode gas channels

Anode gas channels are responsible of conveying O_2, N_2 and H_2O gases. The mass balances are are performed imposing convective transport along the z direction. These equations are the following:

$$\frac{\partial c^C_{O_2}}{\partial t} = -\frac{\partial v^C c^C_{O_2}}{\partial z} - \frac{\dot{n}^C_{O_2}}{\delta^C} \tag{3.27}$$

$$\frac{\partial c^C_{N_2}}{\partial t} = -\frac{\partial v^C c^C_{N_2}}{\partial z} - \frac{\dot{n}^C_{N_2}}{\delta^C} \tag{3.28}$$

$$\frac{\partial c^C_{H_2O}}{\partial t} = -\frac{\partial v^C c^C_{H_2O}}{\partial z} - \frac{\dot{n}^C_{H_2O}}{\delta^C} \tag{3.29}$$

Their boundary conditions are:

$$v^C c^C_{O_2}\big|_{0,t} = \dot{n}^C_{O_2,in} \tag{3.30}$$

$$v^C c^C_{N_2}\big|_{0,t} = \dot{n}^C_{N_2,in} \tag{3.31}$$

$$v^C c^C_{H_2O}\big|_{0,t} = \dot{n}^C_{H_2O,in}, \tag{3.32}$$

where

- O_2, N_2 and H_2O are oxygen, nitrogen and water vapour concentrations measured in mol/m^3.
- v^C are gas velocities measured in m/s.
- $\dot{n}^C_{O_2}$, $\dot{n}^C_{N_2}$ and $\dot{n}^C_{H_2O}$ are oxygen, nitrogen and water vapour molar flux densities transferred to the gas diffusion layers measured in mol/(m^2 s).
- δ^C is the height of the gas channel along direction y measured in m.
- $\dot{n}^A_{O_2,in}$, $\dot{n}^A_{N_2,in}$ and $\dot{n}^A_{H_2O,in}$ are oxygen, nitrogen and water vapour molar flux densities at the cathode channel inlet measured in mol/(m^2 s).

An analogous procedure as in the anode is used to calculate velocities v^C:

$$v^C = -K^C \frac{\partial p^C}{\partial z} \tag{3.33}$$

Pressure is bounded as:

$$p^C(L_z, t) = p^{amb} \tag{3.34}$$

Pressures are calculated similarly using ideal gases equation and Dalton's law:

$$p^C = RT^C(c^C_{O_2} + c^C_{N_2} + c^C_{H_2O}) \tag{3.35}$$

Finally, the internal energy balance and the caloric equation of state are performed consequently:

$$\begin{aligned}\frac{\partial (\rho u)^C}{\partial t} = &-\frac{\partial}{\partial z}\left(v^C\left(c^C_{O_2}h_{O_2}(T^C) + c^C_{N_2}h_{N_2}(T^C) + c^C_{H_2O}h_{H_2O}(T^C)\right)\right) \\ &+ \lambda^C \frac{\partial^2 T^C}{\partial z^2} + \frac{\alpha_1}{\delta^C}\left(T^S - T^C\right) \\ &- \frac{1}{\delta^C}\left(\dot{n}^C_{O_2}h_{O_2}(T^C) + \dot{n}^C_{N_2}h_{N_2}(T^C) + \dot{n}^C_{H_2O}h_{H_2O}(T^C)\right) \end{aligned} \tag{3.36}$$

$$(\rho u)^C + p^C = c^C_{O_2}h_{O_2}(T^C) + c^C_{N_2}h_{N_2}(T^C) + c^C_{H_2O}h_{H_2O}(T^C), \tag{3.37}$$

providing that

- $(\rho u)^C$ is the internal energy of the cathode channels measured in J/m^3.
- $h_{O_2}(T^C)$, $h_{N_2}(T^C)$ and $h_{H_2O}(T^C)$ are molar enthalpies of hydrogen, nitrogen and water vapour at temperature T^C measured in J/mol.
- λ^C is heat conductivity on the cathode measured in W/(m K).
- α_1 is the heat transfer coefficient measured in W/(m^2 K).
- δ^C is the cathode channels width measured in m.
- T^S is the solid parts temperature measured in K.

Their boundary conditions are the following:

- $\dot{n}^C_{O_2,in} h_{O_2}(T^C_{in}) + \dot{n}^C_{N_2,in} h_{N_2}(T^C_{in}) + \dot{n}^C_{H_2O,in} h_{H_2O}(T^C_{in}) = v^C \Big(c^C_{O_2} h_{O_2}(T^C)\big|_{0,t} +$

$$+ c^C_{N_2} h_{N_2}(T^C)\big|_{0,t} + c^C_{H_2O} h_{H_2O}(T^C)\big|_{0,t} \Big) - \lambda^C \frac{\partial T^C}{\partial z}\bigg|_{0,t}$$

- $\lambda^C \frac{\partial T^C}{\partial z}\Big|_{L_z,t} = 0,$

where $h_{O_2}(T^C_{in})$, $h_{N_2}(T^C_{in})$ and $h_{H_2O}(T^C_{in})$ are oxygen's, nitrogen's and water vapour's molar enthalpy at anode's inlet temperature in J/mol. These equations calculate $c^C_{O_2}$, $c^C_{N_2}$, $c^C_{H_2O}$, p^C using variables $\dot{n}^C_{O_2}$, $\dot{n}^C_{N_2}$ and $\dot{n}^C_{H_2O}$ coming from the anode gas diffusion layer.

Enthalpies $h_{O_2}(T^C)$, $h_{N_2}(T^C)$ and $h_{H_2O}(T^C)$ are calculated referred to temperature using the specific heat ($c_p^{O_2}$, $c_p^{N_2}$ and $c_p^{H_2O}$) approximation as before for computational reasons as:

$$h_{O_2}(T^C) = c_p^{O_2} T^C \tag{3.38}$$

$$h_{N_2}(T^C) = c_p^{N_2} T^C \tag{3.39}$$

$$h_{H_2O}(T^C) = c_p^{H_2O} T^C \tag{3.40}$$

3.3.2 Cathode gas diffusion layer

Following the same procedure carried on for the anode case, Stefan-Maxwell diffusion is considered and its equations considering oxygen, nitrogen and water vapour are the following ones:

$$-\nabla \chi^C_{O_2} = \frac{\chi^C_{H_2O} \dot{n}^C_{O_2} - \chi^C_{O_2} \dot{n}^C_{H_2O}}{\bar{c}^C D^{eff}_{O_2,H_2O}} + \frac{\chi^C_{N_2} \dot{n}^C_{O_2} - \chi^C_{O_2} \dot{n}^C_{N_2}}{\bar{c}^C D^{eff}_{O_2,N_2}} \tag{3.41}$$

$$\nabla \chi^C_{O_2} = \frac{\chi^{CC}_{O_2} - \chi^C_{O_2}}{\delta^{GC}} \tag{3.42}$$

$$-\nabla \chi^C_{N_2} = \frac{\chi^C_{H_2O} \dot{n}^C_{N_2} - \chi^C_{N_2} \dot{n}^C_{H_2O}}{\bar{c}^C D^{eff}_{N_2,H_2O}} + \frac{\chi^C_{O_2O} \dot{n}^C_{N_2} - \chi^C_{N_2} \dot{n}^C_{O_2}}{\bar{c}^C D^{eff}_{N_2,O_2}} \tag{3.43}$$

$$\nabla \chi^C_{N_2} = \frac{\chi^{CC}_{N_2} - \chi^C_{N_2}}{\delta^{GC}} \tag{3.44}$$

$$\bar{c}^C = \frac{p^C}{RT^S} \tag{3.45}$$

These equations calculate oxygen's and nitrogen's molar fraction for the cathode catalyst layer $\chi^{CC}_{O_2}$, $\chi^{CC}_{N_2}$ using variables $\dot{n}^{C}_{O_2}$, $\dot{n}^{C}_{N_2}$ and $\dot{n}^{C}_{H_2O}$ coming from the catalyst layer. $D^{eff}_{O_2,H_2O}$, $D^{eff}_{N_2,H_2O}$, $D^{eff}_{O_2,N_2}$, $D^{eff}_{O_2,H_2O}$ are the effective diffusion coefficients of all gases through the others. Once $\chi^{CC}_{O_2}$ and $\chi^{CC}_{N_2}$ are known, variable $\chi^{CC}_{H_2O} = 1-\chi^{CC}_{O_2}-\chi^{CC}_{N_2}$ can be calculated. The proof is analogous to the one for the anode.

3.3.3 Cathode catalyst layer

In the cathode catalyst layer a reduction reaction of oxygen is produced and its associated system chemical equation is the following one:

$$\tfrac{1}{2}\mathrm{O}_2 + 2\mathrm{e}^- + 2\mathrm{H}^+ \longrightarrow \mathrm{H}_2\mathrm{O}$$

Based on this chemical reaction the following relations can be defined:

$$\dot{n}^{C}_{O_2} = \frac{1}{2} r^C \tag{3.46}$$

$$\dot{n}^{C}_{N_2} = 0 \tag{3.47}$$

$$\dot{n}^{C}_{H_2O} = r^C \tag{3.48}$$

$\dot{n}^{C}_{H_2O}$ and $\dot{n}^{C}_{O_2}$ are obtained from the these equations and the reactive term r^C can be obtained using the Butler-Volmer [73] equation as follows:

$$r^C = f^V \frac{i_{C0}}{2F} \exp\Big(\frac{\Delta G_0}{R}\big(\frac{1}{T^S} - \frac{1}{T^{ref}}\big)\Big) \frac{\chi^{CC}_{O_2} p^C}{p_{O_2,ref}} \exp\Big(-\frac{\alpha 2F}{RT^S}\big(\Delta\Phi^C - \Delta\Phi^C_{ref}\big)\Big), \tag{3.49}$$

where

- r^C is the molar rate reacting in the cathode measured in mol/(m^2 s).
- ΔG_0: Gibbs free energy of the open-circuit reaction J/mol.
- T^{ref} is the reference temperature measured in K.
- i_{C0} is the open-circuit cathode current measured in A.
- $p_{O_2,ref}$ is oxygen's reference pressure measured in Pa.
- α is the stoichiometric adjusting coefficient.

- $\Delta\Phi^C$ is the protonic potential difference in the cathode measured in V.
- $\Delta\Phi^C_{ref}$ is the protonic potential difference's reference value in the cathode measured in V.

Butler-Volmer equation needs to be replaced on the anode gas diffusion layer equations to obtain the value for $\chi^{CC}_{O_2}$ and $\chi^{CC}_{H_2O} = 1 - \chi^{CC}_{O_2} - \chi^{CC}_{N_2}$.

3.4 Equations combining anode and cathode

3.4.1 Membrane

The membrane is responsible of carrying protons from anode to cathode to ensure they can be combined to form water. However, membrane is not able to carry gases, majoritary when having high temperatures as it is the case. This generates an electrical current of electrons through a load connected in parallel with the fuel cell. Therefore, membrane equations combine both anode and cathode variables and provide molar flows to the outer layers and i_M electrical current to calculate $\Delta\Phi_A$ and $\Delta\Phi_C$ [77]. The flows to be transmitted to outer layers can be defined as:

$$\dot{n}_{H+} = -\frac{k}{F^2}\nabla\mu_{H+} \tag{3.50}$$

$$\nabla\mu_{H+} = F\nabla\Phi \tag{3.51}$$

$$\nabla\Phi = \frac{\Phi^{CM} - \Phi^{AM}}{\delta^M} = -\frac{\Delta\Phi^M}{\delta^M} \tag{3.52}$$

Variables appearing on these equations have the following meaning:

- k is electrical conductivity measured in C
- $F = 96485$ C/mol is the electrical load of a mole of a given substance (known as Faraday's constant).
- $\nabla\mu_{H+}$ is the gradient of proton electrical potential measured in J/mol.
- $\Delta\Phi^M$ is the membrane potential difference measured in V.
- δ^M is the membrane width measured in m.

Finally, the electrical current i_M can be directly linked to the proton flow using Faraday's constant F as:

$$i^M = F\dot{n}_{H+} \tag{3.53}$$

3.4.2 Solid part energy balance

Solid parts of the fuel cells, formed by gas diffusion layers, catalyst layers and membrane, have a certain temperature T^S. This is spatially distributed and can be calculated using

the following energy balance [73]:

$$\begin{aligned}\delta^S \frac{\partial(\rho e)^S}{\partial t} &= \dot{n}^A_{H_2} h_{H_2}(T^A) + \dot{n}^A_{H_2O} h_{H_2O}(T^A) + \dot{n}^C_{O_2} h_{O_2}(T^C) + \dot{n}^C_{N_2} h_{N_2}(T^C) + \\ &+ \dot{n}^C_{H_2O} h_{H_2O}(T^C) + \alpha_1\big((T^A - T^S) + (T^C - T^S)\big) + \alpha_2(T_{cool} - T^S) + \\ &+ \lambda^S \delta^S \frac{\partial^2 T^S}{\partial z^2} - (\Phi^C - \Phi^A) i^M \end{aligned} \tag{3.54}$$

$$\begin{aligned}\delta^S (\rho e)^S &= \delta^S (\rho u)^S + C^A \delta^{AC} \frac{\Delta\Phi^{A2}}{2} + C^C \delta^{CC} \frac{\Delta\Phi^{C2}}{2} \\ &= (\delta^S - \delta^M)(\rho h)^S(T^S) + \delta^M (\rho h)^M(T^S) + \delta^M \rho^M_{H_2O} h_{H_2O}(T^S) + \\ &+ C^A \delta^{AC} \frac{\Delta\Phi^{A2}}{2} + C^C \delta^{CC} \frac{\Delta\Phi^{C2}}{2}, \end{aligned} \tag{3.55}$$

where

- $(\rho e)^S$ is the total energy measured in J/m^3.
- δ^S is the solid part width measured in m.
- α_2 is a heat transfer coefficient measured in W/(m^2 K).
- λ^S is the solid part heat conduction coefficient measured in W/(m K).
- i^M is the membrane electrical current density measured in A/m^2.
- C^A and C^C are anode and cathode capacities measured in F/m^3.
- δ^{AC} and δ^{CC} are anode and cathode catalyst layers' width measured in m.
- $\Delta\Phi^A$ and $\Delta\Phi^C$ are anode and cathode proton potential difference measured in V.
- T_{cool} is the coolant's temperature measured in K.
- $(\rho u)^S$ is the solid parts' internal energy measured in J/m^3.
- $(\rho h)^S(T^S)$ is the solid parts' enthalpy measured in J/m^3.
- $(\rho h)^S(T^S)$ is the total enthalpy in the membrane measured in J/m^3.
- $\rho^M_{H_2O} h_{H_2O}(T^S)$ is water vapour's enthalpy in the membrane mesured in J/m^3.

The boundary conditions for T^S are:

$$\left.\frac{\partial T^S}{\partial z}\right|_{0,t} = \left.\frac{\partial T^S}{\partial z}\right|_{L_z,t} = 0 \tag{3.56}$$

3.4.3 Charge balances

Finally, the proton potential differences $\Delta\Phi_A$ and $\Delta\Phi_C$ needed by outer layers' equations are calculated using i^M:

$$C^A \delta^{AC} \frac{\partial \Delta\Phi_A}{\partial t} = i^M - 2Fr^A \tag{3.57}$$

$$C^C \delta^{CC} \frac{\partial \Delta\Phi_C}{\partial t} = i^M + 2Fr^C \tag{3.58}$$

3.4.3.1 Voltage as an input

$\Delta\Phi^M$ can be calculated fixing voltage U and applying the following:

$$\Delta\Phi^M(z,t) = \Delta\Phi^C(z,t) - \Delta\Phi^A(z,t) - U(t) \tag{3.59}$$

The total electrical current I and power produced P can be calculated as:

$$I = L_x \int_0^{L_z} i^M dz \tag{3.60}$$

$$P = UI, \tag{3.61}$$

where L_x is fuel cell's length along x direction measured in m.

3.4.3.2 Current as an input

Alternatively, current I can be fixed and causality of the equations accordingly. If nodes $j = 1, \ldots, N$ are considered the following rearrangement of equation (3.59) resulting in equation (3.62) for node 1:

$$U(t) = \Delta\Phi^C(1,t) - \Delta\Phi^A(1,t) - \Delta\Phi^M(1,t) \tag{3.62}$$

To analyse the causality of the problem a set of diagrams called bond graphs defined as shown in [36, 54, 79]. Essentially, a bond graph shows the relationship between variables of a problem to be solved setting 0-junctions where currents are added and 1-junctions where voltages are added. Arrows with transversal lines show causality order, i.e. which variables are used to calculate other ones. When there arrows don't have transversal lines there are no causality relationships and it is called acausal bond graph, which can be used to deduce the causality in further bond graphs. In the case we had

one node bond graphs of figures 3.2, 3.3 and 3.6 are depicted to relate all variables intervening in the problem.

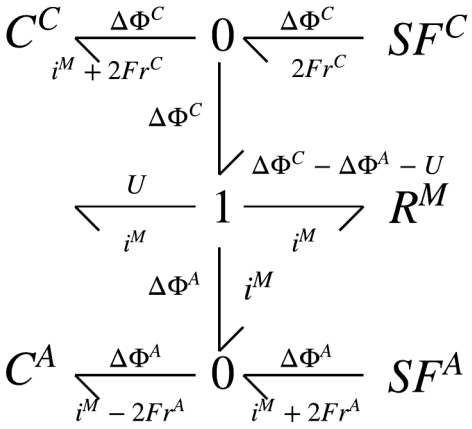

Figure 3.2: Acausal bond graph

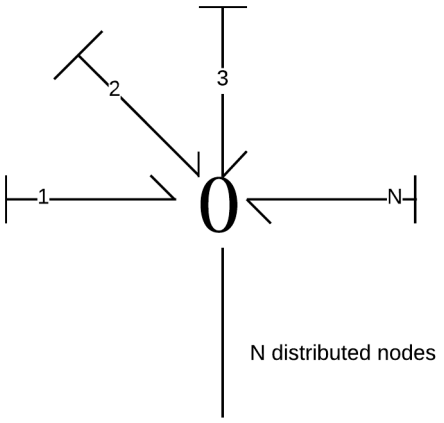

Figure 3.3: Distributed system

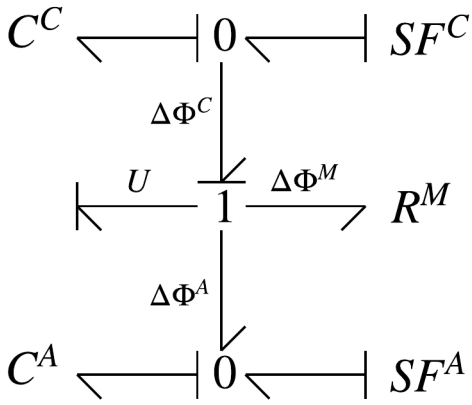

Figure 3.4: Imposing current on one node

Causality of the current problem is the one defined in figures 3.6 and 3.7 where the bond graphs to show the causality are shown:

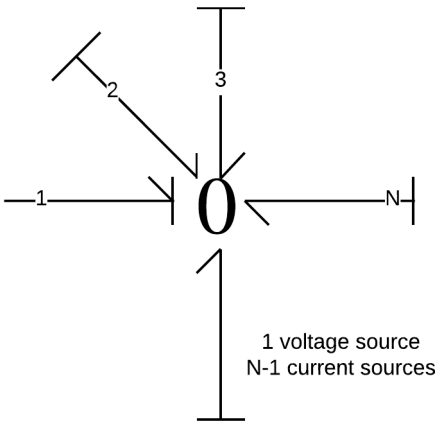

Figure 3.5: N-1 acting as current sources and one of them acting as a voltage source (current imposed externally)

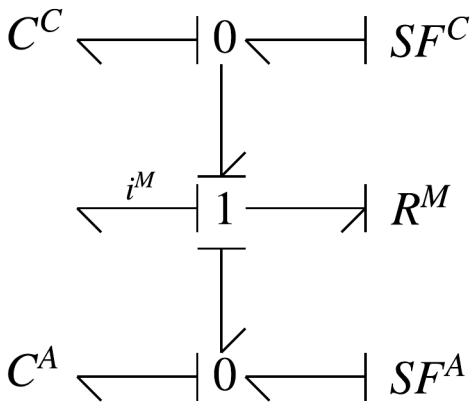

Figure 3.6: Imposing voltage on one node

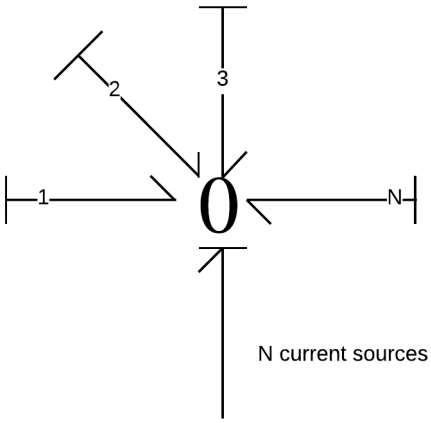

Figure 3.7: N nodes acting as current sources (voltage imposed externally)

In equation (3.62) $U(t) = U(z,t)$ is considered constant for all nodes because it represents the voltage difference between one side and the other of the cell. Similarly, equations (3.50) to (3.52) can be combined to express $\Delta\Phi^M(1,t)$ from node 1 as a function of current density across node 1 $i^M(1,t)$:

$$\Delta\Phi^M(1,t) = \frac{\delta^M}{k} i^M(1,t) \tag{3.63}$$

Considering the fixed current I and other nodes current densities $i^M(i)$ for other nodes $j = 2,\ldots,N$, node 1 is defined as a voltage source with the following current

$i^M(1)$:

$$i^M(1) = \frac{I}{L_x L_z} - i^M(2) - \ldots - i^M(N) \tag{3.64}$$

This expression of $i^M(1)$ can be plugged in equations (3.57) and (3.58) when applying them to node 1. Equations for the following nodes $j = 2, \ldots, N$ are defined imposing currents $i^M(j)$ rearranging equations (3.62) to (3.63) as:

$$\Delta\Phi^M(j,t) = \Delta\Phi^C(j,t) - \Delta\Phi^A(j,t) - U(t) \tag{3.65}$$

$$i^M(j) = \frac{k}{\delta^M}\Delta\Phi^M(j,t) \tag{3.66}$$

Combining both equations (3.65) and (3.66) the following expression for $i^M(j)$ can be obtained:

$$i^M(j) = \frac{k}{\delta^M}(\Delta\Phi^C(j,t) - \Delta\Phi^A(j,t) - U(t)) \tag{3.67}$$

Current $i^M(j)$ is finally plugged in equations (3.57) and (3.58) to compute $\Delta\Phi^A(j,t)$ and $\Delta\Phi^C(j,t)$ for nodes $j = 2, \ldots, N$ different from 1.

3.5 HT-PEMFC model equations discretisation

First of all, the fluid dynamics equations have been defined and are simplified taking into consideration certain constraints. All these equations are then discretised (only spatial coordinates z). Temporal derivatives have not been discretised. Discretisation is defined for a generic function $f(z)$, assuming Δz as a small magnitude, and performed differently depending on the node position:

- **Forward difference**:

$$\begin{aligned} \frac{\partial f(z)}{\partial z} &\approx \frac{f(z+\Delta z) - f(z)}{\Delta z} \\ \frac{\partial^2 f(z)}{\partial z^2} &\approx \frac{f(z+2\Delta z) - 2f(z+\Delta z) + f(z)}{(\Delta z)^2} \end{aligned} \tag{3.68}$$

- **Backward difference**:

$$\begin{aligned} \frac{\partial f(z)}{\partial z} &\approx \frac{f(z) - f(z-\Delta z)}{\Delta z} \\ \frac{\partial^2 f(z)}{\partial z^2} &\approx \frac{f(z) - 2f(z+\Delta z) + f(z-2\Delta z)}{(\Delta z)^2} \end{aligned} \tag{3.69}$$

- **Central difference**:

$$\begin{aligned}\frac{\partial f(z)}{\partial z} &\approx \frac{f(z+\Delta z)-f(z-\Delta z)}{2\Delta z}\\ \frac{\partial^2 f(z)}{\partial z^2} &\approx \frac{f(z+\Delta z)-2f(z)+f(z-\Delta z)}{(\Delta z)^2}\end{aligned} \tag{3.70}$$

For instance, for nodes located around the rim of the geometry equations (3.68) or (3.69) are required and for inner nodes, equation (3.70). To illustrate, the central difference in equation (3.70) approach for inner nodes is the one used henceforth. Equations to be discretised are the ones of the anode and cathode channels and the solid part energy balance.

3.5.1 Anode channels equations discretisation

The system equations to be codified can be divided in algebraic and differential equations (with time derivatives). The algebraic ones to define gas velocities $v^A(i)$, gas pressure $p^A(i)$ and internal energy $(\rho u)^A$ are:

$$v^A(i) = -K^A \frac{p^A(i+1)-p^A(i)}{\Delta z} \tag{3.71}$$

$$p^A = RT^A(c^A_{H_2} + c^A_{H_2O}) \tag{3.72}$$

$$(\rho u)^A = c^A_{H_2} h_{H_2}(T^A) + c^A_{H_2O} h_{H_2O}(T^A) - p^A, \tag{3.73}$$

where $v^A(i)$ and $p^A(i)$ correspond to v^A and $p^A(i)$ in node i, and $p^A(i+1)$ in node $i+1$. These variables have been defined together with the hydrogen and water concentrations $c^A_{H_2}$ and $c^A_{H_2O}$, as well as the anode temperature T^A, solid parts temperature T^S, hydrogen and water flows to the other layers $\dot{n}^A_{H_2}$ and $\dot{n}^A_{H_2O}$ and species enthalpies $h_{H_2}(T^A)$ and $h_{H_2O}(T^A)$. With all this information the corresponding differential equations are presented:

$$\frac{\partial c^A_{H_2}}{\partial t} = -\frac{v^A(i)c^A_{H_2}(i) - v^A(i-1)c^A_{H_2}(i-1)}{\Delta z} - \frac{\dot{n}^A_{H_2}}{\delta^A} \tag{3.74}$$

$$\frac{\partial c^A_{H_2O}}{\partial t} = -\frac{v^A(i)c^A_{H_2O}(i) - v^A(i-1)c^A_{H_2O}(i-1)}{\Delta z} - \frac{\dot{n}^A_{H_2O}}{\delta^A} \tag{3.75}$$

$$\begin{aligned}\frac{\partial(\rho u)^A}{\partial t} = &-\frac{v^A(i)\Big(c^A_{H_2}(i)h_{H_2}(T^A)(i) + c_{H_2O}(i)^A h_{H_2O}(T^A)(i)\Big)}{\Delta z} \\ &+ \frac{v^A(i-1)\Big(c^A_{H_2}(i-1)h_{H_2}(T^A)(i-1) + c_{H_2O}(i-1)^A h_{H_2O}(T^A)(i-1)\Big)}{\Delta z} \\ &+ \lambda^A \frac{T^A(i+1) - 2T^A(i) + T^A(i-1)}{\Delta z^2} + \frac{\alpha_1}{\delta^A}\big(T^S(i) - T^A(i)\big) \\ &- \frac{1}{\delta^A}\Big(\dot{n}^A_{H_2}h_{H_2}(T^A)(i) + \dot{n}^A_{H_2O}h_{H_2O}(T^A)(i)\Big)\end{aligned} \tag{3.76}$$

Enthalpies $h_{H_2}(T^A)$ and $h_{H_2O}(T^A)$ are calculated referred to temperature using the specific heat approximation for computational reasons as follows:

$$h_{H_2}(T^A) = c_p^{H_2}T^A \tag{3.77}$$

$$h_{H_2O}(T^A) = c_p^{H_2O}T^A \tag{3.78}$$

Their boundary conditions are the following:

- $v^A c^A_{H_2}\big|_{0,t} = \dot{n}^A_{H_2,in}$
- $v^A c^A_{H_2O}\big|_{0,t} = \dot{n}^A_{H_2O,in}$
- $\dot{n}^A_{H_2,in}h_{H_2}(T^A_{in}) + \dot{n}^A_{H_2O,in}h_{H_2O}(T^A_{in}) = v^A\Big(\, c^A_{H_2}h_{H_2}(T^A)\big|_{0,t} + c^A_{H_2O}h_{H_2O}(T^A)\big|_{0,t}\Big) - \lambda^A \frac{\partial T^A}{\partial z}\Big|_{0,t}$
- $p^A(L_z,t) = p^{amb}$
- $\lambda^A \frac{\partial T^A}{\partial z}\Big|_{L_z,t} = 0$

These equations calculate $c^A_{H_2}$, $c^A_{H_2O}$, p^A using variables $\dot{n}^A_{H_2}$ and $\dot{n}^A_{H_2O}$ coming from the anode gas diffusion layer.

3.5.2 Cathode channels equations discretisation

An analogous procedure is applied for the cathode equations. The system equations to be codified can be divided in algebraic and differential equations. The algebraic ones to define gas velocities v^C, gas pressures p^C and internal energy $(\rho u)^C$ are:

$$v^C(i) = -K^C \frac{p^C(i+1) - p^C(i)}{\Delta z} \tag{3.79}$$

$$p^C = RT^C(c^C_{O_2} + c^C_{N_2} + c^C_{H_2O}) \tag{3.80}$$

$$(\rho u)^C = c^C_{O_2} h_{O_2}(T^C) + c^C_{N_2} h_{N_2}(T^C) + c^C_{H_2O} h_{H_2O}(T^C) - p^C, \tag{3.81}$$

where $v^C(i)$ and $p^C(i)$ correspond to v^C and $p^C(i)$ in node i, and $p^C(i+1)$ in node $i+1$. Analogous variables have been defined such as the oxygen, nitrogen and water concentrations $c^C_{O_2}$, $c^C_{N_2}$ and $c^C_{H_2O}$, as well as the anode temperature T^C, solid parts temperature T^S, hydrogen and water flows to the other layers $\dot{n}^C_{O_2}$ and $\dot{n}^C_{H_2O}$ and species enthalpies $h_{O_2}(T^C)$, $h_{N_2}(T^C)$ and $h_{H_2O}(T^C)$. With all this information the corresponding differential equations are presented:

$$\frac{\partial c^C_{O_2}}{\partial t} = -\frac{v^C(i)c^C_{O_2}(i) - v^C(i-1)c^C_{O_2}(i-1)}{\Delta z} - \frac{\dot{n}^C_{O_2}}{\delta^C} \tag{3.82}$$

$$\frac{\partial c^C_{H_2O}}{\partial t} = -\frac{v^C(i)c^C_{H_2O}(i) - v^C(i-1)c^C_{H_2O}(i-1)}{\Delta z} - \frac{\dot{n}^C_{H_2O}}{\delta^C} \tag{3.83}$$

$$\begin{aligned}\frac{\partial (\rho u)^C}{\partial t} = &-\frac{v^C(i)\Big(c^C_{O_2}(i)h_{O_2}(T^C)(i) + c^C_{H_2O}(i)h_{H_2O}(T^C)(i)\Big)}{\Delta z} \\ &+ \frac{v^C(i-1)\Big(c^C_{O_2}(i-1)h_{O_2}(T^C)(i-1) + c^C_{H_2O}(i-1)h_{H_2O}(T^C)(i-1)\Big)}{\Delta z} \\ &+ \lambda^C \frac{T^C(i+1) - 2T^C(i) + T^C(i-1)}{\Delta z^2} + \frac{\alpha_1}{\delta^C}\big(T^S(i) - T^C(i)\big) \\ &- \frac{1}{\delta^C}\Big(\dot{n}^C_{O_2}h_{O_2}(T^C)(i) + \dot{n}^C_{H_2O}h_{H_2O}(T^C)(i)\Big)\end{aligned} \tag{3.84}$$

Enthalpies $h_{O_2}(T^C)$, $h_{N_2}(T^C)$ and $h_{H_2O}(T^C)$ are calculated referred to temperature

using the specific heat approximation for computational reasons as follows:

$$h_{O_2}(T^C) = c_p^{O_2} T^C \tag{3.85}$$

$$h_{N_2}(T^C) = c_p^{N_2} T^C \tag{3.86}$$

$$h_{H_2O}(T^C) = c_p^{H_2O} T^C \tag{3.87}$$

Their boundary conditions are the following:

- $v^C c_{O_2}^C\big|_{0,t} = \dot{n}_{O_2,in}^C$
- $v^C c_{H_2O}^C\big|_{0,t} = \dot{n}_{H_2O,in}^C$
- $\dot{n}_{O_2O,in}^C h_{O_2}(T_{in}^C) + \dot{n}_{H_2O,in}^C h_{H_2O}(T_{in}^C) = v^C\Big(c_{O_2}^C h_{O_2}(T^C)\big|_{0,t} + c_{H_2O}^C\, h_{H_2O}(T^C)\big|_{0,t}\Big) - \lambda^C \frac{\partial T^C}{\partial z}\Big|_{0,t}$
- $p^C(L_z,t) = p^{amb}$
- $\lambda^C \frac{\partial T^C}{\partial z}|_{L_z,t} = 0$

These equations calculate $c_{O_2}^C$, $c_{N_2}^C$, $c_{H_2O}^C$, p^C using variables $\dot{n}_{O_2}^C$, $\dot{n}_{N_2}^C$ and $\dot{n}_{H_2O}^C$ coming from the anode gas diffusion layer.

3.5.3 Solid part energy balance equations discretisation

Solid parts of the fuel cells present an energy balance which can be discretised similarly:

$$\begin{aligned}\delta^S \frac{\partial(\rho e)^S}{\partial t} &= \dot{n}_{H_2}^A h_{H_2}(T^A) + \dot{n}_{H_2O}^A h_{H_2O}(T^A) + \dot{n}_{O_2}^C h_{O_2}(T^C) + \dot{n}_{N_2}^C h_{N_2}(T^C) + \\ &+ \dot{n}_{H_2O}^C h_{H_2O}(T^C) + \alpha_1\big((T^A - T^S) + (T^C - T^S)\big) + \alpha_2(T_{cool} - T^S) + \\ &+ \lambda^S \delta^S \frac{T^S(i+1) - 2T^S(i) + T^S(i-1)}{\Delta z^2} - (\Phi^C - \Phi^A) i^M \end{aligned} \tag{3.88}$$

$$\begin{aligned}\delta^S (\rho e)^S &= \delta^S (\rho u)^S + C^A \delta^{AC} \frac{\Delta \Phi^{A2}}{2} + C^C \delta^{CC} \frac{\Delta \Phi^{C2}}{2} \\ &= (\delta^S - \delta^M)(\rho h)^S(T^S) + \delta^M (\rho h)^M(T^S) + \delta^M \rho_{H_2O}^M h_{H_2O}(T^S) + \\ &+ C^A \delta^{CA} \frac{\Delta \Phi^{A2}}{2} + C^C \delta^{CC} \frac{\Delta \Phi^{C2}}{2} \end{aligned} \tag{3.89}$$

Their boundary conditions for T^S are:

$$\frac{\partial T^S}{\partial z}\bigg|_{0,t} = \frac{\partial T^S}{\partial z}\bigg|_{L_z,t} = 0 \tag{3.90}$$

3.6 Steady-state values analysis

Once the HT-PEMFC model has been built it is ready to be simulated. Different simulations can be carried on to check the behaviour of the main physical variables. It is important to notice that the distributed model has 10 state variables per node. For this reason, a study of the minimum nodes needed is also necessary.

3.6.1 Mesh study

As it is well known, solving differential equations analytically is the only way to obtain an exact solution for any point in the studied geometry. However, only some differential equations can be solved analytically and, in the case of partial differential equations like the ones studied, an approximation using numerical methods is needed. In the studied case, finite differences approximation has been applied. Nevertheless, a minimum number of nodes is needed to ensure the approximation is close enough to the hypothetical solution found analytically.

If we consider the system has boundary conditions on both sides, which is generally true for most equations listed, a minimum number of 3 nodes is needed. However, this may leave only one free central node to be calculated with the information obtained by its neighbouring nodes and even some equations with boundary conditions like first derivative equal to zero would not give realistic results. For this reason and to guarantee the existence of a central node which can be used to study the system behaviour far away from both geometry edges 5 nodes are selected as a starting point of the mesh size study. Simulating the model discretising it with 5 nodes and setting the voltage to $U = 0.7V$ and $T_{cool} = 423.15K$ the following solutions for the central node of the geometry are obtained in Figure 3.11 to 3.11:

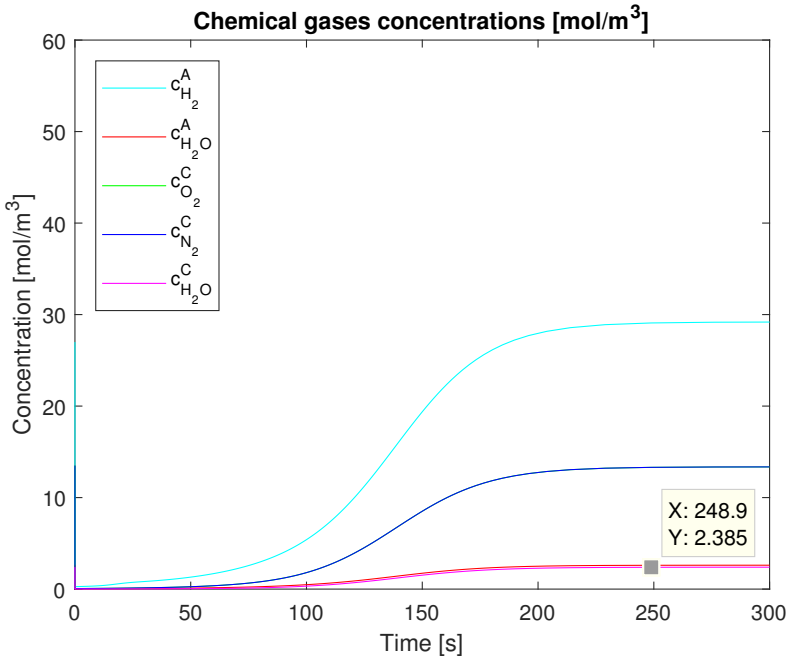

Figure 3.8: Concentrations of all gases on the anode and cathode channels (5 nodes)

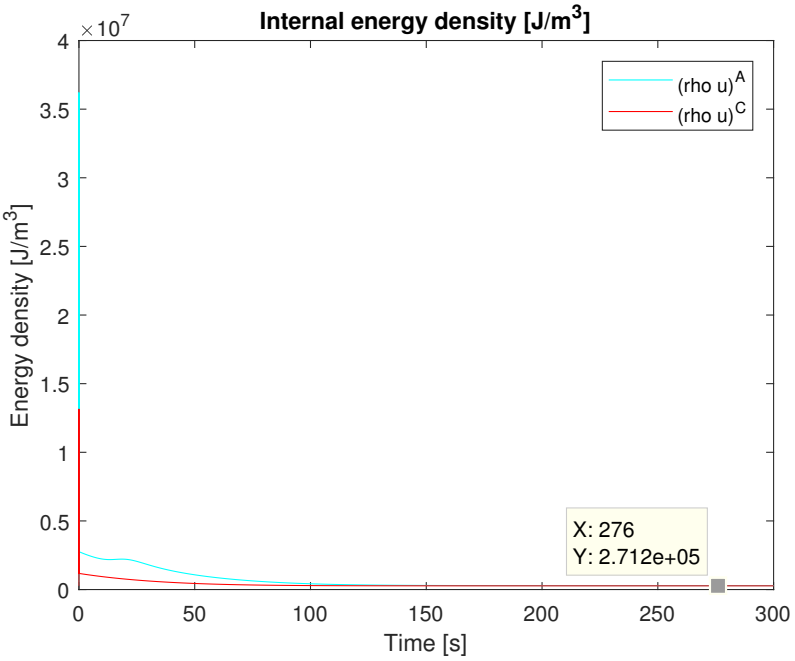

Figure 3.9: Internal energy density on anode and cathode (5 nodes)

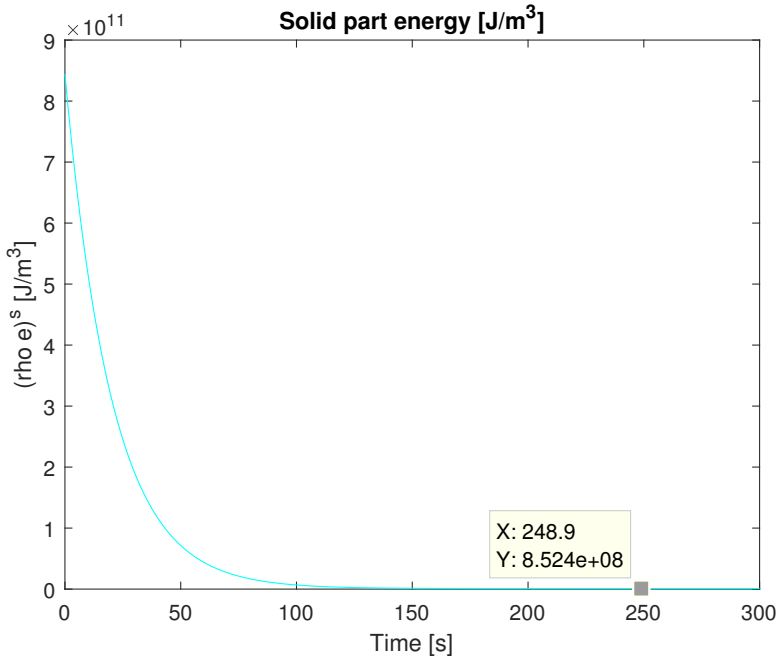

Figure 3.10: Solid part energy density (5 nodes)

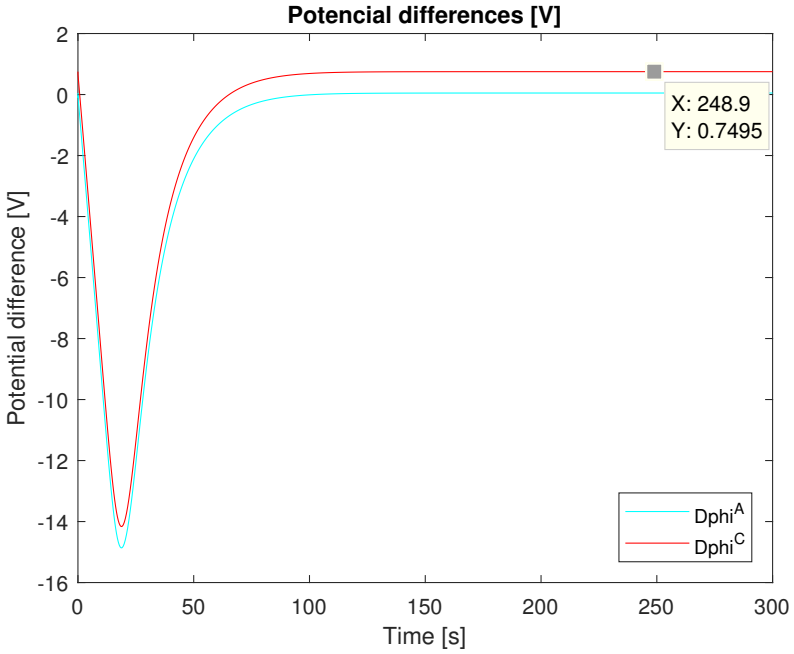

Figure 3.11: Potential difference on anode and cathode (5 nodes)

The same study can be done for more nodes, for example 21, to see if the central node has a similar value (Figures 3.12 to 3.15):

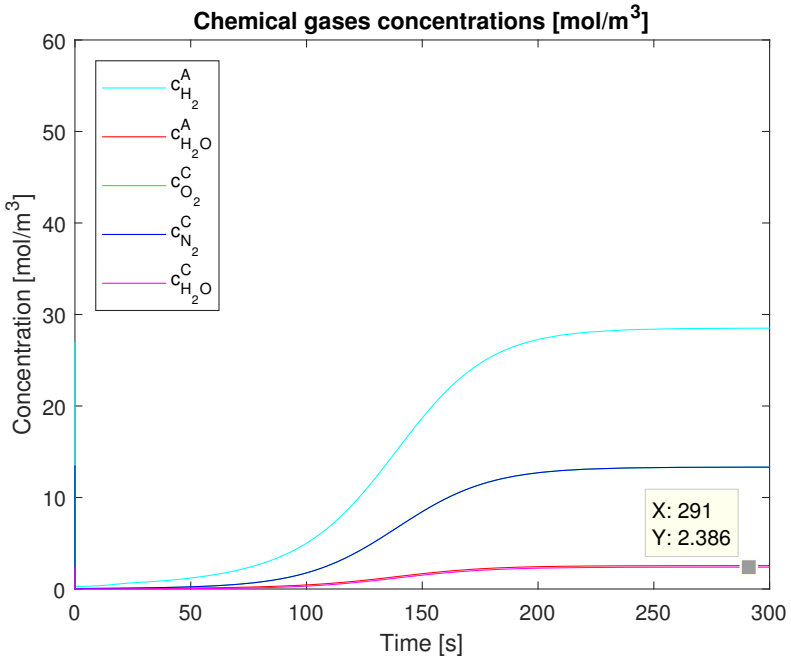

Figure 3.12: Concentrations of all gases on the anode and cathode channels (21 nodes)

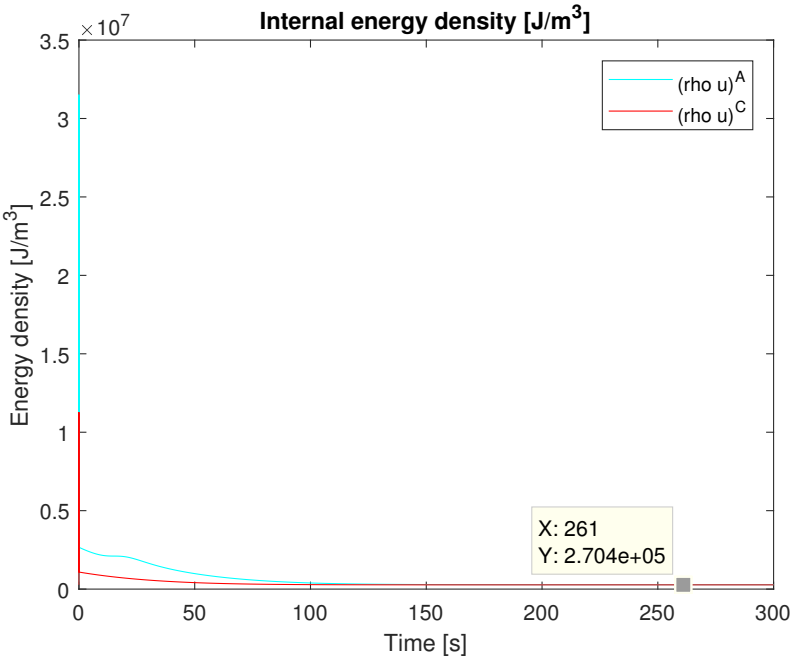

Figure 3.13: Internal energy density on anode and cathode (21 nodes)

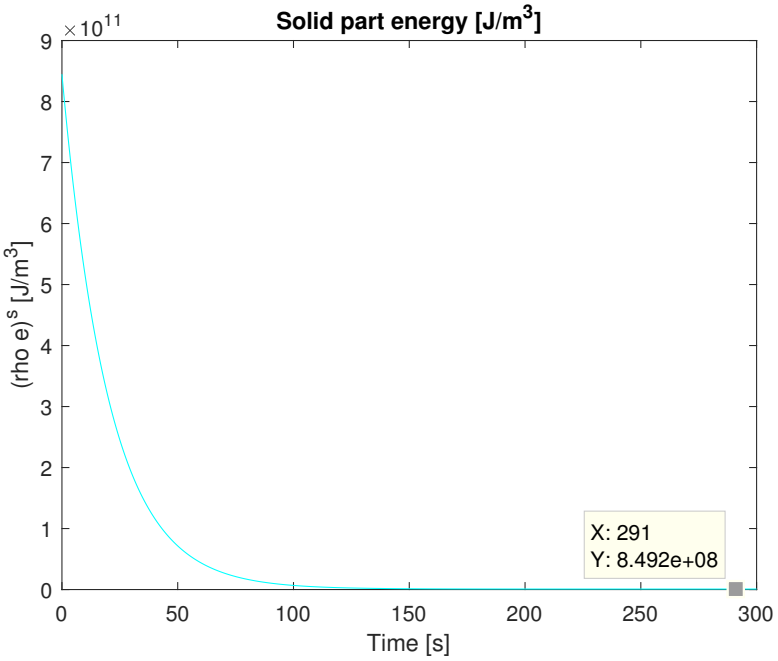

Figure 3.14: Solid part energy density (21 nodes)

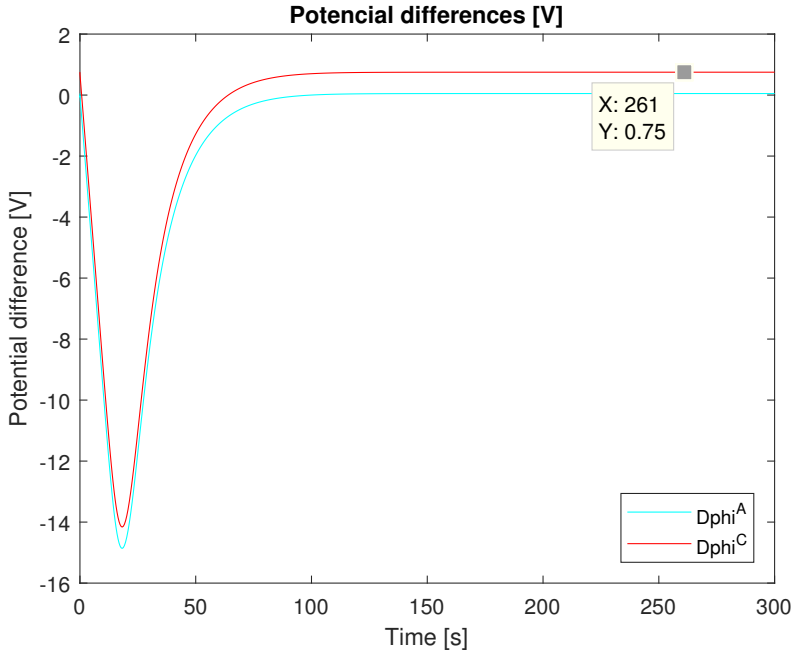

Figure 3.15: Potential difference on anode and cathode (21 nodes)

After a high overshoot when numerically solving the ODE (even though the initial values are close to the steady-state ones) the final values are reached and are similar to the ones when using 5 nodes.

3.6.2 Equilibrium points

Once the model has been defined a set of equilibrium points for given inputs need to be obtained. First of all, the right hand side of the model spatially-discretised equations can be organised for each node in a function F_n^i of the geometry such that:

$$\begin{aligned} \frac{\partial \overrightarrow{\mathbf{x}}}{\partial t} &= F_n^i(c_{H_2}^A, c_{H_2O}^A, (\rho u)^A, c_{O_2}^C, c_{N_2}^C, c_{H_2O}^C, (\rho u)^C, \delta^S(\rho e)^S, \Delta\Phi_A, \Delta\Phi_C) \\ \overrightarrow{\mathbf{x}} &= (c_{H_2}^A, c_{H_2O}^A, (\rho u)^A, c_{O_2}^C, c_{N_2}^C, c_{H_2O}^C, (\rho u)^C, \delta^S(\rho e)^S, \Delta\Phi_A, \Delta\Phi_C)^T \end{aligned} \tag{3.91}$$

Each function F_n^i for each node can be concatenated to build the function for the global system of equations F_n as $F_n = [F_n^1(1) \cdots F_n^N(1)\, F_n^1(2) \cdots F_n^N(2) \cdots F_n^1(10) \cdots F_n^N(10)]^T$.

Once the system has been defined and its equations written in a vector function F_n, an equilibrium point can be found solving the system of nonlinear equations re-

sulting of imposing that the left-hand side of equation (3.91) is zero. The result after concatenating equations for all nodes i is equation (3.92):

$$\mathbf{0} = F_n(c^A_{H_2}, c^A_{H_2O}, (\rho u)^A, c^C_{O_2}, c^C_{N_2}, c^C_{H_2O}, (\rho u)^C, \delta^S(\rho e)^S, \Delta\Phi_A, \Delta\Phi_C) \tag{3.92}$$

For different sets of input variables equilibrium points will change. Some interesting variables which are important are temperatures for the inner layers and the previously defined polarisation curve relating voltage and current. For a node distribution of 5 nodes the relationship between T^S, T^A and T^C (on central node 3) with voltage is the one seen in Figure 3.16:

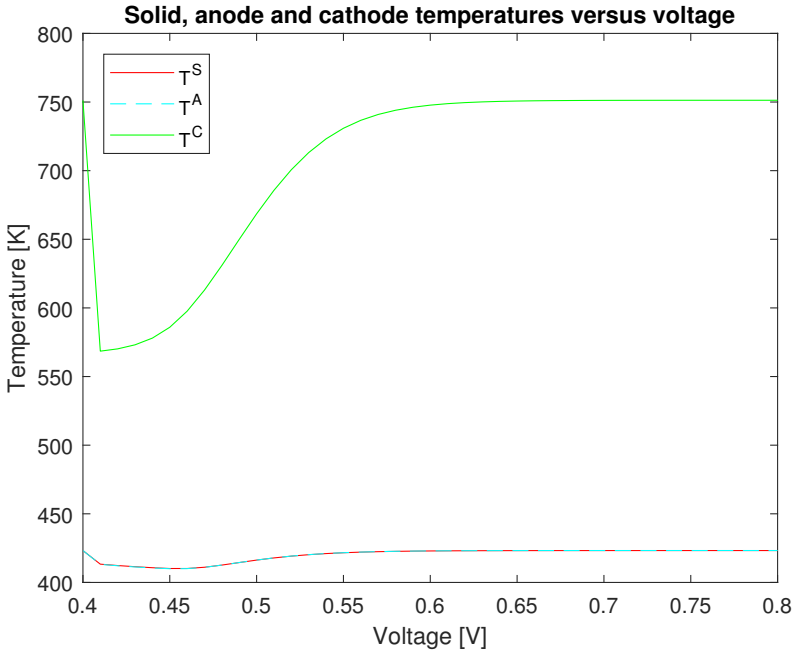

Figure 3.16: Solid parts, anode and cathode central node temperature with respect to voltage (5 nodes)

The same study can be done with 21 nodes and it is shown in Figure 3.17:

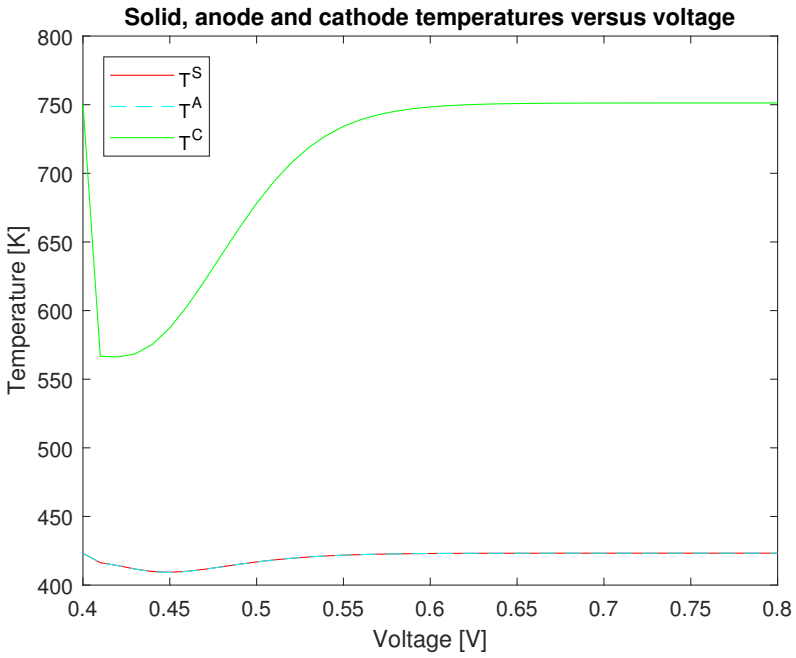

Figure 3.17: Solid parts, anode and cathode central node temperature with respect to voltage (21 nodes)

It can be seen that both curves for 5 and 21 nodes are almost the same. Finally, polarisation curve for 5 nodes is depicted in Figure 3.18:

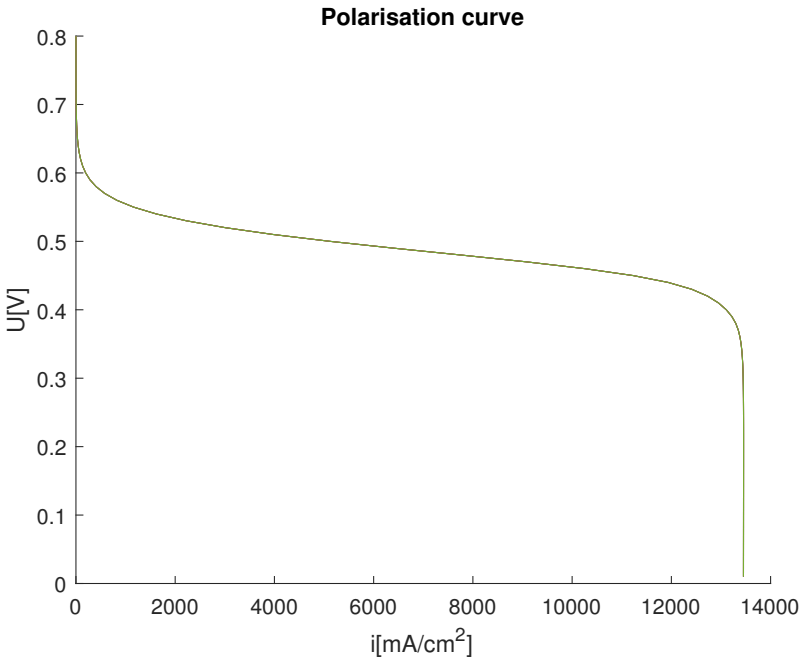

Figure 3.18: Polarisation curve (5 nodes)

Each of these equilibrium points can be used to perform a linearisation of the system around it so that a state-space representation can be carried on.

3.7 Linearised model

3.7.1 Linearisation procedure

As mention above, to linearise the studied system, an equilibrium point must be found solving the system of equations for all nodes in the one-dimensional geometry. Once an equilibrium point has been found, the linearised state-space can be calculated. State-space matrices are a result of linearising the system's equations around the equilibrium

point $\mathbf{x}^*$, $\mathbf{u}^*$ as seen in equations (6.15) and (3.94):

$$\begin{aligned}
\frac{d\Delta x(t)}{dt} &= \mathbf{A}\Delta\mathbf{x}(t) + \mathbf{B}\Delta\mathbf{u}(t) \\
\Delta y(t) &= \mathbf{C}\Delta\mathbf{x}(t) + \mathbf{D}\Delta\mathbf{u}(t) \\
\Delta\mathbf{x}(t) &= \mathbf{x}(t) - \mathbf{x}^* \\
\Delta\mathbf{u}(t) &= \mathbf{u}(t) - \mathbf{u}^* \\
\Delta\mathbf{y}(t) &= \mathbf{y}(t) - \mathbf{y}^*
\end{aligned} \tag{3.93}$$

$$\mathbf{A} = \left[\begin{matrix} \frac{\partial F_n^1}{\partial x_n^1} & \cdots & \frac{\partial F_n^1}{\partial x_n^n} \\ \vdots & \ddots & \vdots \\ \frac{\partial F_n^n}{\partial x_n^1} & \cdots & \frac{\partial F_n^n}{\partial x_n^n} \end{matrix}\right]\Bigg|_{\mathbf{x}^*,\mathbf{u}^*}, \quad \mathbf{B} = \left[\begin{matrix} \frac{\partial F_n^1}{\partial u_n^1} & \cdots & \frac{\partial F_n^1}{\partial u_n^m} \\ \vdots & \ddots & \vdots \\ \frac{\partial F_n^n}{\partial u_n^1} & \cdots & \frac{\partial F_n^n}{\partial u_n^m} \end{matrix}\right]\Bigg|_{\mathbf{x}^*,\mathbf{u}^*} \tag{3.94}$$

Matrix A corresponds to the previously calculated jacobian, but it can also be calculated another way, which will allow us to compare and verify the presented method. This is done by means of a Matlab command able to call a Simulink model and calculating its state-space model called $[A, B, C, D] = linmod('SimulinkModel')$. For the case studied, variables in the model have the following meaning:

- $\mathbf{x}(t) = [c_{H_2}^A, c_{H_2O}^A, (\rho u)^A, c_{O_2}^C, c_{N_2}^C, c_{H_2O}^C, (\rho u)^C, \delta^S(\rho e)^S, \Delta\Phi_A, \Delta\Phi_C]^T$ is the vector of state variables.
- $\mathbf{u}(t) = [U, T_{cool}]^T$ or $\mathbf{u}(t) = [I, T_{cool}]^T$ are the inputs.
- $\mathbf{y}(t) = I$ or $\mathbf{y}(t) = U$ is the output.

3.7.2 Stability, controllability and observability

Once the system has been linearised around an specific equilibrium point the resulting linearised system needs to be analysed. To do so, the main characteristics typically studied are:

- *Stability*: ability of a system to restore the original condition after it is disturbed.
- *Controllability*: ability to move a system, i.e. its state variables, around the region in which it operates.

- *Observability*: ability to know the system internal states from its external outputs, i.e. sensors.

All three conditions need to be met in order to have a reliable linearised model that can be controlled in the future. Firstly, stability in state-space systems like the one from equation (6.15) is checked computing the real part $Re(\lambda_i)$ of eigenvalues of the matrix $\mathbf{A} \in \mathbb{R}^{n \times n}$. Conditions are the following:

- *Stable system*: if all $Re(\lambda_i) < 0$, $i = 1, \ldots, n$
- *Marginably stable system*: if some $Re(\lambda_i) = 0$ and the rest $Re(\lambda_i) < 0$, $i = 1, \ldots, n$
- *Unstable system*: if one or more $Re(\lambda_i) > 0$, $i = 1, \ldots, n$

Secondly, one of the main ways of checking a state-space system controllability is analysing the so called controllability matrix $\mathbf{M_{con}}$, defined as follows:

$$\mathbf{M_{con}} = [\mathbf{B} \quad \mathbf{AB} \quad \cdots \quad \mathbf{A}^{n-1}\mathbf{B}], \tag{3.95}$$

where $\mathbf{A} \in \mathbb{R}^{n \times n}$ and $\mathbf{B} \in \mathbb{R}^{n \times m}$ are state-space matrices from equation (6.15). The system is said to be controllable if $rank(M_{con}) = n$. Finally, observability is studied analysing the following controllability matrix $\mathbf{M_{obs}}$:

$$\mathbf{M_{obs}} = \begin{bmatrix} \mathbf{C} \\ \mathbf{CA} \\ \vdots \\ \mathbf{CA}^{n-1} \end{bmatrix}, \tag{3.96}$$

where $\mathbf{A} \in \mathbb{R}^{n \times n}$ and $\mathbf{C} \in \mathbb{R}^{q \times n}$ are state-space matrices from equation (6.15). The system is said to be observable if $rank(\mathbf{M_{con}}) = n$. If $rank(\mathbf{M_{con}}) \neq n$ it means that the extra number of sensors needed is:

$$N_{sensors} = n - rank(\mathbf{M_{con}}) \tag{3.97}$$

However, depending on the system, these extra $N_{sensors}$ can be too expensive to install or even impossible in some cases. Other alternatives like implementing observers need to be explored in those cases.

3.7.3 Linearised model around different equilibrium points

Once all linearisation process has been defined a set of linearised models around different equilibrium points of the studied system is performed. More specifically, input $\mathbf{u}(t) = [U, T_{cool}]^T$ is set to different values establishing a mesh for variables U and T_{cool} and its resulting linearised models studied. One of the possible analyses to be done is a study of the maximum and minimum real part of their eigenvalues distribution for all systems. These are shown in Figure 3.19 and 3.20.

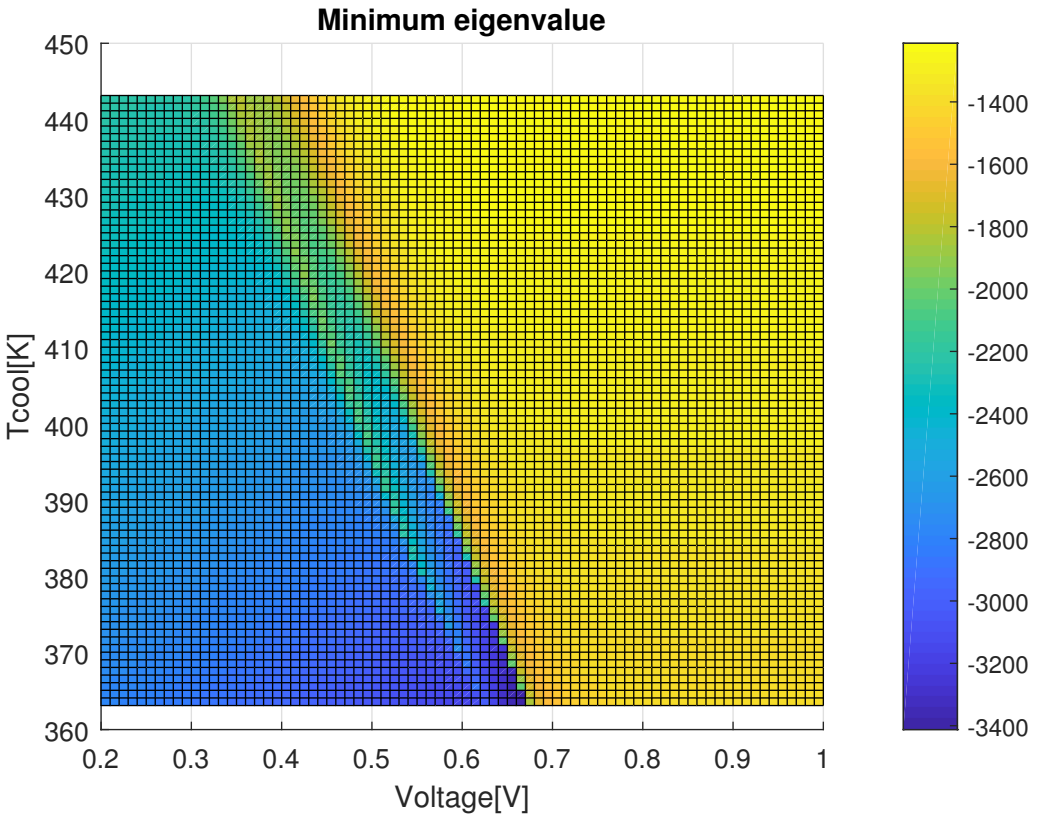

Figure 3.19: Minimum real part of eigenvalues corresponding to different linearised systems

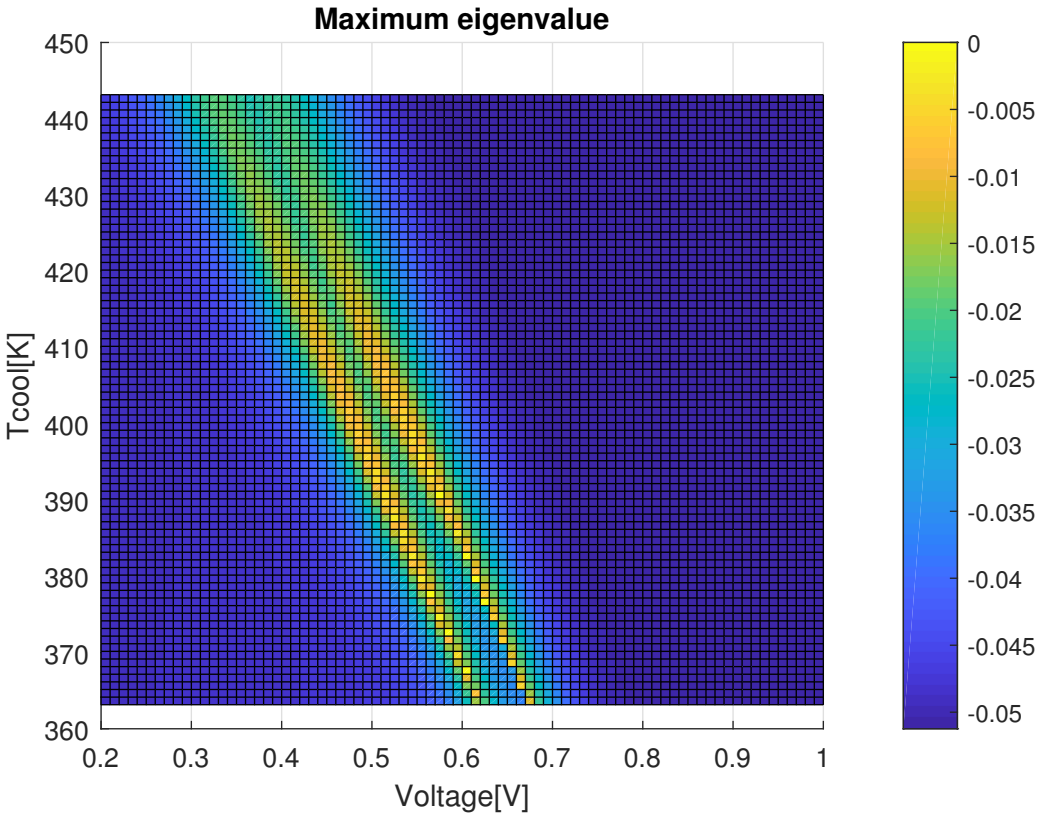

Figure 3.20: Maximum real part of eigenvalues corresponding to different linearised systems

Analysing figure 3.20 it can be seen that all zones have all eigenvalues λ_i with $Re(\lambda_i) < 0$, i.e. stable linearised models. This matches with the stable results obtained for the nonlinear system around the same operation points of this zone.

3.7.3.1 Comparison between linearised and nonlinear models around its equilibrium points

As explained in previous sections fuel cells' polarisation curve presents three different regions:

- *Activation zone*: corresponding to low current density i_M where chemical reaction's activation losses are the most important ones.

- *Ohmic zone*: corresponding to intermediate values of current density i_M where electric ohmic losses, i.e resistive, are the most dominate.
- *Concentration zone*: corresponding to high current density i_M where transport concentration losses are predominate.

If three equilibrium points (one per each zone in the polarisation curve) are selected the corresponding linearised models can be calculated. The behaviour of these linearised models is compared to the one of the original nonlinear model. The equilibrium points are selected through inputs U and T_{cool}:

- *Concentration zone*: $U^* = 0.3$ V and $T^*_{cool} = 423.15$ K
- *Ohmic zone*: $U^* = 0.5$ V and $T^*_{cool} = 423.15$ K
- *Activation zone*: $U^* = 0.7$ V and $T^*_{cool} = 423.15$ K

The block diagram to compare both systems where u is the input, x is the state vector and y the output (and u^*, x^* and y^* its corresponding equilibrium points) is the one shown below:

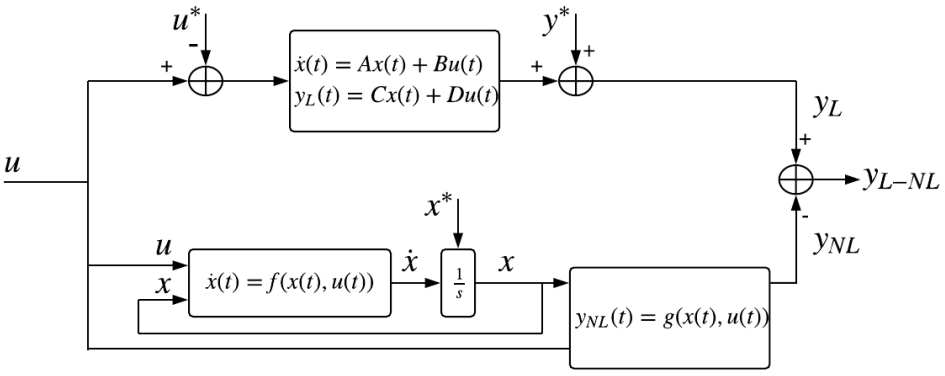

Figure 3.21: Block diagram to compute linear and nonlinear systems around an equilibrium point

The value of $y_{L-NL} = y_L - y_{NL}$ for all three different points are the ones in figure 3.22:

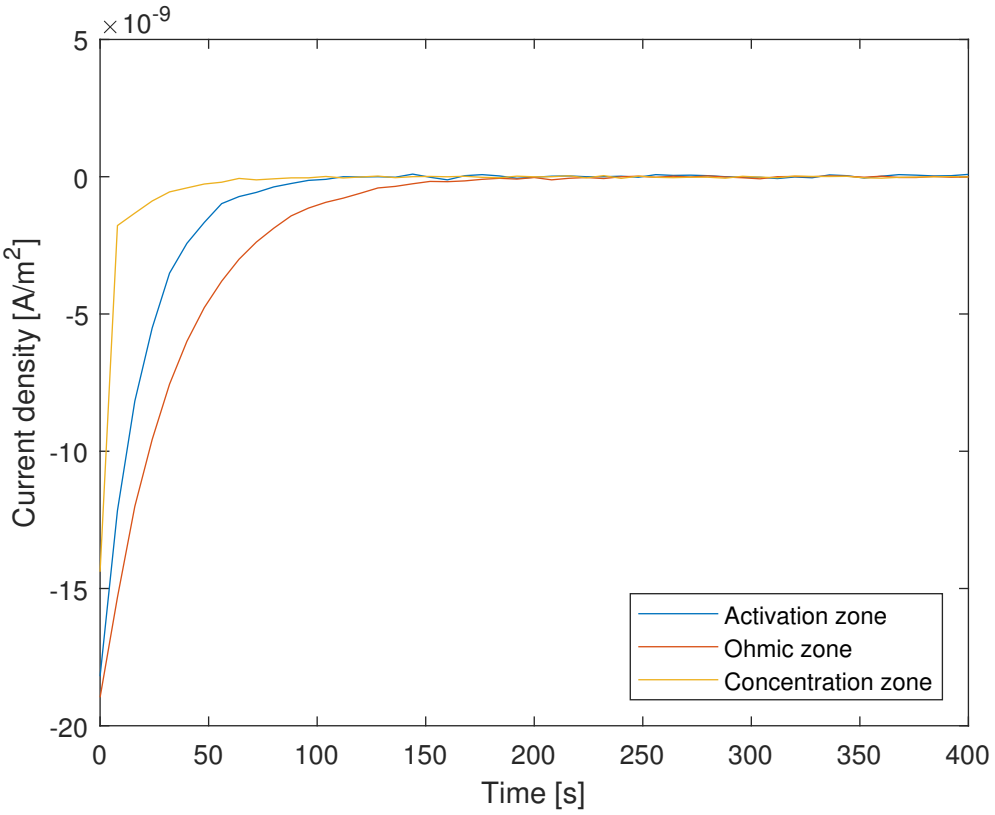

Figure 3.22: Output differences of linear and nonlinear systems around three equilibrium points

Looking at all three cases depicted it can be seen that results of the linearised systems and the original nonlinear system match. Therefore, linearised systems match the nonlinear one around the corresponding equilibrium point as expected. From now on, we can work with a family of equilibrium points instead of the nonlinear model, which will be very useful, especially for control design.

3.7.3.2 Selection of the necessary equilibrium points

When selecting a set of equilibrium points corresponding to this system, this cannot be done analytically. This procedure should, then be done following an iterative process fixing variables such as fuel cell voltage or current (one or the other, leaving one free). Different simulations of the system of differential equations presented are calculated, starting from reasonable initialisation points. These points have been obtained using

initialisation points obtained with a finite-elements simulation computed with program Comsol®. This program is able to impose a fuel cell's geometry, electrochemical equations, fluid dynamics and thermal characteristics, similarly to what's done in [64], where other finite-elements programs are used. From these starting points, as close as possible to real equilibrium points, the system of differential equations is simulated till variables reach stability. These stable variables are then imposed in the system to ensure they are real equilibrium points, that is, all equations are equal to zero when equilibrium points are evaluated.

However, although all initialisation points are selected using results from the finite-elements Comsol®, some variables, specially temperature values (proportional to energy) in nodes where boundary conditions act, tend to diverge and stabilise around values which change to abruptly. This lack of reliability, together with excessive computational time related to the dimension of the space to be explored to find the equilibria (10 times the number of nodes N), makes this kind of distributed models a bad alternative for control methods that are supposed to work online and update continuously, as it will be explained in later chapters. Even though model reduction techniques have been explored ([8, 32, 39, 59, 67, 85, 91, 93]) to reduce this system's complexity and thus be able to implement distributed models in control systems, equilibrium points are difficult to search for multiple scenarios, and switching from one to the other (when doing control) would be too cumbersome. Due to all these reasons, a simpler model (non distributed) of the HT-PEMFC needs to be used and integrated with the rest of models that build up the global CHP system studied. This global CHP model is presented with equations for all elements in the following chapter.

Chapter 4

Simulation model

All the world's a stage,

And all the men and women merely players

From *As You Like It*, by William Shakespeare

After knowing about the physical processes going on in HT-PEMFC and its possibilities, the global CHP system must be modelled integrating all its parts. In this chapter, the global system components are detailed and its submodels arranged.

4.1 System's architecture and components

4.1.1 System description

In order to tackle the problem a model of the global system is needed. According to several authors ([3, 30, 48, 90]), components of the CHP system such as a heat exchanger, a battery and water tanks are needed for most applications of this kind. Therefore, this CHP system model should include elements in Figure 4.1. Their roles in the system are [90]

- *HT-PEMFC*: able to generate heat and electrical energy.
- *PEM electrolyser*: able to generate generate split water into hydrogen and oxygen when connected to a voltage source.

- *Photovoltaic cell*: able to generate generate electrical power (direct current) from sun's irradiance.
- *DC/DC converter*: establishes the desired level of voltage.
- *DC/AC converter*: transforms direct current to alternating current and establishes the desired level of voltage.
- *Hydrogen tank*: stores pressurised hydrogen gas generated by the electrolyser.
- *Battery*: stores electrical energy to be supplied depending on the demand.
- *Storage tank*: stores water to generate heat for space heating.
- *Hot water tank*: stores and supplies hot water to be used by humans.

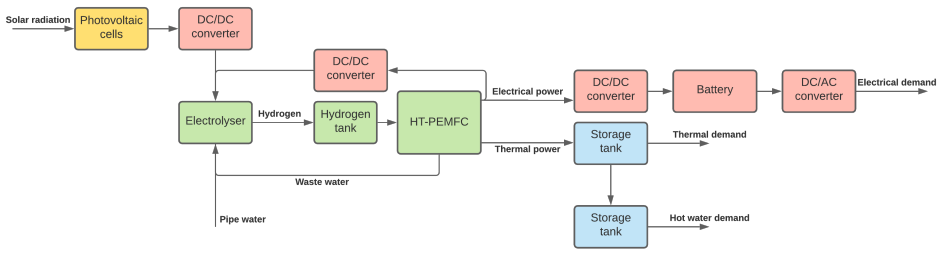

Figure 4.1: CHP system and its elements

4.1.2 System model

This system can be modelled differently depending on the simplicity of the model needed and certain computations can only be carried on when the model is simple enough. Among these model alternatives, whether a system is linear or nonlinear is one of the ways to classify them. It is clear that linearising a model which is nonlinear by nature makes the model more simple and less reliable, but can be more useful for control applications, among others. Considering all this, the Matlab/Simulink model designed is the one from Figure 4.2, whose elements will be detailed in the following sections.

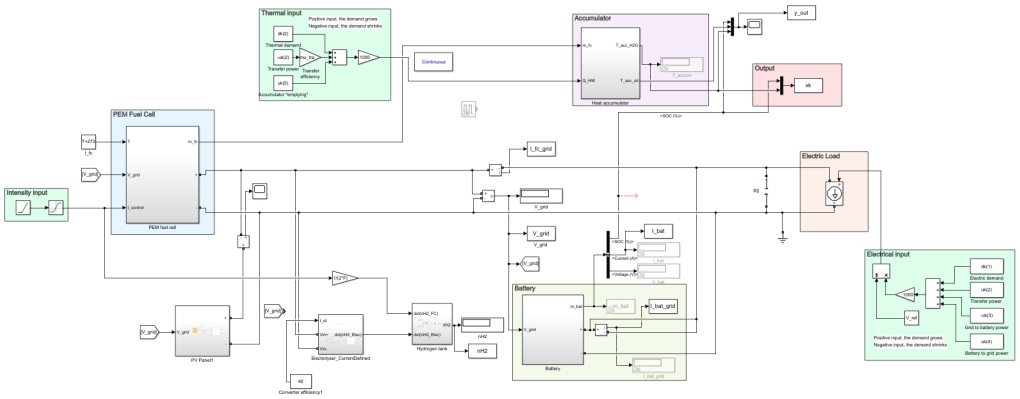

Figure 4.2: Matlab/Simulink model of the whole system

4.1.2.1 HT-PEMFC

Starting with the energy generator, the fuel cell, figure 3.4 shows the configuration of the PEMFC. It is important to note that the input to the fuel cell will be the intensity, decided via the controller. In Figure 4.3 the intensity is modelled as a ramp. As explained before, this is due to the fact that big changes in intensity highly deteriorate of the cell.

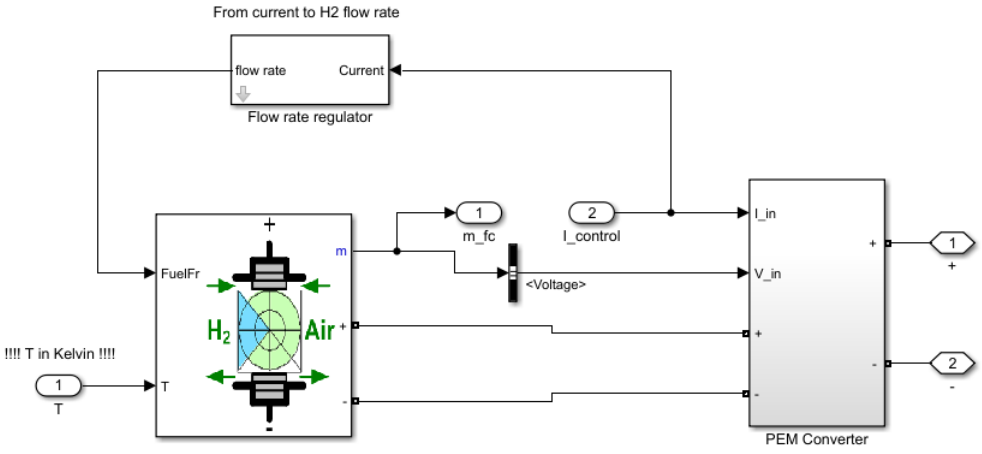

Figure 4.3: Fuel cell Matlab/Simulink model block

Then, on the right, a converter has been placed, connecting the cell with the external grid. Lastly, a block has been designed to input the amount of hydrogen needed, according to the desired intensity.

The model of the fuel cell has been done using the Fuel cell model of the Simscape toolbox. Parameters of the fuel cell can be set, having a total of 6 predefined fuel cells available (Figure 4.4. If the 'Model detail Level' is set to 'Simplified', only the first 3 will be displayed, which correspond to the creation of the polarization curve of the fuel cell. On the other hand, if it is set to 'Detailed', the rest of the options and the 'Signal variation' window will appear, allowing the fuel cell parameters changing over time via inputs to the model.

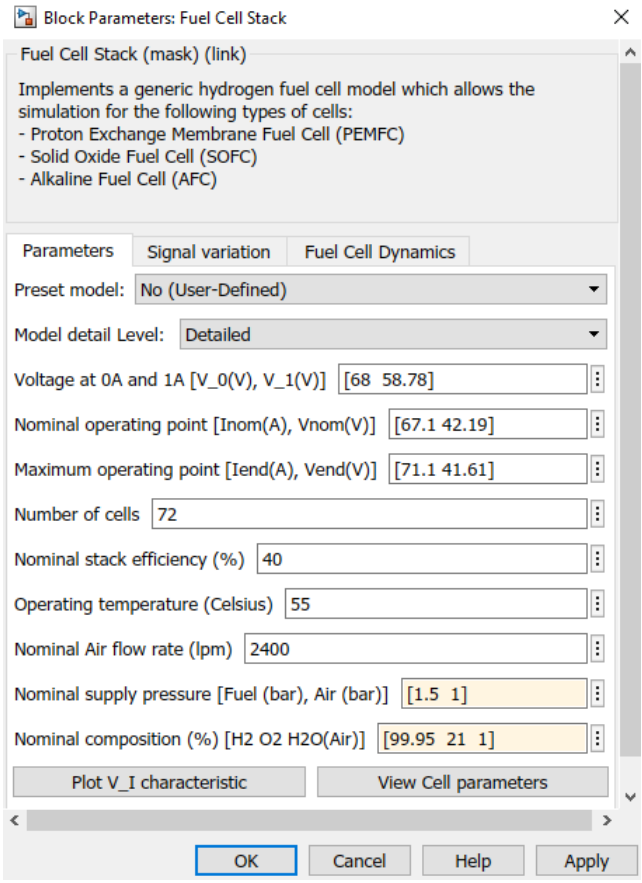

Figure 4.4: Fuel cell Matlab/Simulink model parameters

On the right side, the model of a converter has been created. Due to the fuel cell's

voltage being a function of the intensity, a converter is needed before supplying the produced energy to the grid. As the voltage of the fuel cell is lower than the grid, the converter used will have to be a boost type. The Matlab/Simulink fuel cell model from Figure 4.3 has the structure of Figure 4.5, equivalent to a simple polarisation curve as the one mentioned in previous chapters and a delay T_d to break the algebraic loop.

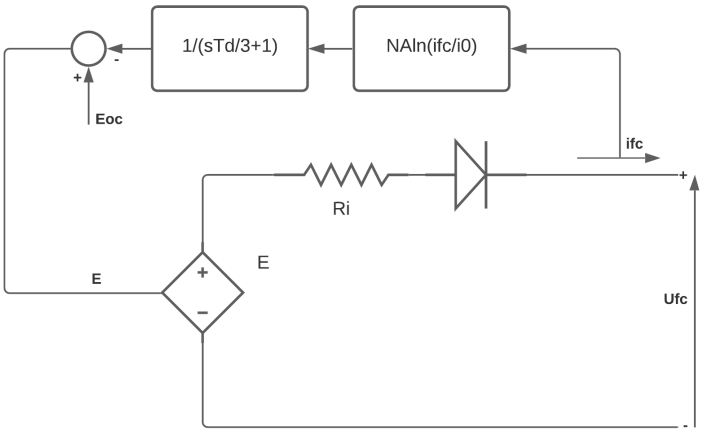

Figure 4.5: Matlab/Simulink fuel cell model equivalent diagram

The model corresponding to Figure 4.5 has the following expressions for variables E_{oc} and i_0:

$$E_{oc} = K_c E_n \tag{4.1}$$

$$i_0 = \frac{zFk(P_{H_2} + P_{O_2})\Delta v}{Rh} e^{-\frac{\Delta G}{RT}}, \tag{4.2}$$

where E_{oc} is the fuel cell open circuit voltage in V, K_c is the voltage constant at nominal condition of operation, E_n is the Nernst voltage in V, i_0 is the exchange current in A, $z = 2$ is the number moles of moving electrons, $F = 96485$ As/mol is Faraday's constant, $k = 1.38 \cdot 10^{-23}$ J/K is Boltzmann's constant, $R = 8.31$ J/(mol K) is the ideal gases constant, $h = 6.626 \cdot 10^{-34}$ Js is Planck's constant, P_{H_2} is hydrogen's pressure in Pa, P_{O_2} is oxygen's pressure in Pa, Δv is the activation barrier volume factor in m^3, ΔG is the size of the activarion barrier depending on the electrode and catalyst in J/mol and T is the operation temperature in K. In the studied case of high-temperature fuel

cells and an oxygen ratio below a certain limit, the expression for Nernst voltage E_n is the one from equation (4.3):

$$E_n = 1.229 + (T - 298)\frac{-44.43}{zF} + \frac{RT}{zF}\ln\left(\frac{P_{H_2}P_{O_2}^{1/2}}{P_{H_2O}}\right) \tag{4.3}$$

Partial pressures P_{H_2} and P_{O_2} can be calculated as follows:

$$P_{H_2} = (1 - U_{fH_2})\chi_{H_2}P_{fuel} \tag{4.4}$$

$$P_{O_2} = (1 - U_{fO_2})\chi_{O_2}P_{air} \tag{4.5}$$

$$P_{H_2O} = (\chi_w + 2\chi_{O_2}U_{fO_2})P_{air}, \tag{4.6}$$

where χ_{H_2} is the hydrogen molar fraction in the fuel, χ_{O_2} is the oxygen molar fractions in the oxidant, χ_w is the water vapour molar fraction in the oxidant, P_{fuel} is the fuel pressure in atm and P_{air} is the cathode air pressure in atm. U_{fH_2} and U_{fO_2} are hydrogen and oxygen conversion rates calculated in equations (4.7) and (4.8) as follows:

$$U_{fH_2} = \frac{n_{H_2}^r}{n_{H_2}^{in}} = \frac{60000RTNi_{fc}}{zFP_{fuel}V_{lpm(fuel)}\chi_{H_2}} \tag{4.7}$$

$$U_{fO_2} = \frac{n_{O_2}^r}{n_{O_2}^{in}} = \frac{60000RTNi_{fc}}{2zFP_{air}V_{lpm(air)}\chi_{O_2}}, \tag{4.8}$$

where $V_{lpm(fuel)}$ is the fuel flow rate in l/min, $V_{lpm(air)}$ is the air flow rate in l/min, N is the number of cells and 60000 is the conversion constant from l/min to m^3/s. Substituting equations (4.7) and (4.8) in equations (4.4) to (4.6) the expressions of pressures P_{H_2}, P_{O_2} and P_{H_2O} as functions of fuel cell's current i_{fc}:

$$P_{H_2} = \left(1 - \frac{60000RTNi_{fc}}{zFP_{fuel}V_{lpm(fuel)}\chi_{H_2}}\right)\chi_{H_2}P_{fuel} \tag{4.9}$$

$$P_{O_2} = \left(1 - \frac{60000RTNi_{fc}}{2zFP_{air}V_{lpm(air)}\chi_{O_2}}\right)\chi_{O_2}P_{air} \tag{4.10}$$

$$P_{H_2O} = \left(\chi_w + 2\chi_{O_2}\frac{60000RTNi_{fc}}{2zFP_{air}V_{lpm(air)}\chi_{O_2}}\right)P_{air} \tag{4.11}$$

These expressions from equations (4.9) to (4.11) can be substituted in equation (4.3)

to obtain the following expression for E_n:

$$\begin{aligned} E_n &= 1.229 + (T - 298)\frac{-44.43}{zF} + \\ &\quad + \frac{RT}{zF}\ln\left(\frac{Num^{fuel}(i_{fc})Num^{air}(i_{fc})}{(\chi_w + 2\chi_{O_2}\frac{60000RTNi_{fc}}{2zFP_{air}V_{lpm(air)}\chi_{O_2}})P_{air}}\right) \\ Num^{fuel}(i_{fc}) &= \left(1 - \frac{60000RTNi_{fc}}{zFP_{fuel}V_{lpm(fuel)}\chi_{H_2}}\right)\chi_{H_2}P_{fuel} \\ Num^{air}(i_{fc}) &= \left(\left(1 - \frac{60000RTNi_{fc}}{2zFP_{air}V_{lpm(air)}\chi_{O_2}}\right)\chi_{O_2}P_{air}\right)^{1/2} \end{aligned} \tag{4.12}$$

Finally, the expression of E_{oc} as a function of i_{fc} is obtained replacing equation (4.12) in equation (4.1):

$$\begin{aligned} E_{oc} &= K_c\left[1.229 + (T - 298)\frac{-44.43}{zF} + \right. \\ &\quad \left. + \frac{RT}{zF}\ln\left(\frac{Num^{fuel}(i_{fc})Num^{air}(i_{fc})}{(\chi_w + 2\chi_{O_2}\frac{60000RTNi_{fc}}{2zFP_{air}V_{lpm(air)}\chi_{O_2}})P_{air}}\right)\right] \\ Num^{fuel}(i_{fc}) &= \left(1 - \frac{60000RTNi_{fc}}{zFP_{fuel}V_{lpm(fuel)}\chi_{H_2}}\right)\chi_{H_2}P_{fuel} \\ Num^{air}(i_{fc}) &= \left(\left(1 - \frac{60000RTNi_{fc}}{2zFP_{air}V_{lpm(air)}\chi_{O_2}}\right)\chi_{O_2}P_{air}\right)^{1/2} \end{aligned} \tag{4.13}$$

Regarding the transfer function added in Figure 4.5, with a defined time of T_d, in the Laplace domain, it is transformed to the time domain in the shape of a state-space representation, naming the output of this block as E_{pre}:

$$\dot{E}_{pre} = -\frac{3}{T_d}E_{pre} + \frac{3}{T_d}NA\ln\left(\frac{i_{fc}}{i_0}\right) \tag{4.14}$$

The electrical circuit from Figure 4.5 is used to obtain the following relationship between variables:

$$U_{fc} = E - R_i i_{fc}, \tag{4.15}$$

where U_{fc} is the fuel cell voltage in V and R_i is the fuel cell's internal resistance in Ω. Variables E, E_{pre} and E_{oc} aforementioned are related the following way:

$$E = E_{oc} - E_{pre} \tag{4.16}$$

Consequently, equation (4.17) arises:

$$U_{fc} = -E_{pre} + E_{oc} - R_i i_{fc} \tag{4.17}$$

Finally, the state-space representation of the fuel cell is defined. Its variables are classified the following way:

- E_{pre} is the state variable.
- i_{fc} is the input variable.
- U_{fc} is the output variable.

Replacing the value of i_0 with the expression of equation (4.2) as well as the values of pressures defined in equations (4.9) to (4.11) the following expression corresponding to the HT-PEMFC state equation is obtained in equation (4.18). Finally, variable E_{oc} is replaced by the expression obtained in equation (4.13) to form the final state-space output equation corresponding to equation (4.19).

$$\begin{aligned}
\dot{E}_{pre} &= -\frac{3}{T_d}E_{pre} + \frac{3}{T_d}NA\ln\left[\frac{Rhi_{fc}}{Den(i_{fc})}\right] \\
Den(i_{fc}) &= zFk\Big(\big(1 - \frac{60000RTNi_{fc}}{zFP_{fuel}V_{lpm(fuel)}\chi_{H_2}}\big)\chi_{H_2}P_{fuel} + \\
&\quad + \big(1 - \frac{60000RTNi_{fc}}{2zFP_{air}V_{lpm(air)}\chi_{O_2}}\big)\chi_{O_2}P_{air}\Big)\Delta ve^{-\frac{\Delta G}{RT}} \\
U_{fc} &= -E_{pre} + K_c\Bigg[1.229 + (T-298)\frac{-44.43}{zF} + \\
&\quad + \frac{RT}{zF}\ln\left(\frac{Num^{fuel}(i_{fc})Num^{air}(i_{fc})}{\big(\chi_w + 2\chi_{O_2}\frac{60000RTNi_{fc}}{2zFP_{air}V_{lpm(air)}\chi_{O_2}}\big)P_{air}}\right)\Bigg] - R_i i_{fc} \\
Num^{fuel}(i_{fc}) &= \Big(1 - \frac{60000RTNi_{fc}}{zFP_{fuel}V_{lpm(fuel)}\chi_{H_2}}\Big)\chi_{H_2}P_{fuel} \\
Num^{air}(i_{fc}) &= \left(\Big(1 - \frac{60000RTNi_{fc}}{2zFP_{air}V_{lpm(air)}\chi_{O_2}}\Big)\chi_{O_2}P_{air}\right)^{1/2}
\end{aligned} \tag{4.18, 4.19}$$

Regarding the converter, it is physically supposed to provide a constant output voltage by means of fast-switching. While modelling this behaviour is quite simple, simulations tend to take much longer due to such nature. For this reason, in the end,

such a converter can be simplified to an energy balance (equation (4.20)), such that the power introduced is the same as the extracted, except for a small fraction, because of internal losses:

$$U_{out}I_{out} = \mu_{conv}U_{in}I_{in} \tag{4.20}$$

For this thesis, the output voltage is the grid's one, which is a constant value. Additionally, the input variables such as the intensity given by the controller and the voltage fixed by the intensity are known. This allows the current output intensity calculation. The created converter model can be seen in Figure 4.6.

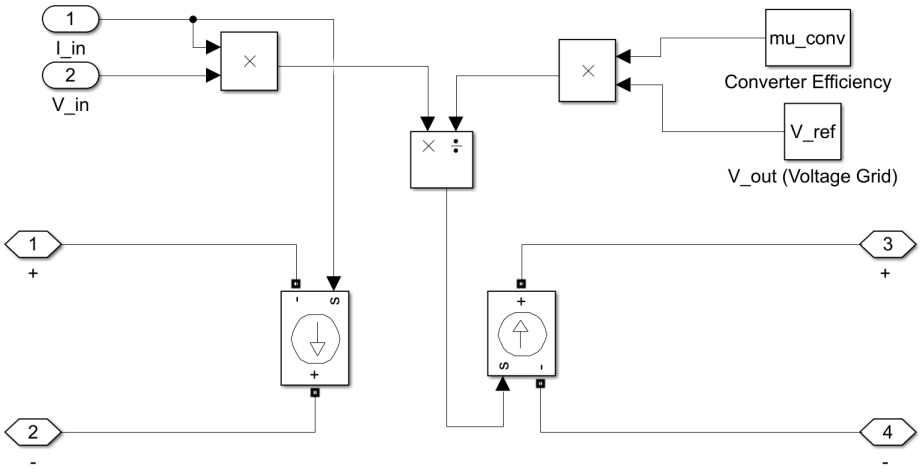

Figure 4.6: Matlab/Simulink converter model

Lastly, the controller will set the cell's intensity to a given value, but this has to be converted to hydrogen flow. Using equation (4.21) calculates the hydrogen needed in mol/s, but the Matlab/Simulink model's input is the amount of fuel in l/min.

$$\dot{n}_{H_2} = \frac{6000N_cIRT}{2Fn_{H_2,comp}n_{H_2,used}P_{fuel}}, \tag{4.21}$$

where T is the fuel cell's temperature in K, P_{fuel} the pressure of the hydrogen in Pa, $R = 8.314$ J/(mol K) the ideal gas constant, $n_{H_2,comp}$ is the number of hydrogen moles in the fuel's composition, $n_{H_2,used}$ is the number of hydrogen moles used for the reaction and N_c is the number of fuel cells.

4.1.2.2 PEM Electrolyser

A simple Matlab/Simulink model using Simscape electrical Toolbox to build electrical circuits is completed with a certain feedback dynamics. The model is the following one:

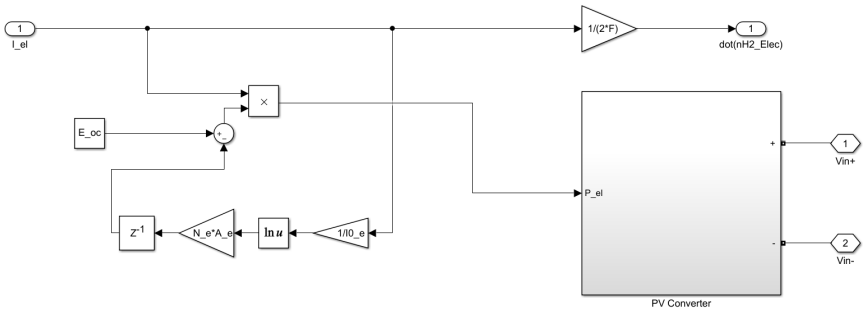

Figure 4.7: PEM electrolyser Matlab/Simulink model

The equivalent equations to this model are the following ones:

$$U_{El,pre} = N_e A_e \ln\left(\frac{I_{El}}{I_{El,0}}\right) \tag{4.22}$$

$$\dot{n}^A_{H_2} = \frac{I_{El}}{2F}, \tag{4.23}$$

where I_{El} is the electrolyser's current in A, $I_{El,0}$ is the electrolyser's open-circuit current in A, N_e is the number of layers in the electrolyser, A_e is the electrolyser's active area in m^2. As seen in Figure 4.7, artificial dynamics for simulation purposes (including time constant τ) is substituted by a time delay). Resulting voltage $U_{El,pre}$ can be substracted to the open circuit voltage E_{oc} to get the value of U_{El} (equation (4.24)). The other output equation is obtained from equation (4.23) and summarised as an state equation in equation (4.25):

$$U_{El} = E_{oc} - N_e A_e \ln\left(\frac{I_{El}}{I_{El,0}}\right) \tag{4.24}$$

$$\dot{n}^A_{H_2}(t) = \frac{1}{2F} I_{El}(t) \tag{4.25}$$

4.1.2.3 Photovoltaic cell

The Matlab/Simulink model for 'PV Array' has been used. This block has two inputs:

- Solar irradiance $[W/m^2]$
- PV cell temperature [℃]

The equivalent electrical circuit of the PV cell is the one shown in Figure 4.8 and its associated equation (4.26):

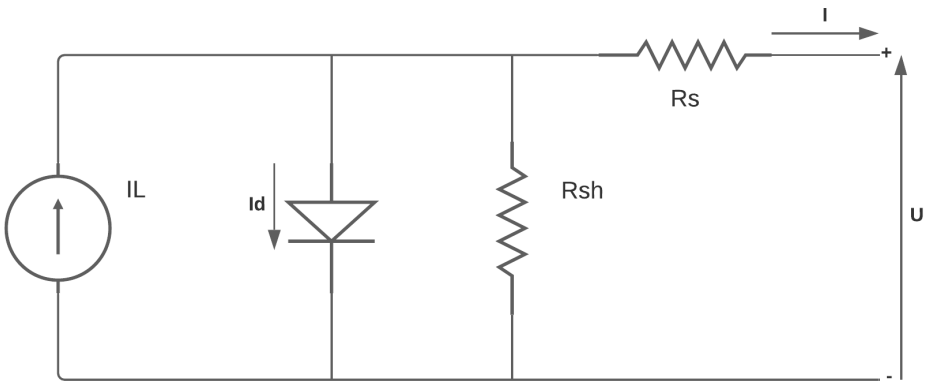

Figure 4.8: Matlab/Simulink PV cell equivalent circuit

$$U = R_{sh}(I_L - I_d - I) - R_s I, \tag{4.26}$$

where U_{PV} is the solar panel's voltage in V, $R_{sh}$is the solar panel's shunt resistance in Ω, R_s is the solar panel's resistance in Ω, I_L is the solar panel's internal current in A, I_d is the solar panel's internal diode's current in A and I is the solar panel's output current in A.

4.1.2.4 Hydrogen storage tank

The hydrogen storage tank is simplified to an integration of the input hydrogen molar flow $\dot{n}^A_{H_2}$ to produce the amount of hydrogen moles stored $n^A_{H_2}$. The equation is the following one:

$$n^A_{H_2} = \int \dot{n}^A_{H_2} dt \tag{4.27}$$

4.1.2.5 Electrical battery

The Matlab/Simulink model for the electrical battery is the one in the Simscape toolbox and it can be seen in Figure 4.9. This model has 4 parameters: nominal voltage, rated capacity, initial state of charge and response time. Battery discharge, temperature and ageing effects can also be modelled. Its structure has the one seen in diagram from Figure 4.10.

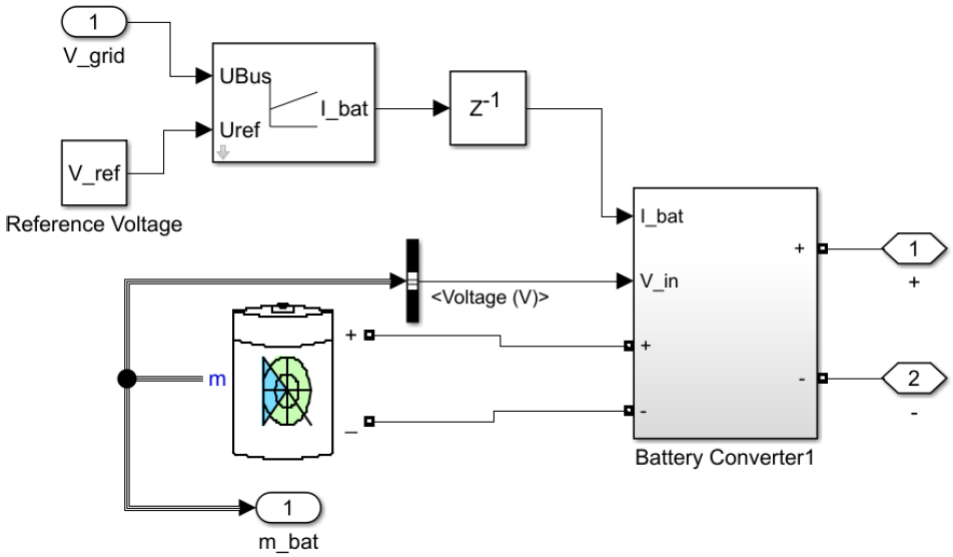

Figure 4.9: Matlab/Simulink battery model

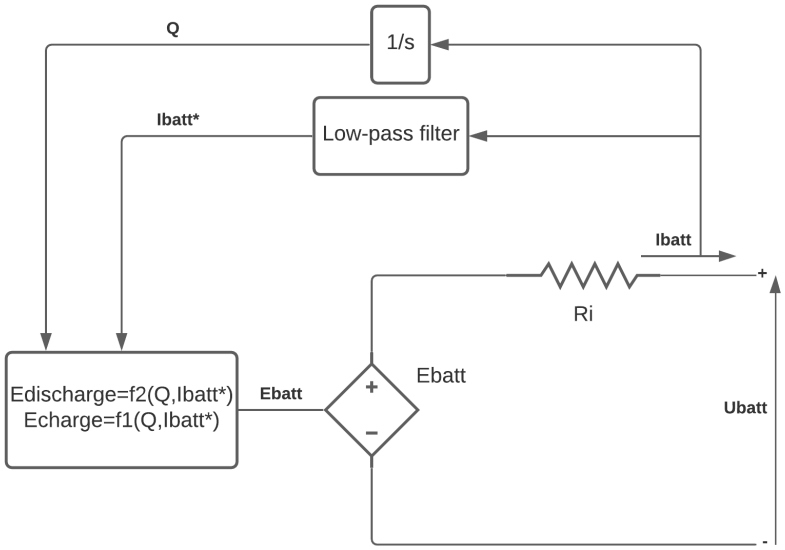

Figure 4.10: Matlab/Simulink battery model block diagram

Apart from this, a converter for the battery is needed to connect it to the grid to boost the voltage to the reference one. Contrarily to the cell, batteries can be charged and discharged, implying that the converter must be bidirectional. This converter (Figure 4.11) is modelled as a change in the efficiency of the converter, which depends on the sign of the battery's intensity. Therefore, this is set to a lower value to the one for positive battery currents and for the opposite case, the inverse of the efficiency was used, as the input intensity turns out the be the one of the grid.

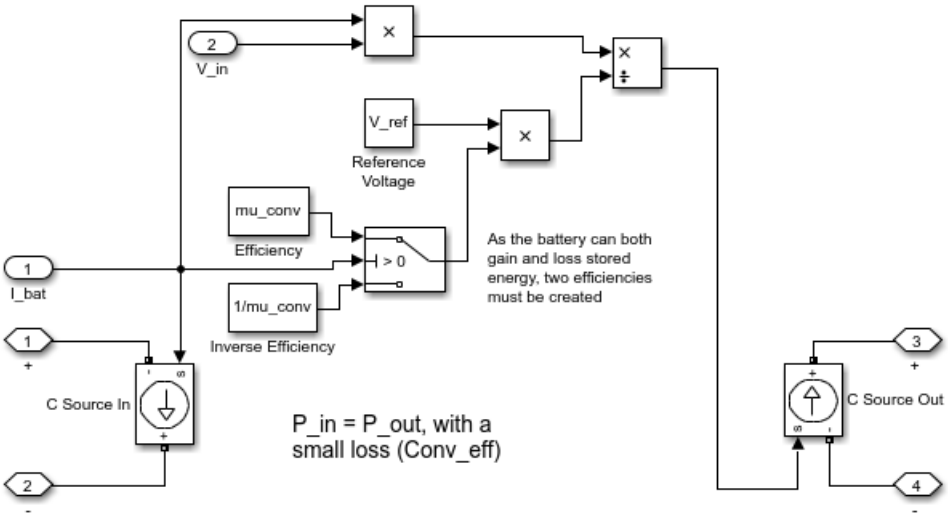

Figure 4.11: Matlab/Simulink battery converter model

Looking at equations from Figure 4.11, the state-space representation for the lithium-ion battery model can be found. First of all, variables $Q_{max} = Q$, $Q = it$, $U_{batt} = V_{batt}$, $I_{batt} = i$ and $I^*_{batt} = i^*$ are renamed and functions $E_{discharge} = f_1(Q, I^*_{batt})$ and $E_{charge} = f_2(Q, I^*_{batt})$ corresponding to the value of E_{batt} for the discharging ($I^*_{batt} > 0$) and charging ($I^*_{batt} < 0$) can be defined as follows:

$$E_{discharge} = f_1(Q, I^*_{batt}) = E_0 - K\frac{Q_{max}}{Q_{max} - Q}I^*_{batt} - K\frac{Q_{max}}{Q_{max} - Q}Q + Ae^{-BQ} \quad (4.28)$$

$$E_{charge} = f_2(Q, I^*_{batt}) = E_0 - K\frac{Q_{max}}{Q + 0.1Q_{max}}I^*_{batt} - K\frac{Q_{max}}{Q_{max} - Q}Q + Ae^{-BQ}, \quad (4.29)$$

where E_0 is the open circuit voltage in V, K is the polarisation constant in V/Ah, Q_{max} is the maximum battery capacity in Ah, Q is the extracted capacity in Ah, I^*_{batt} is the low frequency current dynamics in A, I_{batt} is the battery current in A, A is the exponential voltage in A and B is the exponential capacity in A/h. Additionally, U_{batt} is the battery voltage in V, E_{batt} is the nonlinear internal voltage of the battery in V and R_i is the battery internal resistance in Ω. To define the state-space of the battery model the following variables are considered:

- Q and I^*_{batt} are state variables.
- I_{batt} is the input variable.

- U_{batt} is the output variable.

The first state-space equation is derived from equation (4.30) as follows:

$$\dot{Q} = I_{batt} \tag{4.30}$$

The second state-space equation is derived from defining a first order low-pass filter with a time constant τ in the Laplace domain (equation (4.31)) and transforming it to the time domain as seen in equation (4.32):

$$G_{1of}(s) = \frac{1}{\tau s + 1} \tag{4.31}$$

$$\dot{I}^*_{batt} = -\frac{1}{\tau} I^*_{batt} + \frac{1}{\tau} I_{batt} \tag{4.32}$$

I_{batt} variable in equations (4.30) and (4.32) is calculated with the system's output equation:

$$I_{batt} = -\frac{1}{R_i} E_{batt} + \frac{1}{R_i} U_{batt} \tag{4.33}$$

Finally, the nonlinear state-space representation of the discharging model is formed by state equations (4.30) and (4.32). The result is the following one:

$$\begin{bmatrix} \dot{Q} \\ \dot{I}^*_{batt} \end{bmatrix} = \begin{bmatrix} 0 & 0 \\ 0 & -\frac{1}{\tau} \end{bmatrix} \begin{bmatrix} Q \\ I^*_{batt} \end{bmatrix} + \begin{bmatrix} 1 \\ \frac{1}{\tau} \end{bmatrix} I_{batt} \tag{4.34}$$

$$U_{batt} = \left(E_0 - K\frac{Q_{max}}{Q_{max} - Q} I^*_{batt} - K\frac{Q_{max}}{Q_{max} - Q} Q + Ae^{-BQ}\right) + R_i I_{batt} \tag{4.35}$$

$$SOC = 1 - \frac{1}{Q_{max}} Q, \tag{4.36}$$

where SOC is the state of charge of the battery, equal to 0 when it is fully discharged and 1 when it is fully charged. For the case of the charging model, equations (4.34) and (4.36) are the same but equation (4.35) is replaced by the following equation (4.37):

$$U_{batt} = E_0 - K\frac{Q_{max}}{Q + 0.1Q_{max}} I^*_{batt} - K\frac{Q_{max}}{Q_{max} - Q} Q + Ae^{-BQ} + R_i I_{batt} \tag{4.37}$$

Additionally, a PI control is designed to control the grid voltage. The scheme on Figure 4.13 compares this voltage and the reference one to act on battery's current to maintain it at that value. Additionally, a saturation block has been placed to avoid large currents going through the battery. Calculation of the PI parameters is done later

in this thesis and a delay has been added to the system to avoid a loop that prevented the simulation from starting.

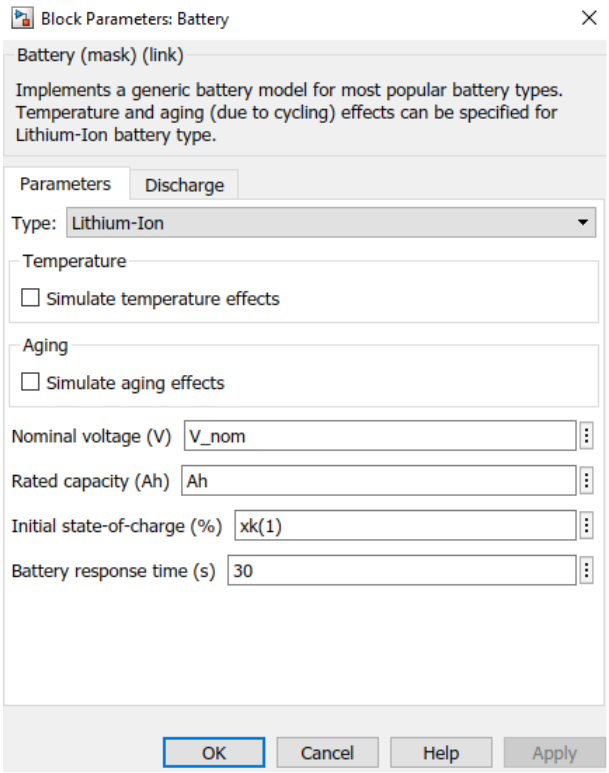

Figure 4.12: Matlab/Simulink battery model parameters

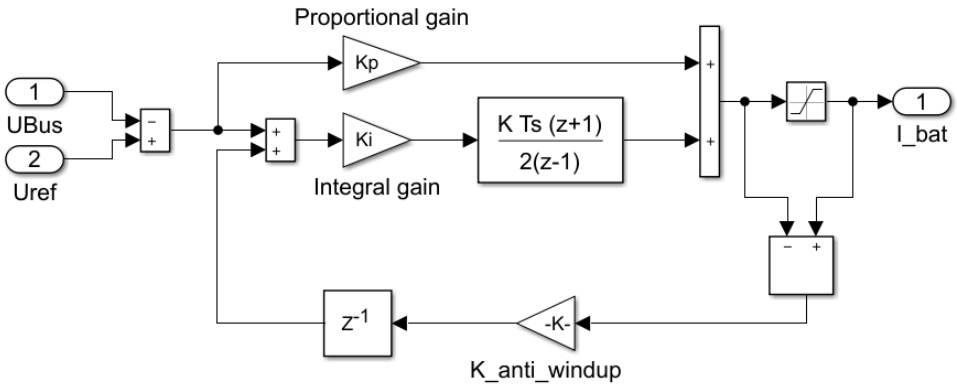

Figure 4.13: Matlab/Simulink PI controller model

4.1.2.6 Heat exchanger and water tank

Regarding the thermal part of the system, a water tank is used as a simple way to use the heat produced by the fuel cell and keep hot water for later uses. The heat exchanger consists on an oil tank surrounding the fuel cell and it can be modelled as a simple thermal model before the water tank. This is the following one. Both water and oil tank masses are considered constant as they are filled at the same rate they have mass losses. This can be seen in Figure 4.14.

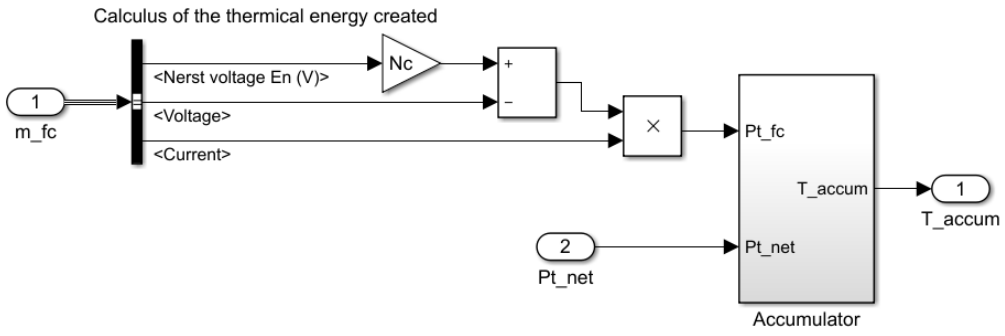

Figure 4.14: Thermal energy calculation and water tank, i.e. accumulator

The oil accumulator system included in Figure 4.14 follows equation (4.38) in the Laplace domain:

$$sT_{acc}^{oil} = \frac{1}{m_{tank}^{oil} c_p^{oil}} P_{t,fc} \mu_{exch} - \frac{K_{exch}}{m_{tank}^{oil} c_p^{oil}} (T_{acc}^{oil} - T_{acc}^{H_2O}), \tag{4.38}$$

where $P_{t,fc}$ is the fuel cell thermal power in W, T_{acc}^{oil} is the oil accumulator temperature in K, $T_{acc}^{H_2O}$ is the water accumulator temperature in K, K_{exch} is the oil-tank exchange losses constant in W/K, m_{tank}^{oil} is the tank mass in kg, c_p^{oil} is oil's specific heat in J/(kg K) and μ_{exch} is the exchanger efficiency. As seen in Figure 4.14, $P_{t,fc}$ is linked to the cell current according to the following equation:

$$P_{t,fc} = (N_c E_n - U) I, \tag{4.39}$$

where U is the grid voltage in V. Transforming equation (4.38) to time domain and organising it as a state-space representation as seen in equation (4.40):

$$\dot{T}_{acc}^{oil} = -\frac{K_{exch}}{m_{tank}^{oil} c_p^{oil}} \begin{bmatrix} 1 & -1 \end{bmatrix} \begin{bmatrix} T_{acc}^{oil} \\ T_{acc}^{H_2O} \end{bmatrix} + \frac{\mu_{exch}}{m_{tank}^{oil} c_p^{oil}} P_{t,fc} \tag{4.40}$$

Similarly, the other accumulator, the water accumulator system, follows the thermal balance seen in equation (4.42):

$$sT_{acc}^{H_2O} = -\frac{K_{env}}{m_{tank}^{H_2O}c_p^{H_2O}}(T_{acc}^{H_2O} - T_{env}) + \frac{K_{exch}}{m_{tank}^{oil}c_p^{oil}}(T_{acc}^{oil} - T_{acc}^{H_2O}) - \frac{Q_{HW}}{m_{tank}^{H_2O}c_p^{H_2O}}, \quad (4.41)$$

where Q_{HW} is the power corresponding to hot water extracted from the accumulator in W, $c_p^{H_2O}$ is water's specific heat in J/(kg K), K_{env} is the environment losses constant in W/K and T_{env} is the environment temperature in K. This can be transformed to the state-space representation (time domain) as follows:

$$\dot{T}_{acc}^{H_2O} = \begin{bmatrix} \frac{K_{exch}}{m_{tank}^{oil}c_p^{oil}} & \frac{-K_{env}}{m_{tank}^{H_2O}c_p^{H_2O}} - \frac{K_{exch}}{m_{tank}^{oil}c_p^{oil}} \end{bmatrix} \begin{bmatrix} T_{acc}^{oil} \\ T_{acc}^{H_2O} \end{bmatrix} - \frac{Q_{HW}}{m_{tank}^{H_2O}c_p^{H_2O}} + \frac{K_{env}T_{env}}{m_{tank}^{H_2O}c_p^{H_2O}} \quad (4.42)$$

4.2 Consumption analysis

The whole CHP system is designed to manage thermal and electrical demands of a particular house studied. For this reason, a simple thermal model for the house, data corresponding to climate conditions around it and consumption data assigned to it need to be defined.

4.2.1 Thermal model of the house

The effect of heat exchange between the environment, the house space to be heated and the heat coming from the CHP system defined previously needs to be modelled. When doing so, a simple model based on thermal resistances is detailed. In the case of the house, the heat exchange between the house (temperature T_{house}) and the environment (temperature T_{out}) is defined according to the following equations:

$$\frac{dQ_{loss}}{dt} = \frac{T_{house} - T_{out}}{R_{eq}^{house}} \quad (4.43)$$

$$\frac{dT_{house}}{dt} = \frac{1}{M_{air}c_p^{air}}\left(\frac{dQ_{heater}}{dt} - \frac{dQ_{loss}}{dt}\right) \quad (4.44)$$

Parameters in equations (4.43) and (4.44) are the following:

- M_{air} is the mass of air inside the house in kg.
- R_{eq}^{house} is the equivalent thermal resistance of the house in K/W.

- c_p^{air} is the air's heat capacity at constant pressure in J/(kg K).
- Q_{loss} is the thermal energy exchange between the house and the environment in J.
- Q_{heater} is heater's thermal energy in J.

Similarly, the CHP heating system (temperature T_{heater}) has the following thermal relationship with the house inner space:

$$\frac{dQ_{heater}}{dt} = (T_{heater} - T_{house})\dot{M}c_p^{air}, \tag{4.45}$$

where $\dot{M}$ is the air mass flow rate through the heater. If expressions in equations (4.43) and (4.45) are substituted in equation (4.44), the following expression is obtained:

$$\begin{aligned}\frac{dT_{house}}{dt} &= \frac{1}{M_{air}c_p^{air}}\Big((T_{heater} - T_{house})\dot{M}c_p^{air} - \frac{T_{house} - T_{out}}{R_{eq}^{house}}\Big) \\ &= \frac{-1}{M_{air}}\Big(\dot{M} + \frac{1}{c_p^{air}R_{eq}}\Big)T_{house} + \frac{\dot{M}}{M_{air}}T_{heater} + \frac{1}{M_{air}c_p^{air}R_{eq}}T_{out}\end{aligned} \tag{4.46}$$

Equation (4.46) has two inputs (T_{heater} and T_{out}) and T_{house} as output. Changing time dominion equation to the Laplace dominion, the following expression is obtained:

$$\begin{aligned}sT_{house}(s) &= \frac{-1}{M_{air}}\Big(\dot{M} + \frac{1}{c_p^{air}R_{eq}}\Big)T_{house}(s) + \frac{\dot{M}}{M_{air}}T_{heater}(s) + \frac{1}{M_{air}c_p^{air}R_{eq}}T_{out}(s) \\ \Big(s + \frac{1}{M_{air}}\Big(\dot{M} + \frac{1}{c_p^{air}R_{eq}}\Big)\Big)T_{house}(s) &= \frac{\dot{M}}{M_{air}}T_{heater}(s) + \frac{1}{M_{air}c_p^{air}R_{eq}}T_{out}(s) \\ T_{house}(s) &= \frac{\frac{\dot{M}}{M_{air}}}{s + \frac{1}{M_{air}}(\dot{M} + \frac{1}{c_p^{air}R_{eq}})}T_{heater}(s) + \frac{\frac{1}{M_{air}c_p^{air}R_{eq}}}{s + \frac{1}{M_{air}}(\dot{M} + \frac{1}{c_p^{air}R_{eq}})}T_{out}(s)\end{aligned} \tag{4.47}$$

Evaluating to 0 each of the inputs $T_{heater}(s)$ and $T_{out}(s)$ on equation (4.47), two transfer functions $G_{HH}(s)$ and $G_{OH}(s)$ are obtained as follows:

$$G_{HH}(s) = \frac{T_{house}(s)}{T_{heater}(s)} = \frac{\frac{\dot{M}}{M_{air}}}{s + \frac{1}{M_{air}}(\dot{M} + \frac{1}{c_p^{air}R_{eq}})} = \frac{\frac{\dot{M}}{\dot{M} + \frac{1}{c_p^{air}R_{eq}}}}{\frac{M_{air}}{\dot{M} + \frac{1}{c_p^{air}R_{eq}}}s + 1} \tag{4.48}$$

$$G_{OH}(s) = \frac{T_{house}(s)}{T_{out}(s)} = \frac{\frac{1}{M_{air}c_p^{air}R_{eq}}}{s + \frac{1}{M_{air}}(\dot{M} + \frac{1}{c_p^{air}R_{eq}})} = \frac{\frac{1}{1 + \dot{M}c_p^{air}R_{eq}}}{\frac{M_{air}}{\dot{M} + \frac{1}{c_p^{air}R_{eq}}}s + 1} \tag{4.49}$$

Knowing that a typical first order system has the structure $G(s) = \frac{K}{\tau s+1}$, it can be seen that both transfer functions $G_{HH}(s)$ and $G_{OH}(s)$ have the same time constant $\tau = \frac{M_{air}}{\dot{M}+\frac{1}{c_p^{air}R_{eq}}}$. This time constant τ can be proved to be the inverse of the coefficient of equation (4.46) with a negative sign, as stated by theory. This parameter can be used to obtain an approximation of the house's equivalent thermal resistance R_{eq}, once M_{air}, $\dot{M}$ and c_p^{air} are defined.

4.2.2 House localisation and climate data

The house selected is located in a town with quite cold weather conditions but not too extreme. Its location is the following one:

- *Town*: El Pont de Suert (Alta Ribagorça, Catalonia, Spain) (see map in Figure 4.15
- *Height*: 823 m
- *Population*: 2216 (year 2018), according to the Instituto Nacional de Estadística (the Spanish statistics institute)

Figure 4.15: Location of the house, map provided by Institut Cartogràfic i Geològic de Catalunya (the Catalan government's cartographic and geological institute

To obtain data about the weather conditions around the house, historical data of the Servei Meteorològic de Catalunya (Catalonia's government climate agency) has been searched. A typical winter day (15/01/2020) and spring day (15/04/2020) have been selected for the study, whose measured temperatures can be seen in Figures 4.16 and 4.17. For the current study, temperature values and solar irradiance are needed. These values are provided by the local weather station every 30 minutes. In the following table (Table 4.1), values for the 15/01/2020 are listed:

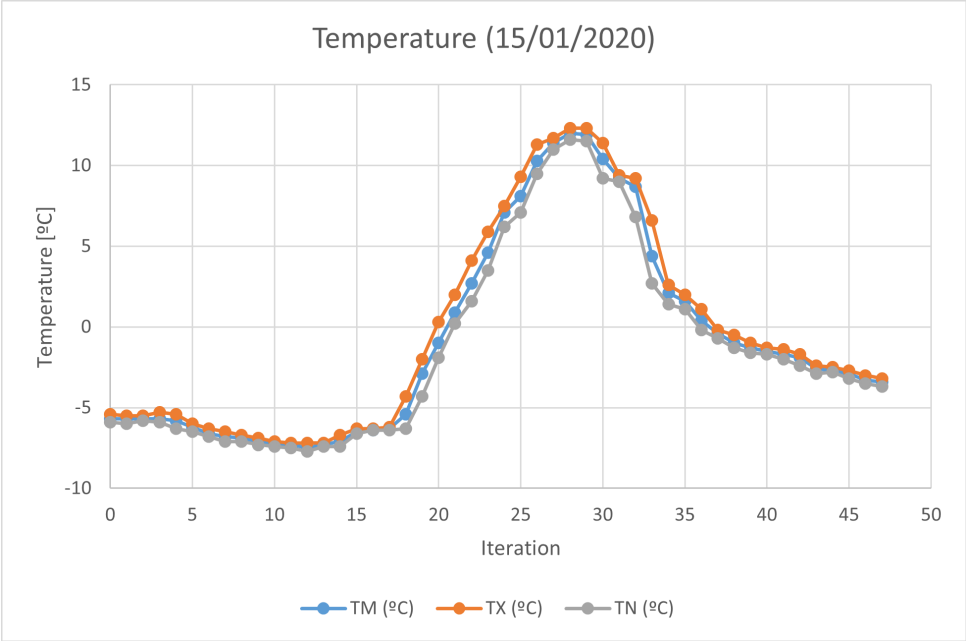

Figure 4.16: Maximum, minimum and average temperatures on day 15/01/2020 measured every 30 minutes (1 iteration every 30 minutes)

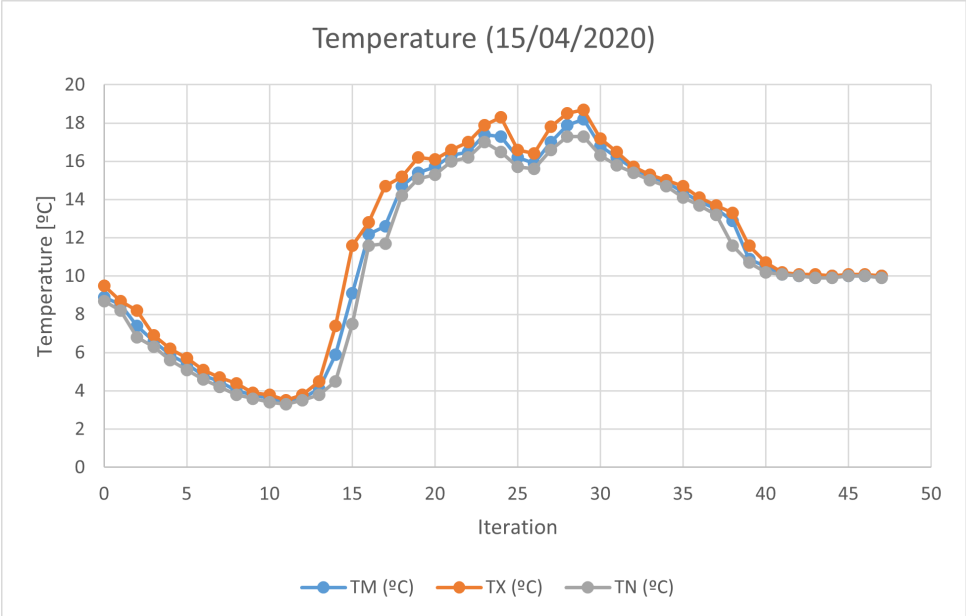

Figure 4.17: Maximum, minimum and average temperatures on day 15/04/2020 measured every 30 minutes (1 iteration every 30 minutes)

Table 4.1: Weather conditions on day 15/01/2020

Period [Start - End]	Maximum temperature [°C]	Average temperature [°C]	Minimum temperature [°C]	Solar irradiance [W/m^2]
00:00 - 00:30	-5.7	-5.4	-5.9	0
00:30 - 01:00	-5.7	-5.5	-6.0	0
01:00 - 01:30	-5.7	-5.5	-5.8	0
01:30 - 02:00	-5.7	-5.3	-5.9	0
02:00 - 02:30	-5.8	-5.4	-6.3	0
02:30 - 03:00	-6.2	-6.0	-6.5	0
03:00 - 03:30	-6.6	-6.3	-6.8	0
03:30 - 04:00	-6.8	-6.5	-7.1	0
04:00 - 04:30	-6.9	-6.7	-7.1	0
04:30 - 05:00	-7.1	-6.9	-7.3	0
05:00 - 05:30	-7.3	-7.1	-7.4	0
05:30 - 06:00	-7.3	-7.2	-7.5	0
06:00 - 06:30	-7.5	-7.2	-7.7	0
06:30 - 07:00	-7.3	-7.2	-7.4	0
07:00 - 07:30	-7.1	-6.7	-7.4	2
07:30 - 08:00	-6.5	-6.3	-6.6	9
08:00 - 08:30	-6.4	-6.3	-6.4	22
08:30 - 09:00	-6.3	-6.2	-6.4	30
09:00 - 09:30	-5.4	-4.3	-6.3	187
09:30 - 10:00	-2.9	-2.0	-4.3	345
10:00 - 10:30	-1.0	0.3	-1.9	333
10:30 - 11:00	0.9	2.0	0.2	414
11:00 - 11:30	2.7	4.1	1.6	473
11:30 - 12:00	4.6	5.9	3.5	433
12:00 - 12:30	7.1	7.5	6.2	449
12:30 - 13:00	8.1	9.3	7.1	424
13:00 - 13:30	10.3	11.3	9.5	427
13:30 - 14:00	11.4	11.7	11.0	393
14:00 - 14:30	12.0	12.3	11.6	343
14:30 - 15:00	11.9	12.3	11.5	278
15:00 - 15:30	10.4	11.4	9.2	99
15:30 - 16:00	9.2	9.4	9.0	24
16:00 - 16:30	8.7	9.2	6.8	14
16:30 - 17:00	4.4	6.6	2.7	2

Period [Start - End]	Maximum temperature [℃]	Average temperature [℃]	Minimum temperature [℃]	Solar irradiance [W/m^2]
17:00 - 17:30	2.1	2.6	1.4	0
17:30 - 18:00	1.6	2.0	1.1	0
18:00 - 18:30	0.4	1.1	-0.2	0
18:30 - 19:00	-0.4	-0.2	-0.7	0
19:00 - 19:30	-1.0	-0.5	-1.3	0
19:30 - 20:00	-1.3	-1.0	-1.6	0
20:00 - 20:30	-1.5	-1.3	-1.7	0
20:30 - 21:00	-1.7	-1.4	-2.0	0
21:00 - 21:30	-1.9	-1.7	-2.4	0
21:30 - 22:00	-2.6	-2.4	-2.9	0
22:00 - 22:30	-2.7	-2.5	-2.8	0
22:30 - 23:00	-2.9	-2.7	-3.2	0
23:00 - 23:30	-3.3	-3.0	-3.5	0
23:30 - 00:00	-3.4	-3.2	-3.7	0

The same is done for data corresponding to the 15/04/2020 as follows (Table 4.2):

Table 4.2: Weather conditions on day 15/01/2020

Period [Start - End]	Maximum temperature [℃]	Average temperature [℃]	Minimum temperature [℃]	Solar irradiance [W/m^2]
00:00 - 00:30	8.9	9.5	8.7	0
00:30 - 01:00	8.5	8.7	8.2	0
01:00 - 01:30	7.4	8.2	6.8	0
01:30 - 02:00	6.6	6.9	6.3	0
02:00 - 02:30	5.9	6.2	5.6	0
02:30 - 03:00	5.4	5.7	5.1	0
03:00 - 03:30	4.8	5.1	4.6	0
03:30 - 04:00	4.5	4.7	4.2	0
04:00 - 04:30	4.0	4.4	3.8	0
04:30 - 05:00	3.8	3.9	3.6	0
05:00 - 05:30	3.6	3.8	3.4	2
05:30 - 06:00	3.4	3.5	3.3	15
06:00 - 06:30	3.6	3.8	3.5	35
06:30 - 07:00	4.1	4.5	3.8	46
07:00 - 07:30	5.9	7.4	4.5	236
07:30 - 08:00	9.1	11.6	7.5	422

Period [Start - End]	Maximum temperature [°C]	Average temperature [°C]	Minimum temperature [°C]	Solar irradiance [W/m^2]
08:00 - 08:30	12.2	12.8	11.6	452
08:30 - 09:00	12.6	14.7	11.7	465
09:00 - 09:30	14.7	15.2	14.2	439
09:30 - 10:00	15.4	16.2	15.1	349
10:00 - 10:30	15.7	16.1	15.3	289
10:30 - 11:00	16.3	16.6	16.0	361
11:00 - 11:30	16.5	17.0	16.2	448
11:30 - 12:00	17.4	17.9	17.0	834
12:00 - 12:30	17.3	18.3	16.5	684
12:30 - 13:00	16.2	16.6	15.7	300
13:00 - 13:30	15.9	16.4	15.6	327
13:30 - 14:00	17.0	17.8	16.6	691
14:00 - 14:30	17.9	18.5	17.3	759
14:30 - 15:00	18.2	18.7	17.3	690
15:00 - 15:30	16.8	17.2	16.3	177
15:30 - 16:00	16.2	16.5	15.8	133
16:00 - 16:30	15.6	15.7	15.4	56
16:30 - 17:00	15.2	15.3	15.0	22
17:00 - 17:30	14.9	15.0	14.7	20
17:30 - 18:00	14.4	14.7	14.1	6
18:00 - 18:30	13.9	14.1	13.7	6
18:30 - 19:00	13.5	13.7	13.2	0
19:00 - 19:30	12.9	13.3	11.6	0
19:30 - 20:00	10.9	11.6	10.7	0
20:00 - 20:30	10.5	10.7	10.2	0
20:30 - 21:00	10.1	10.2	10.1	0
21:00 - 21:30	10.0	10.1	10.0	0
21:30 - 22:00	10.0	10.1	9.9	0
22:00 - 22:30	10.0	10.0	9.9	0
22:30 - 23:00	10.0	10.1	10.0	0
23:00 - 23:30	10.0	10.1	10.0	0
23:30 - 00:00	10.0	10.0	9.9	0

Based on this data, temperature profiles every 15 minutes are obtained interpolating temperatures. The same is done for solar irradiance.

4.2.3 Thermal and electrical demands

Thermal and electrical demands are defined according to the month studied, based on estimated electrical and thermal needs by a family. For a typical day of January, these can be in Figures 4.18 and 4.19. Iteration 1 corresponds to midnight, and a whole day separated on 97 iterations is depicted (15 minutes between each one):

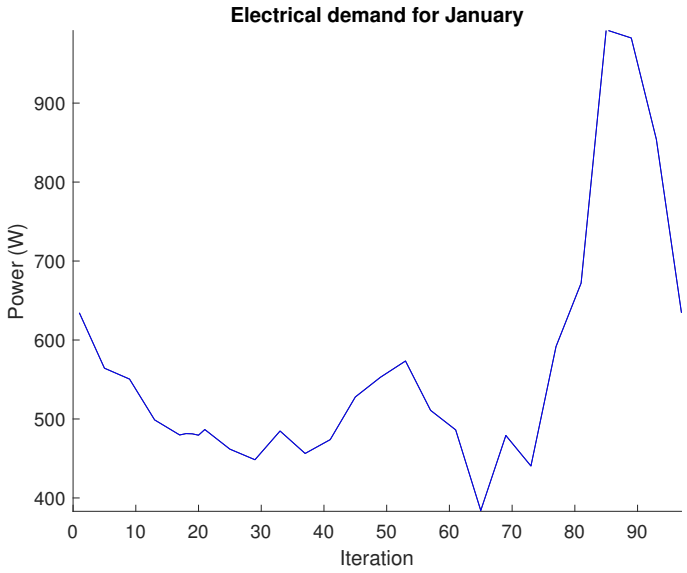

Figure 4.18: Electrical demand on a typical day of January

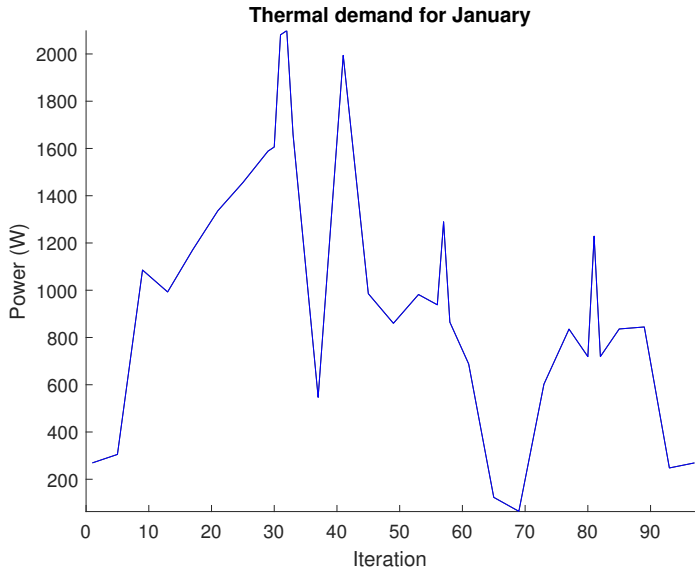

Figure 4.19: Thermal demand on a typical day of January

Similarly, for a typical day of April, demands are seen in Figures 4.20 and 4.21:

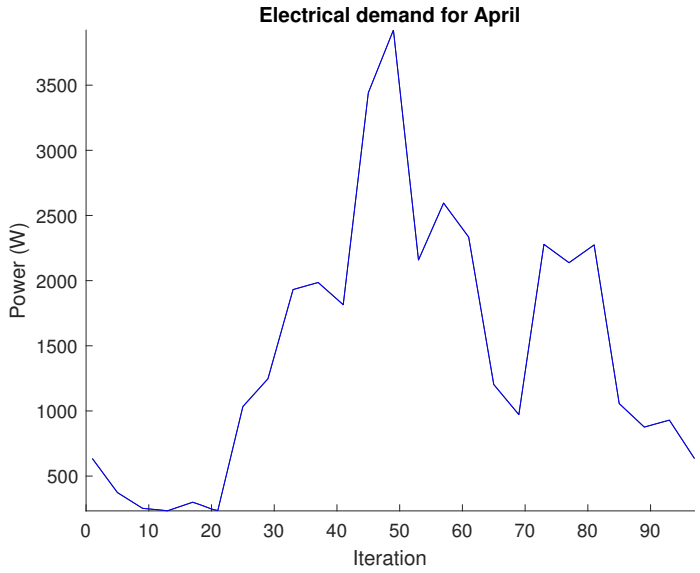

Figure 4.20: Electrical demand on a typical day of April

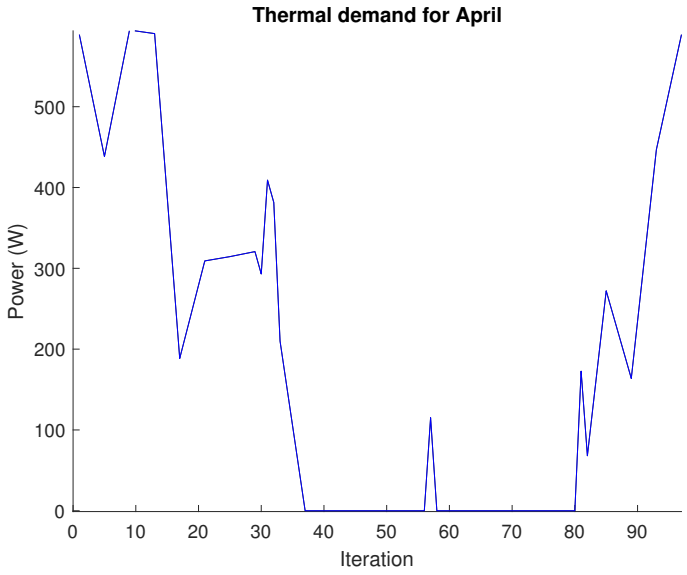

Figure 4.21: Thermal demand on a typical day of April

These demands will be used in following chapters to test control algorithms proposed along a typical day of January and April. Demand variations along the day will also be imposed, to see if the system is able to follow the real demand even when this is not fully known when the day starts. However, some assumptions regarding consumption tendencies for January and April will be assumed, as real demands for certain months follow certain trends from one year to the other.

4.2.4 Elements dimensioning

Once the system has been defined, it must fit the application. Considering the amount of power demanded to fulfill electrical and heat requirements, the appropriate size of the system elements must be chosen. The study carried on by [48] deals with a 5 kWe HT-PEMFC stack (72 cells) for a CHP residential application, and it can work as a starting point to start our process of design. The same goes for the electrical battery, water accumulator and solar panel and electrolyser, as after the first results its values need to be adjusted so that they have dimensions big enough to fulfil system operation but small enough to reduce economical cost, as overdimensioned devices imply excessive costs. Control strategies play a crucial role when these dimensions follow this

trade-off between economical cost and energy efficiency. Initial dimensions for the first simulations are the following ones:

- Battery capacity: 160 Ah
- Water accumulator mass: 200 kg
- Oil accumulator mass: 100 kg

The influence of changing these values will be explored in simulation to check its influence and final value.

Chapter 5

Control system structure

Alone am I driven each day before daybreak

To give my cares utterance.

From *The Wanderer*

Once the system has been modelled for simulation, a control approach to obtain the results desired is needed. In this chapter, the global control problem and its mathematical formulation are presented.

5.1 Detailed models' description and integration

Once mathematical models for all parts of the system have been defined, they can be integrated in a single state-space representation that can be later controlled. To do so, the following hypotheses are assumed:

- Variable E_{pre} and its equation (4.18) are not included, as it is the result of applying a simple dynamic for simulation requirements. Suppressing this artificial dynamics setting $\dot{E}_{pre} = 0$, equation (4.18) ends up being:

$$E_{pre} = NA \ln\left(\frac{i_{fc}}{i_0}\right) \tag{5.1}$$

- Variable I_{El} is obtained reformulating equation(4.24) the following way:

$$I_{El} = I_{El,0} \exp\left(\frac{E_{oc} - U_{El}(t)}{N_e A_e}\right) \tag{5.2}$$

- Variable I^*_{batt} and its equation in the second term of equation (4.34) are not included, is the result of applying a simple low-pass filter for simulation requirements. As done above, $\dot{I}^*_{batt} = 0$ is imposed on equation (4.32) giving the following result:

$$I^*_{batt} = I_{batt} \tag{5.3}$$

Additionally, a capacitor with capacity C is added to the system and has the following state-space equations:

$$\dot{Q}_c = I_c \tag{5.4}$$

$$U_c = \frac{Q_c}{C} \tag{5.5}$$

For the both cases of battery charging and discharging, an initial simplified state equation can be defined as seen in equation (5.6):

$$\begin{aligned}
\begin{bmatrix} \dot{Q}_{batt} \\ \dot{Q}_c \\ \dot{T}^{oil}_{acc} \\ \dot{T}^{H_2O}_{acc} \end{bmatrix} &= \begin{bmatrix} 0 & 0 & 0 & 0 \\ 0 & 0 & 0 & 0 \\ 0 & 0 & \frac{-K_{exch}}{m^{oil}_{tank} c^{oil}_p} & \frac{K_{exch}}{m^{oil}_{tank} c^{oil}_p} \\ 0 & 0 & \frac{K_{exch}}{m^{oil}_{tank} c^{oil}_p} & \frac{-K_{env}}{m^{H_2O}_{tank} c^{H_2O}_p} - \frac{K_{exch}}{m^{oil}_{tank} c^{oil}_p} \end{bmatrix} \begin{bmatrix} Q_{batt} \\ Q_c \\ T^{oil}_{acc} \\ T^{H_2O}_{acc} \end{bmatrix} + \\
&+ \begin{bmatrix} 0 & 0 & 0 \\ 1 & 0 & 0 \\ 0 & \frac{\mu_{exch}}{m^{oil}_{tank} c^{oil}_p} & 0 \\ 0 & 0 & \frac{-1}{m^{H_2O}_{tank} c^{H_2O}_p} \end{bmatrix} \begin{bmatrix} I_{load} \\ P_{t,fc} \\ Q_{HW} \end{bmatrix} + \begin{bmatrix} 0 & 0 \\ -1 & 0 \\ 0 & 0 \\ 0 & \frac{K_{env}}{m^{H_2O}_{tank} c^{H_2O}_p} \end{bmatrix} \begin{bmatrix} I_{PV} \\ T_{env} \end{bmatrix} + \\
&+ \begin{bmatrix} I_{batt} \\ -I_{batt} + I_{fc} - I_{El} \\ 0 \\ 0 \end{bmatrix},
\end{aligned} \tag{5.6}$$

where variables are classified as follows:

- Q_{batt}, Q_c, T^{oil}_{acc} and $T^{H_2O}_{acc}$ are state variables.
- I_{load}, $P_{t,fc}$ and Q_{HW} are input variables.
- I_{PV} and T_{env} are disturbance variables.

The state-space equation (5.6) has the advantage of being linear but, as input variables $P_{t,fc}$ and Q_{HW} are difficult to impose in reality, new input variables must be

selected, at the cost of forcing nonlinearities to arise. Consequently, $P_{t,fc}$ is replaced using the expression of U_{fc} in equation (4.18). The resulting expression for $P_{t,fc}$ is calculated as follows:

$$\begin{aligned}
P_{t,fc} &= U_{fc} i_{fc} = \\
&= -NA \ln\left(\frac{i_{fc}}{i_0}\right) i_{fc} + K_c \left[1.229 + (T - 298)\frac{-44.43}{zF} + \right. \\
&\left. + \frac{RT}{zF} \ln\left(\frac{Num_{fuel}(i_{fc}) Num_{air}(i_{fc})}{(\chi_w + 2\chi_{O_2} \frac{60000RTNi_{fc}}{2zFP_{air}V_{lpm(air)}\chi_{O_2}}) P_{air}} \right) \right] i_{fc} - R_i i_{fc}^2 \\
Num^{fuel}(i_{fc}) &= \left(1 - \frac{60000RTNi_{fc}}{zFP_{fuel}V_{lpm(fuel)}\chi_{H_2}}\right) \chi_{H_2} P_{fuel} \\
Num^{air}(i_{fc}) &= \left(\left(1 - \frac{60000RTNi_{fc}}{2zFP_{air}V_{lpm(air)}\chi_{O_2}}\right) \chi_{O_2} P_{air} \right)^{1/2}
\end{aligned} \tag{5.7}$$

Considering that fuel cell, solar panel, electrolyser, battery and capacitor are connected in parallel, the following definition of the bus voltage can be defined, using equation (5.5), as follows:

$$U_{fc} = U_{PV} = U_{batt} = U_{El} = U_c = \frac{Q_c}{C} \tag{5.8}$$

At the same time, i_{fc} can be expressed in terms of the hydrogen molar flow needed for the fuel cell $\dot{n}_{H_2}$, measured in mol/s. The relation is the one mentioned in previous chapters, like in equation (4.25). On the other hand, Q_{HW} can be calculated in practical terms as a function of the amount of water consumed the following way:

$$Q_{HW} = \dot{m}_{HW} c_p^{H_2O} T_{acc}^{H_2O}, \tag{5.9}$$

where $\dot{m}_{HW}$ is the mass flow extracted from the water accumulator for consumption needs, measured in kg/s. If variables $P_{t,fc}$ and Q_{HW} are replaced by expressions in equations (5.7) and (5.9), voltages are replaced according to equation (5.8) and currents I_{fc}, I_{El}, I_{batt} (considering battery discharge) are replaced using equations (5.7), (5.2)

and (4.35) the final state-space equation is:

$$\begin{bmatrix} \dot{Q}_{batt} \\ \dot{Q}_c \\ \dot{T}_{acc}^{oil} \\ \dot{T}_{acc}^{H_2O} \end{bmatrix} = \begin{bmatrix} 0 & 0 & 0 & 0 \\ 0 & 0 & 0 & 0 \\ 0 & 0 & \frac{-K_{exch}}{m_{tank}^{oil} c_p^{oil}} & \frac{K_{exch}}{m_{tank}^{oil} c_p^{oil}} \\ 0 & 0 & \frac{K_{exch}}{m_{tank}^{oil} c_p^{oil}} & \frac{-K_{env}}{m_{tank}^{H_2O} c_p^{H_2O}} - \frac{K_{exch}}{m_{tank}^{oil} c_p^{oil}} \end{bmatrix} \begin{bmatrix} Q_{batt} \\ Q_c \\ T_{acc}^{oil} \\ T_{acc}^{H_2O} \end{bmatrix} +$$

$$+ \begin{bmatrix} 0 & 0 & 0 \\ 1 & 0 & 0 \\ 0 & \frac{2F\mu_{exch}}{m_{tank}^{oil} c_p^{oil} C} Q_c & 0 \\ 0 & 0 & \frac{-T_{acc}^{H_2O}}{m_{tank}^{H_2O}} \end{bmatrix} \begin{bmatrix} I_{load} \\ \dot{n}_{H_2}^A \\ \dot{m}_{HW} \end{bmatrix} + \begin{bmatrix} 0 & 0 \\ -1 & 0 \\ 0 & 0 \\ 0 & \frac{K_{env}}{m_{tank}^{H_2O} c_p^{H_2O}} \end{bmatrix} \begin{bmatrix} I_{PV} \\ T_{env} \end{bmatrix} +$$

$$+ \begin{bmatrix} \frac{\frac{Q_c}{C} - E_0 + K\frac{Q_{batt}^{max}}{Q_{batt}^{max} - Q_{batt}} Q_{batt} - Ae^{-BQ_{batt}}}{R_i - K\frac{Q_{batt}^{max}}{Q_{batt}^{max} - Q_{batt}}} \\ -\frac{\frac{Q_c}{C} - E_0 + K\frac{Q_{batt}^{max}}{Q_{batt}^{max} - Q_{batt}} Q_{batt} - Ae^{-BQ_{batt}}}{R_i - K\frac{Q_{batt}^{max}}{Q_{batt}^{max} - Q_{batt}}} + \frac{CP_{fc}}{Q_c} - I_{El,0} e^{\frac{CE_{oc} - Q_c}{CN_e A_e}} \\ 0 \\ 0 \end{bmatrix}, \quad (5.10)$$

where I_{load}, $\dot{n}_{H_2}^A$ and $\dot{m}_{HW}$ are input variables at the cost of having the following nonlinearities in the input matrix:

- State variables Q_c and $T_{acc}^{H_2O}$ inside the input matrix.
- An additional nonlinear vector term added at the end, function of state variables Q_{batt} and Q_c.

The same can be done in the case of battery charging using the expression of I_{batt} obtained from equation (4.37) instead. The state-space model, quite similar to the

previous one, is the following one:

$$\begin{bmatrix} \dot{Q}_{batt} \\ \dot{Q}_c \\ \dot{T}_{acc}^{oil} \\ \dot{T}_{acc}^{H_2O} \end{bmatrix} = \begin{bmatrix} 0 & 0 & 0 & 0 \\ 0 & 0 & 0 & 0 \\ 0 & 0 & \frac{-K_{exch}}{m_{tank}^{oil} c_p^{oil}} & \frac{K_{exch}}{m_{tank}^{oil} c_p^{oil}} \\ 0 & 0 & \frac{K_{exch}}{m_{tank}^{oil} c_p^{oil}} & \frac{-K_{env}}{m_{tank}^{H_2O} c_p^{H_2O}} - \frac{K_{exch}}{m_{tank}^{oil} c_p^{oil}} \end{bmatrix} \begin{bmatrix} Q_{batt} \\ Q_c \\ T_{acc}^{oil} \\ T_{acc}^{H_2O} \end{bmatrix} +$$

$$+ \begin{bmatrix} 0 & 0 & 0 \\ 1 & 0 & 0 \\ 0 & \frac{2F\mu_{exch}}{m_{tank}^{oil} c_p^{oil} C} Q_c & 0 \\ 0 & 0 & \frac{-T_{acc}^{H_2O}}{m_{tank}^{H_2O}} \end{bmatrix} \begin{bmatrix} I_{load} \\ \dot{n}_{H_2}^{A} \\ \dot{m}_{HW} \end{bmatrix} + \begin{bmatrix} 0 & 0 \\ -1 & 0 \\ 0 & 0 \\ 0 & \frac{K_{env}}{m_{tank}^{H_2O} c_p^{H_2O}} \end{bmatrix} \begin{bmatrix} I_{PV} \\ T_{env} \end{bmatrix} +$$

$$+ \begin{bmatrix} \frac{\frac{Q_c}{C} - E_0 + K \frac{Q_{batt}^{max}}{Q_{batt} + 0.1 Q_{batt}^{max}} Q_{batt} - A e^{-B Q_{batt}}}{R_i - K \frac{Q_{batt}^{max}}{Q_{batt} + 0.1 Q_{batt}^{max}}} \\ -\frac{\frac{Q_c}{C} - E_0 + K \frac{Q_{batt}^{max}}{Q_{batt} + 0.1 Q_{batt}^{max}} Q_{batt} - A e^{-B Q_{batt}}}{R_i - K \frac{Q_{batt}^{max}}{Q_{batt} + 0.1 Q_{batt}^{max}}} + \frac{C P_{fc}}{Q_c} - I_0 e^{\frac{Q_c}{C N_e A e}} \\ 0 \\ 0 \end{bmatrix} \tag{5.11}$$

When trying to implement the simulation of this state-space system, which must have results similar to the global Matlab/Simulink system detailed in the previous chapter, a little variation is needed. For computational reasons and to preserve causality, the state-space is rearranged assigning the fuel cell imput variables as seen in the simple model from Figure 4.5. Consequently, U_{fc} is considered as a new input variable, U as an state variable (connected by an internal resistance r_i) and fuel cell current as

$I_{fc} = \frac{E_{oc}-U_{fc}-U}{r_i i_0}$. The state-space to be simulated is the following one:

$$\begin{bmatrix} \dot{U} \\ \dot{Q}_{batt} \\ \dot{Q}_c \\ \dot{T}_{acc}^{oil} \\ \dot{T}_{acc}^{H_2O} \end{bmatrix} = \begin{bmatrix} \frac{-3}{\tau} & 0 & 0 & 0 & 0 \\ 0 & 0 & 0 & 0 & 0 \\ 0 & 0 & 0 & 0 & 0 \\ 0 & 0 & 0 & \frac{-K_{exch}}{m_{tank}^{oil} c_p^{oil}} & \frac{K_{exch}}{m_{tank}^{oil} c_p^{oil}} \\ 0 & 0 & 0 & \frac{K_{exch}}{m_{tank}^{oil} c_p^{oil}} & \frac{-K_{env}}{m_{tank}^{H_2O} c_p^{H_2O}} - \frac{K_{exch}}{m_{tank}^{oil} c_p^{oil}} \end{bmatrix} \begin{bmatrix} U \\ Q_{batt} \\ Q_c \\ T_{acc}^{oil} \\ T_{acc}^{H_2O} \end{bmatrix} +$$

$$+ \begin{bmatrix} 0 & 0 & 0 \\ 0 & 0 & 0 \\ 1 & 0 & 0 \\ 0 & \frac{\mu_{exch}}{m_{tank}^{oil} c_p^{oil}} \frac{E_{oc}-U_{fc}-U}{r_i} & 0 \\ 0 & 0 & \frac{-1}{m_{tank}^{H_2O} c_p^{H_2O}} \end{bmatrix} \begin{bmatrix} I_{load} \\ U_{fc} \\ Q_{HW} \end{bmatrix} + \begin{bmatrix} 0 & 0 \\ 0 & 0 \\ -1 & 0 \\ 0 & 0 \\ 0 & \frac{K_{env}}{m_{tank}^{H_2O} c_p^{H_2O}} \end{bmatrix} \begin{bmatrix} I_{PV} \\ T_{env} \end{bmatrix} +$$

$$+ \begin{bmatrix} \frac{3NAK_c}{\tau} \ln\left(\frac{E_{oc}-U_{fc}-U}{r_i i_0}\right) \\ I_{batt} \\ -I_{batt} + \frac{E_{oc}-U_{fc}-U}{r_i} - I_0 e^{\frac{Q_c}{CN_e A_e}} \\ 0 \\ 0 \end{bmatrix}, \tag{5.12}$$

where K_c is the fuel cell converter gain and I_{batt} follows the expression for battery discharging or charging as done before.

5.2 Control architecture

The studied system is controlled at two levels, a local one and a global one. On a local level, proportional-integral (PI) controllers are designed to ensure local stability, as explained in Chapter 4. Once these different system elements have been stabilised, a global supervisory control strategy is defined. The structure is the one shown in Figure 5.1.

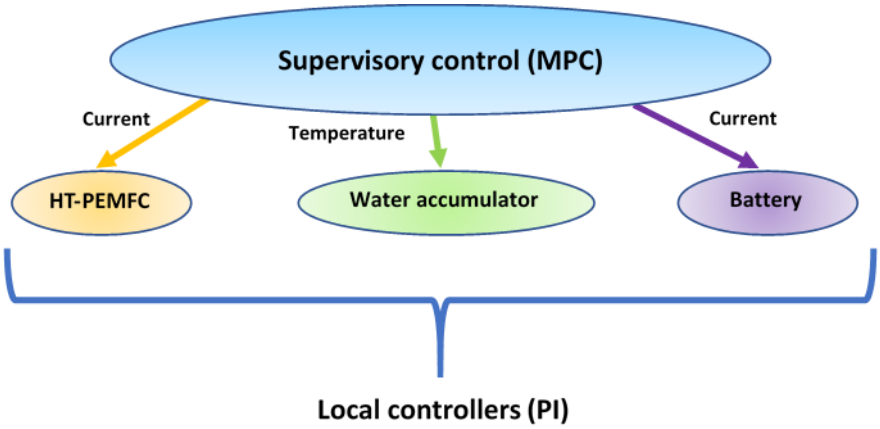

Figure 5.1: Control structure of the CHP-HT-PEMFC system

5.2.1 Local controllers

As mention in Chapter 4, elements in the CHP system include PI controllers to ensure stability at a local level. The global system control variables will be computed using an online controller with the characteristics presented below.

5.2.2 Global controller

The system is controlled using a model predictive control (MPC) strategy, which is designed according to the following steps:

1. Select control objectives for the case studied.
2. Formulate this control objectives as mathematical subfunctions to be included in a global objective function.
3. Select weighting functions to prioritise some objective functions above others, writing the objective function as a linear combination of weighting functions and its corresponding objective subfunction.
4. Define an optimisation problem with this objective function and constraints.
5. Select variables to act as control variables.
6. Include the model equations as constraints for this optimisation problem.

7. Limit variables with minimum and maximum values (hard constraints).
8. Include other limitations for some variables in the shape of soft constraints.
9. Select a control horizon and prediction horizon so that the optimisation problem will solve the problem for the current iteration and some in the future, to anticipate results.
10. Include disturbances and pay attention at their predictability and variation.
11. Implement the optimisation online to provide the system plant's inputs solving the optimisation problem.

5.3 Control objectives

When designing the CHP system, the main target is being able to feed both the thermal and the electrical demand in a efficient manner. In order to apply an MPC controller, it is necessary to transform this generic objective into a cost function and restrictions on the system variables. As usual in the MPC [37, 61], in this work the cost function will be constructed as the linear combination of different cost functions, each of which will be directly related to a specific concept. For this, a prediction horizon N_{total}, i.e. number of iterations predicted, and $u_{k,i}$ i-components of the input vector (equation(6.14)) for a certain iteration k are considered. All norms used represent 1-norm. This will lead to what is known as a multi-objective optimization problem.

In the case of the system studied, and based on specifications of efficiency, mitigation degradation and environmental sustainability, control objectives to be considered in this work are the following:

- Hydrogen consumed: Consumed hydrogen is proportional to the fuel cell current.
- Fuel cell current variation. Fast variation in the fuel cell current might produce starvation in the fuel cell which is one of the main degradation sources [43].
- Minimising energy.
- Minimising electrical power transferred to thermal.

- Minimising variation of electrical power transferred to thermal.
- Minimising electrical power supplied by the grid.
- Minimising variation of electrical power supplied by the grid.
- Minimising electrical power supplied to the grid.
- Minimising variation of electrical power supplied to the grid.
- Minimising thermal power extracted as waste.
- Minimising variation of thermal power extracted as waste.

These control objectives will be translated into subfunctions to be included in the global objective function in the following chapter.

Chapter 6

Energy management strategy

Shine here to us, and thou art everywhere;

This bed thy centre is, these walls thy sphere.

From *The Sun Rising*, by John Donne

The control system described in the previous chapter must be used in the energy management problem tackled during this thesis. Consequently, in this chapter, the optimisation problem is described, simulated and the first results of the global CHP system shown and discussed.

6.1 Optimisation problem. Mathematical formulation

To match the values of heat and electrical power generated to the demand in the case of a specific house a model predictive control problem is formulated. The system state-space obtained from a thermal and electrical balance is used as a constraint for the optimisation problem in its discretised form.

6.1.1 Control objectives

Control objectives have been summarised as subfunctions f_i and are renamed as follows:

- Hydrogen consumed: Consumed hydrogen is proportional to the fuel cell current.

Consequently, the following cost function is proposed.

$$f_{H_2} = \frac{\sum_{i=0}^{N_{total}} \|u_{k+i,1}\|}{I_{fc,max}} \tag{6.1}$$

- Fuel cell current variation: Fast variation in the fuel cell current might produce starvation in the fuel cell which is one of the main degradation sources [43]. To minimize this, the following cost function is suggested:

$$f_{H_2,var} = \frac{\sum_{i=0}^{N_{total}} \|u_{k+i,1} - u_{k+i-1,1}\|}{I_{fc,max}} \tag{6.2}$$

- Minimising energy:

$$f_e = \sum_{i=0}^{N_{total}} \|e_{k+i}\| \tag{6.3}$$

- Minimising electrical power transferred to thermal:

$$f_{tr} = \frac{\sum_{i=0}^{N_{total}} \|u_{k+i,2}\|}{P_{tra}^{max}} \tag{6.4}$$

- Minimising variation of electrical power transferred to thermal:

$$f_{tr,var} = \frac{\sum_{i=0}^{N_{total}} \|u_{k+i,2} - u_{k-1,2}\|}{P_{tra}^{max}} \tag{6.5}$$

- Minimising electrical power supplied by the grid:

$$f_{grid^{in}} = \frac{\sum_{i=0}^{N_{total}} \|u_{k+i,4}\|}{P_{e,loss}^{max}} \tag{6.6}$$

- Minimising variation of electrical power supplied by the grid, using values from two consecutive iterations ($k-1$ and k):

$$f_{grid^{in},var} = \frac{\sum_{i=0}^{N_{total}} \|u_{k+i,4} - u_{k+i-1,4}\|}{P_{e,loss}^{max}} \tag{6.7}$$

- Minimising electrical power supplied to the grid:

$$f_{grid^{out}} = \frac{\sum_{i=0}^{N_{total}} \|u_{k+i,3}\|}{P_{e,loss}^{max}} \tag{6.8}$$

- Minimising variation of electrical power supplied to the grid, using values from two consecutive iterations ($k-1$ and k):

$$f_{grid^{out},var} = \frac{\sum_{i=0}^{N_{total}} \|u_{k+i,3} - u_{k+i-1,3}\|}{P_{e,loss}^{max}} \tag{6.9}$$

- Minimising thermal power extracted as waste:

$$f_{th^{out}} = \frac{\sum_{i=0}^{N_{total}} \|u_{k+i,5}\|}{P_{t,loss}^{max}} \tag{6.10}$$

- Minimising variation of thermal power extracted as waste, using values from two consecutive iterations ($k-1$ and k):

$$f_{th^{out},var} = \frac{\sum_{i=0}^{N_{total}} \|u_{k+i,5} - u_{k+i-1,5}\|}{P_{t,loss}^{max}} \tag{6.11}$$

6.1.2 Objective function

The objective function is calculated adding up all control objectives presented in the previous section f_i, each of them with its weight function w_i, to prioritise some objectives above others. As previously discussed the cost function is defined as

$$J(\mathbf{x}_k, \mathbf{u}_k) = \sum_{i=1}^{11} w_i \cdot f_i(\mathbf{x}_k, \mathbf{u}_k)$$
$$\min_{\mathbf{u}_k} J(\mathbf{x}_k, \mathbf{u}_k) \tag{6.12}$$

6.2 Control model

Although it is possible to propose an MPC controller for a nonlinear and complex model like the one proposed in equation (5.12), in order to obtain an easily implementable controller, a linear model will be created that keeps the main characteristics of the initial model. This model will be directly formulated as a discrete-time state-space model.

The state vector is defined as

$$\mathbf{x} = \begin{bmatrix} E_{elec}^{bat} \\ E_{therm}^{acc} \end{bmatrix} \tag{6.13}$$

formed by the following 2 states:

- Stored electrical energy in the battery E_{elec}^{bat}.
- Stored thermal energy in the water accumulator E_{therm}^{acc}.

Additionally, the system has a total of 5 inputs in input vector $\mathbf{u}$ and 2 variables in disturbance vector $\mathbf{d}$:

$$\mathbf{u} = \begin{bmatrix} I_{fc} \\ W_{tra} \\ W_{grid_{in}} \\ W_{grid_{out}} \\ W_{accum_{out}} \end{bmatrix}, \quad \mathbf{d} = \begin{bmatrix} W_{d_{elec}} \\ W_{d_{therm}} \end{bmatrix} \tag{6.14}$$

These variables stand for:

- Fuel cell current I_{fc}.
- Electrical to thermal energy transfer variable if necessary for demand purposes W_{tra}.
- 3 security elements to connect to grid and the accumulator if necessary for demand purposes $W_{grid_{in}}$, $W_{grid_{out}}$ and $W_{accum_{out}}$.
- Electrical and thermal demands $W_{d_{elec}}$ and $W_{d_{therm}}$ are considered as perturbations.

This model can be written as:

$$\begin{aligned} \mathbf{x}_{k+1} &= \mathbf{A}\mathbf{x}_k + \mathbf{B}\mathbf{u}_k + \mathbf{G_d}\mathbf{d} \\ \mathbf{y}_k &= \mathbf{C}\mathbf{x}_k, \end{aligned} \tag{6.15}$$

where

$$\begin{aligned} \mathbf{A} &= \begin{bmatrix} 1 & 0 \\ 0 & 1 - \frac{K_{env} T_s}{m_{acc} C_{H_2O}} \end{bmatrix}, \\ \mathbf{B} &= T_s \begin{bmatrix} \eta_{conv} V_{fc}^{nom} & \eta_{exch}(V_q^{nom} - V_{fc}^{nom}) \\ -1 & \eta_{tra} \\ 1 & 0 \\ -1 & 0 \\ 0 & -1 \\ -1 & 0 \\ 0 & -1 \end{bmatrix}^T, \\ \mathbf{C} &= \mathbf{I_{2x2}}, \quad \mathbf{G_d} = -T_s \mathbf{I_{2x2}}. \end{aligned} \tag{6.16}$$

Parameters included in the model can be defined as:

- K_{env} is the environment losses constant.
- T_s is the sampling time of the model predictive control.
- m_{acc} is the mass of water in the accumulator.
- C_{H_2O} is water's specific heat.
- η_{conv} is the converter efficiency.
- η_{exch} is the heat exchanger efficiency.
- η_{tra} is the transfer resistance.
- V_{fc}^{nom} is the electrical voltage due to linearisation.
- V_{q}^{nom} is the thermal voltage due to linearisation.

6.3 MPC constraints

Once the structure of the objective function and control model have been defined, MPC contraints need to be presented. This model's variables are constrained with upper and lower bounds, using soft constraints, which should be avoided when possible, and hard constraints, which cannot be violated. Demands are considered as perturbation $\mathbf{d}_k$ and included as inputs.

Current constraints are:

$$\begin{aligned} I_{fc,min} \leq u_{k,1} \leq I_{fc,max} \\ -dI_{fc,max} \leq u_{k,1} - u_{k-1,1} \leq dI_{fc,max} \end{aligned} \tag{6.17}$$

Energy constraints are:

$$\begin{aligned} x_{k+1} \geq E_{e,llim} - (E_{e,llim} - E_{e,min})e_k \\ x_{k+1} \leq E_{e,hlim} + (E_{e,max} - E_{e,llim})e_k \\ E_{t,min} \leq x_{k+1,2} \leq E_{t,max} \\ 0 \leq e_k \leq 1 \end{aligned} \tag{6.18}$$

Transfer resistance constraints are:

$$P_{tra,min} \leq u_{k,2} \leq P_{tra,max} \tag{6.19}$$

Battery constraints are:

$$\begin{aligned} y_k &\leq (Batt_{ll} - x_{k+1,1})E_{e,max} + 1 \\ u_{k,3} &\leq P_{e,loss}^{max} y_k \\ P_{e,loss}^{min} \leq u_{k,3} &\leq P_{e,loss}^{max} \end{aligned} \tag{6.20}$$

Battery to grid constrains are:

$$\begin{aligned} y_k &\leq \frac{x_{k+1,1} - Batt_{hl}}{E_{e,max}} + 1 \\ u_{k,4} &\leq P_{e,loss}^{max} y_k \\ P_{e,loss}^{min} \leq u_{k,4} &\leq P_{e,loss}^{max} \end{aligned} \tag{6.21}$$

Accumulator emptying constrains are:

$$\begin{aligned} y_k &\leq \frac{x_{k+1,2} - Accu_{hl}}{E_{t,max}} + 1 \\ u_{k,5} &\leq P_{t,loss}^{max} y_k \\ P_{t,loss}^{min} \leq u_{k,5} &\leq P_{t,loss}^{max} \end{aligned} \tag{6.22}$$

All these equations (6.17) to 6.22 have their variables defined as follows:

- $\mathbf{x}_k = [E_{elec}^{bat}, E_{therm}^{acc}]^T$ is the state vector composed by stored electrical energy in the battery E_{elec}^{bat} and total stored thermal energy in the water accumulator E_{therm}^{acc}.
- $\mathbf{u}_k$ is the input vector defined in equation (6.14) with variables defined in the discrete domain. Its first component $u_{k,1}$ corresponds to the HT-PEMFC inlet electrical current I_k, proportional to hydrogen flow. Elements $u_{k,2}$ to $u_{k,5}$ variables W_{tra}, $W_{grid_{in}}$, $W_{grid_{out}}$, $W_{accum_{out}}$ also defined in equation (6.14).
- $\mathbf{d}_k = [D_{elec}, D_{therm}^{HW} + D_{therm}^{SH}]^T$ is the perturbation vector composed by expected electricity demand D_{elec} and thermal energy for hot water D_{therm}^{HW} and space heating D_{therm}^{SH}. It corresponds to the last 2 values of $\mathbf{u}_k$, i.e. $u_{k,6}$ and $u_{k,7}$.

- e_k a variable to constrain soft constraints. When $e_k = 0$, only soft constraint values remain, forcing the state of charge to be between both. On the contrary, if $e_k = 1$, the soft constraints term cancels out and the battery state of charge is limited between its minimum and maximum values.
- y_k is a binary variable that, when set to 0, prevents the input from activating (equation (6.20)). The first inequality in equation (6.21) is the responsible of forcing the binary variable to 0 when the state of charge is above a set value.
- $Batt_{min}$, $Batt_{l1}$, $Batt_{h1}$, $Batt_{max}$ are minimum, lowest recommended, highest recommended and maximum battery limits.
- $Accu_{min}$, $Accu_{h1}$, $Accu_{max}$ are minimum, highest recommended and maximum accumulator temperatures.
- $I_{fc,min}$, $I_{fc,max}$ are minimum and maximum electrical current limits.
- $dI_{fc,min}$, $dI_{fc,max}$ are minimum and maximum electrical current variation limits.
- P_{tra}^{min}, P_{tra}^{max} are minimum and maximum transfer resistance limits.
- $P_{e,loss}^{min}$, $P_{e,loss}^{max}$ are minimum and maximum electrical valve limits.
- $P_{t,loss}^{min}$, $P_{t,loss}^{max}$ are minimum and maximum thermal valve limits.

The steps to be followed during the control process are:

- A prediction horizon for the problem N_{total} and a control horizon $N < N_{total}$ are defined.
- Expected demand values for horizon N are defined, $\hat{\mathbf{d}}_k \cdots \hat{\mathbf{d}}_{k+N}$.
- The optimisation problem to obtain the control action u_k is solved so that the following N predicted states $\hat{\mathbf{x}}_k \cdots \hat{\mathbf{x}}_{k+N}$ match the specifications.
- The process is repeated for each instant k.

Using values presented before, an optimisation problem as shown in equation (6.12) is implemented. To do so, the Yalmip environment is embedded in Matlab. Yalmip is a toolbox able to implement linear matrix inequalities in optimisation problems, as the case of MPC constraints. Results obtained are states $\mathbf{x}_k = [E_{elec}^{bat}, E_{therm}^{acc}]^T$ (energy storage units) and control input $u_{k,1} = I_k$ (fuel cell stack current).

6.4 Prediction horizon generation

For all cases, a whole day is simulated, with 15 minutes time between iterations. This makes 97 iterations for a whole day, being the first and the last the ones corresponding to 0 a.m. o'clock. Prediction horizon is initially defined as the whole day, imposing known demands from historical data. In following chapters, when the complete system is simulated and parameters in the MPC algorithm have been tuned, a more strict and short-term prediction will be impose

6.5 First results

The algorithm presented is tested using a simplified plant and the complex one presented in Chapter 4 and sumarised in equation (5.12). This simplified model does not include solar panel, hydrogen plant and electrolyser, thus working as a good test plant for the MPC algorithm presented.

6.5.1 Simplified model's results

First of all, the presented control strategy is tested with a simple model, with the following simplifications:

- Oil tank dynamics simplified to a single efficiency constant.
- Fuel cell current supplied directly from a hydrogen source.
- Photovoltaic panel and electrolyser are not considered.

The control algorithm from previous section is tested in the house model detailed above, in different scenarios. These correspond to a whole day with electrical and

thermal demands associated to different months of the year. The time between iterations k used for the prediction is 15 minutes and the prediction horizon is $N_{total} = 97$. Weight functions used are $w_1 = 0.078$, $w_2 = 0.005$, $w_3 = 0.005$, $w_4 = 0.156$, $w_5 = 0.005$, $w_6 = 0.195$, $w_7 = 0.005$, $w_8 = 0.195$, $w_9 = 0.005$, $w_{10} = 0.195$ and $w_{11} = 0.005$. For each scenario, the following variables are monitored:

- Electrical demand.
- Thermal demand.
- Fuel cell current or intensity
- Battery state of charge in percentage.
- Water accumulator temperature.
- Electrical power transferred to add additional heat through a resistance.
- Electrical electrical power input, coming from the grid.
- Electrical electrical power output, going to the grid.

To test whether the control strategy works as expected battery state of charge and water accumulator temperature cannot exceed their minimum and maximum values, imposed by the previously mentioned constraints. Fuel cell current should also stay between certain limits. Additionally, some scenarios may need extra heat, in case of too high thermal demand, or extra heat may be extracted as waste, when thermal demand is too low. Both phenomena will be included in extra plots when they are not zero, and a similar thing is done for electrical power going in or out of the external electrical grid.

Demand profiles are defined according to those of a house located by the sea in the Spanish Mediterranean coast, not considering Summer season, as it is not demanding enough in terms of thermal demand.

6.5.1.1 Simplified model's January results

Results for a typical day of January are the ones seen in Figure 6.1.

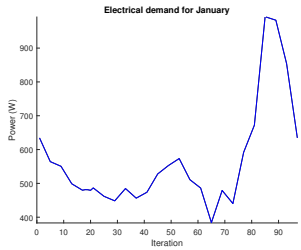

(a) Electrical demand on a day of January (simplified model)

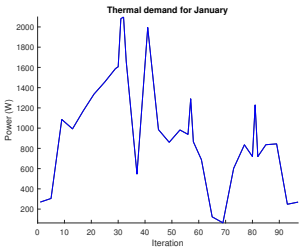

(b) Thermal demand on a day of January (simplified model)

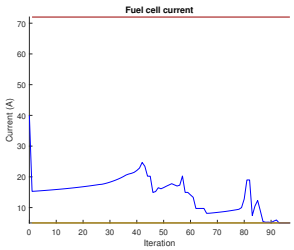

(c) Fuel cell current on a day of January (simplified model)

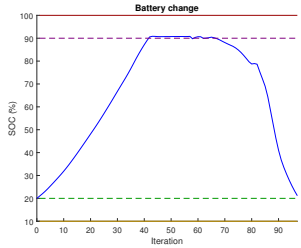

(d) Electrical battery state of charge on a day of January (simplified model)

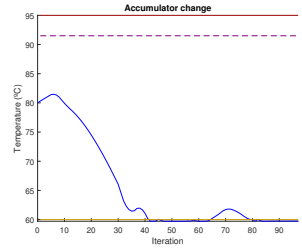

(e) Water accumulator temperature on a day of January (simplified model)

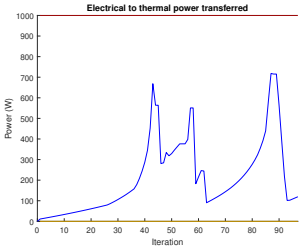

(f) Electrical power transferred to the thermal system on a day of January (simplified model)

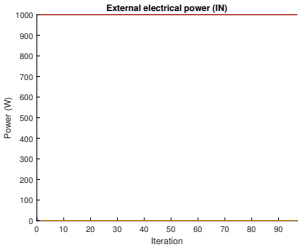

(g) Electrical power supplied by the grid on a day of January (simplified model)

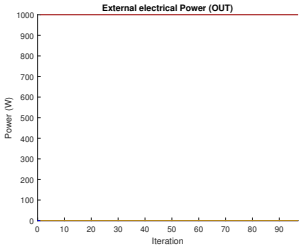

(h) Electrical power supplied to the grid on a day of January (simplified model)

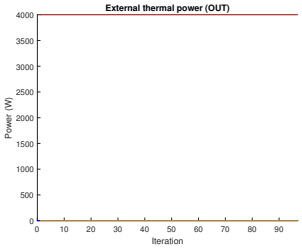

(i) Thermal power extracted as waste on a day of January (simplified model)

Figure 6.1: Simplified model's results for a day of January (200 kg of water in the accumulator)

It can be seen that fuel cell current is low enough and does not present sudden changes (Figure 6.1c), the state of charge of the electrical battery remains between boundaries (Figure 6.1d) and water in the accumulator keeps a reasonable temperature (Figure 6.1e). Additionally, extra thermal power is obtained from the electrical system to match the high thermal demand (Figure 6.1f).

6.5.1.2 Simplified model's April results

A similar study is done for April and the corresponding results are displayed in Figure 6.2.

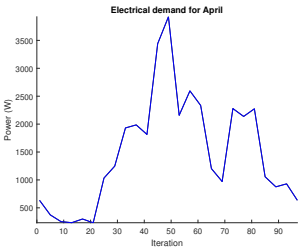

(a) Electrical demand on a day of April (simplified model)

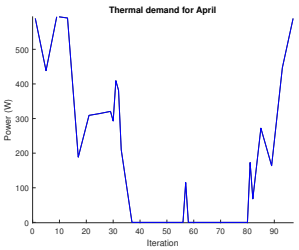

(b) Thermal demand on a day of April (simplified model)

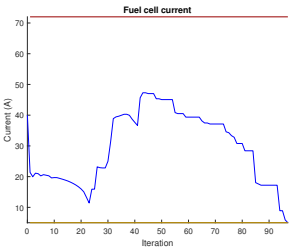

(c) Fuel cell current on a day of April (simplified model)

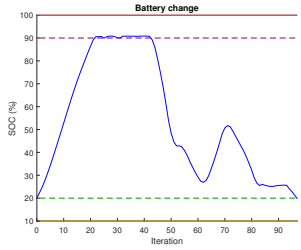

(d) Electrical battery state of charge on a day of April (simplified model)

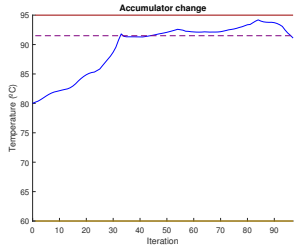

(e) Water accumulator temperature on a day of April (simplified model)

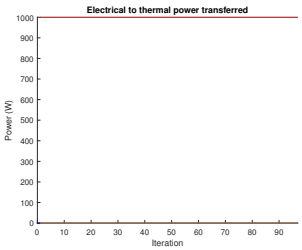

(f) Electrical power transferred to the thermal system on a day of April (simplified model)

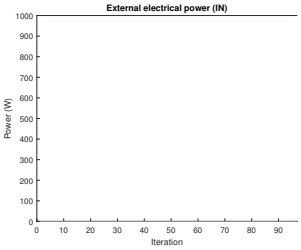

(g) Electrical power supplied by the grid on a day of April (simplified model)

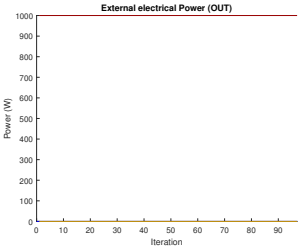

(h) Electrical power supplied to the grid on a day of April (simplified model)

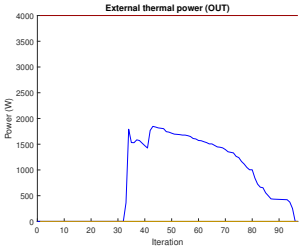

(i) Thermal power extracted as waste on a day of April (simplified model)

Figure 6.2: Simplified model's results for a day of April (200 kg of water in the accumulator)

The main difference with the case of January is that extra heat produced is not used as thermal demands are not that high (Figure 6.2i). This lower thermal demand

is responsible for having a higher water temperature in the accumulator (Figure 6.2e), which is close to the upper constraint limit. This is the opposite behaviour to the January scenario, where this temperature was close to the lower constraint limit, due to constant use of water for thermal purposes.

6.5.2 Main model's results

Once the system has been tested using its simplified version, the complete system detailed in previous chapters is used, so that a comparison can be made. This model still does not include solar panel and electrolyser, as these will be included later in the last chapter and final simulations. Simulation conditions and scenarios are the same ones as the ones studied for the simplified model.

6.5.2.1 Main model's January results

Results for a typical day of January are the ones seen in Figure 8.1.

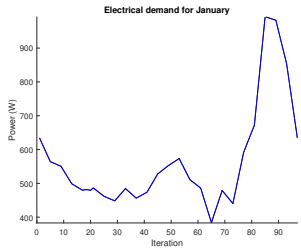

(a) Electrical demand on a day of January

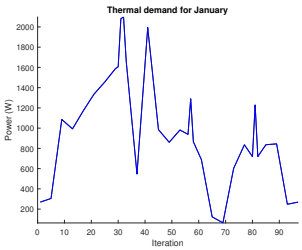

(b) Thermal demand on a day of January

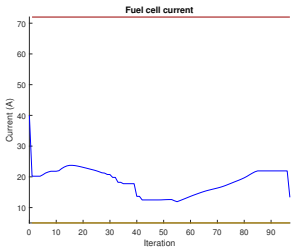

(c) Fuel cell current on a day of January

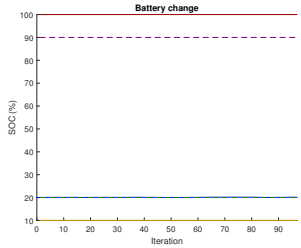

(d) Electrical battery state of charge on a day of January

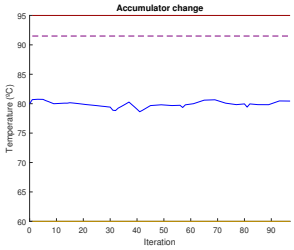

(e) Water accumulator temperature on a day of January

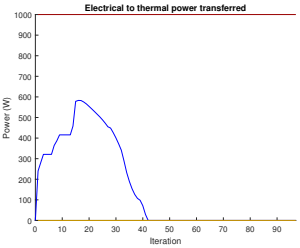

(f) Electrical power transferred to the thermal system on a day of January

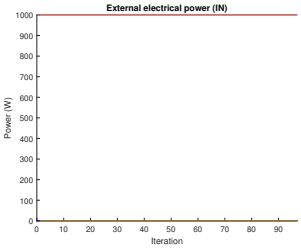

(g) Electrical power supplied by the grid on a day of January

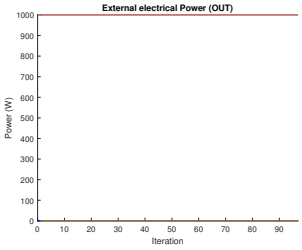

(h) Electrical power supplied to the grid on a day of January

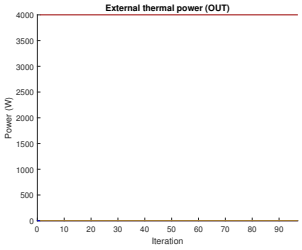

(i) Thermal power extracted as waste on a day of January

Figure 6.3: Results for a day of January (200 kg of water in the accumulator)

Comparing these results to the ones obtained in the case of the simplified model (Figure 6.2), the following differences can be noticed:

- Fuel cell current follows different trajectories but stays between similar values in both simplified model (Figure 8.1c) and the simplified one (Figure 6.1c).
- Battery state of change in the case of the simplified system (Figure 6.1d) almost reaches the top level allowed for the battery state of charge. In contrast, the state of charge corresponding to the main model barely changes (Figure 8.1d). This

means the electrical converter controlling battery current needs to be adjusted properly and weight functions corresponding to it tuned when needed.

- Overcooling in the water accumulator in the case of the simplified model (Figure 6.1e) forces the system to need a different amount of power coming from the electrical system to be transferred as heat (Figure 6.1f). This is different in the case of the main model, where water temperature remains stable (Figure 8.1e) and extra power coming from the electrical part of the system has a different profile (Figure 8.1f).
- No external power coming from the grid is needed in any of the cases (Figure 8.1g), and no electrical or thermal energy is released in any case (Figures 6.1h, 6.1i, 8.1h, and 8.1i).

Varying water mass in the accumulator In order to understand the limits of the model, the amount of water in the accumulator is changed and new results for a day of January are calculated. Water mass of 200 kg used in previous Figure 8.1 is first reduced to obtain results from Figure 6.4, corresponding to 100 kg of water, and Figure 6.5, corresponding to 70 kg of water.

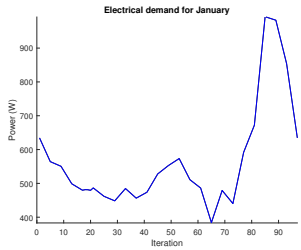

(a) Electrical demand on a day of January

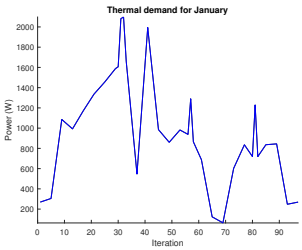

(b) Thermal demand on a day of January

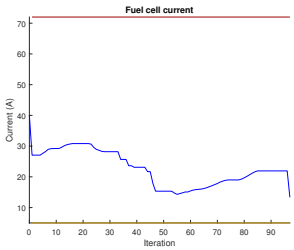

(c) Fuel cell current on a day of January

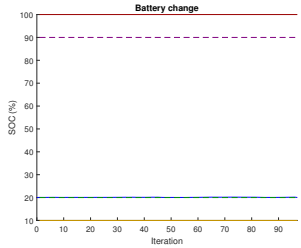

(d) Electrical battery state of charge on a day of January

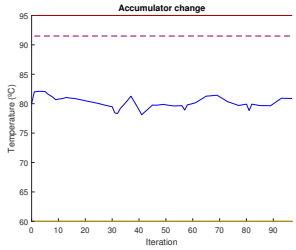

(e) Water accumulator temperature on a day of January

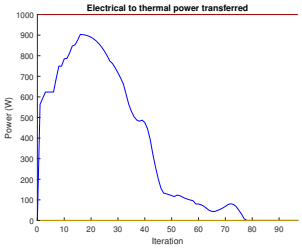

(f) Electrical power transferred to the thermal system on a day of January

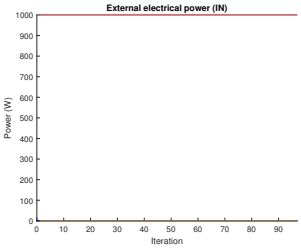

(g) Electrical power supplied by the grid on a day of January

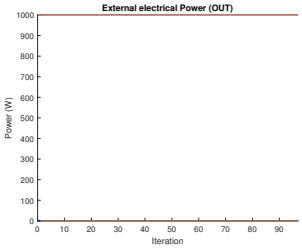

(h) Electrical power supplied to the grid on a day of January

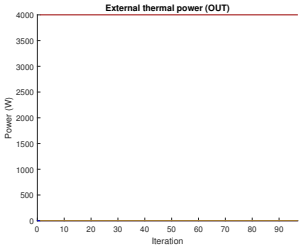

(i) Thermal power extracted as waste on a day of January

Figure 6.4: Results for a day of January (100 kg of water in the accumulator)

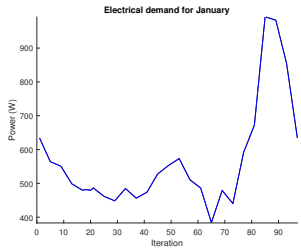

(a) Electrical demand on a day of January

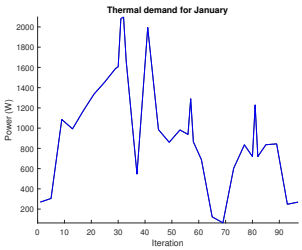

(b) Thermal demand on a day of January

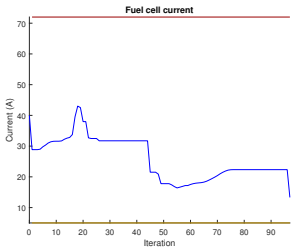

(c) Fuel cell current on a day of January

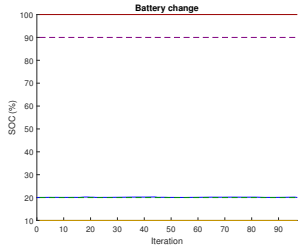

(d) Electrical battery state of charge on a day of January

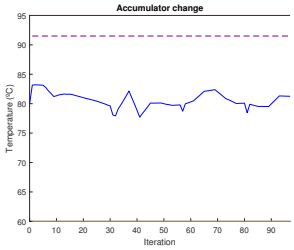

(e) Water accumulator temperature on a day of January

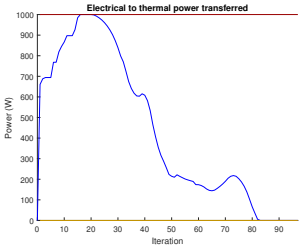

(f) Electrical power transferred to the thermal system on a day of January

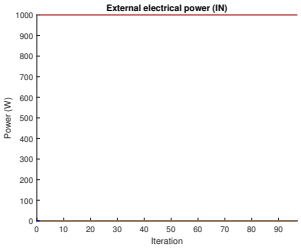

(g) Electrical power supplied by the grid on a day of January

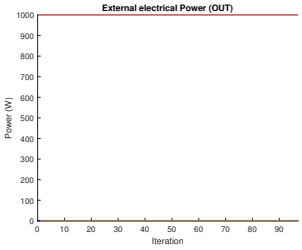

(h) Electrical power supplied to the grid on a day of January

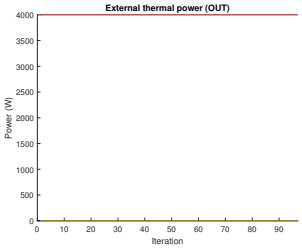

(i) Thermal power extracted as waste on a day of January

Figure 6.5: Results for a day of January (70 kg of water in the accumulator)

It can be seen in these Figures 6.4 and 6.5 that, as expected, reducing the amount of water in the accumulator makes the system highly dependant on external heat obtained transforming electrical energy to heat (Figures 6.4f and 6.5f).

Finally, the amount of water is increased to 400 kg and its results are seen in Figure 6.6.

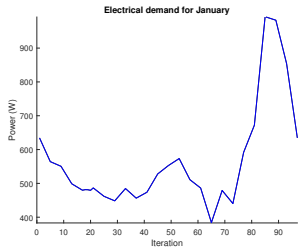

(a) Electrical demand on a day of January

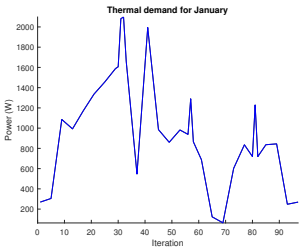

(b) Thermal demand on a day of January

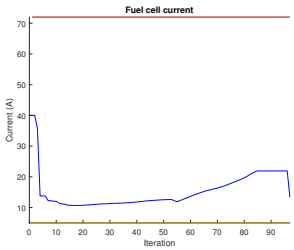

(c) Fuel cell current on a day of January

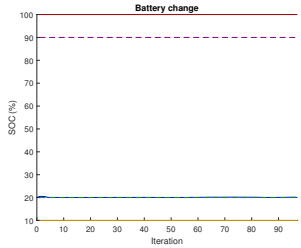

(d) Electrical battery state of charge on a day of January

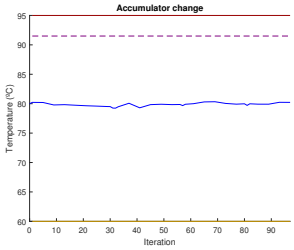

(e) Water accumulator temperature on a day of January

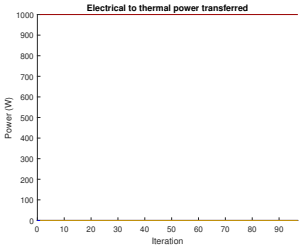

(f) Electrical power transferred to the thermal system on a day of January

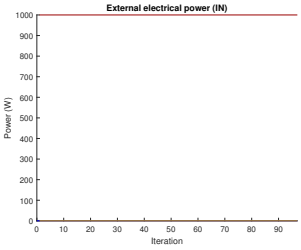

(g) Electrical power supplied by the grid on a day of January

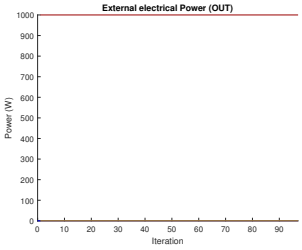

(h) Electrical power supplied to the grid on a day of January

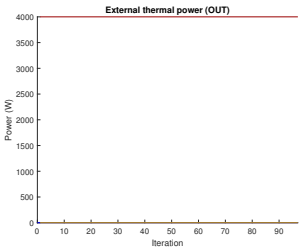

(i) Thermal power extracted as waste on a day of January

Figure 6.6: Results for a day of January (400 kg of water in the accumulator)

As seen in Figure 6.6f, the system is less dependant on extra heat supplied by other means when there is enough water in the accumulator. However, extra costs associated to higher accumulators should be avoided.

Varying oil mass Similarly, the initial oil mass of 100 kg is reduced to 25 kg and 50 kg respectively in Figures 6.7 and 6.8.

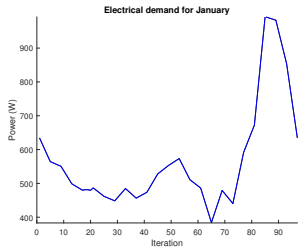

(a) Electrical demand on a day of January

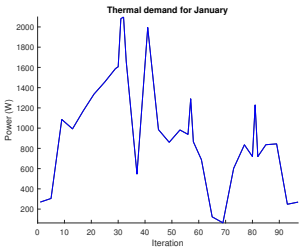

(b) Thermal demand on a day of January

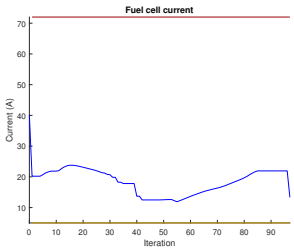

(c) Fuel cell current on a day of January

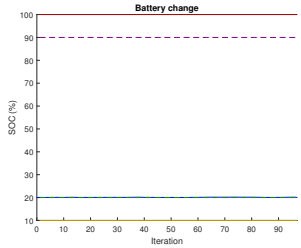

(d) Electrical battery state of charge on a day of January

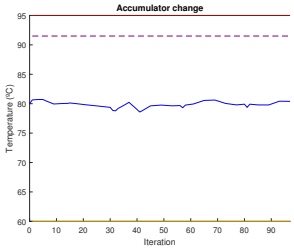

(e) Water accumulator temperature on a day of January

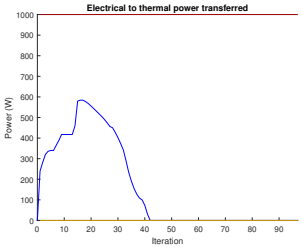

(f) Electrical power transferred to the thermal system on a day of January

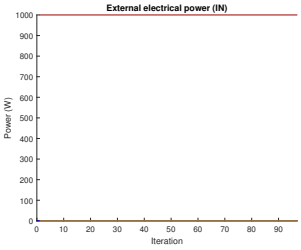

(g) Electrical power supplied by the grid on a day of January

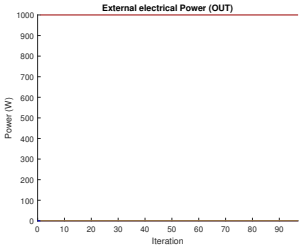

(h) Electrical power supplied to the grid on a day of January

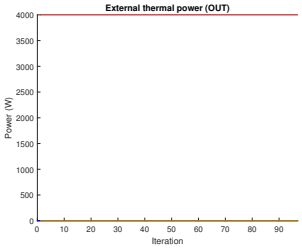

(i) Thermal power extracted as waste on a day of January

Figure 6.7: Results for a day of January (25 kg of oil in the tank)

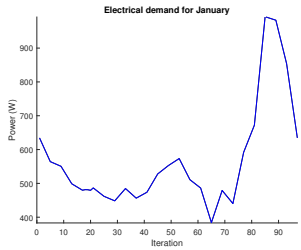

(a) Electrical demand on a day of January

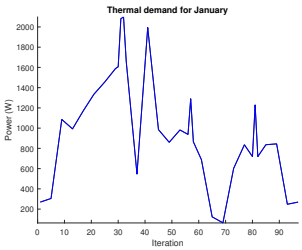

(b) Thermal demand on a day of January

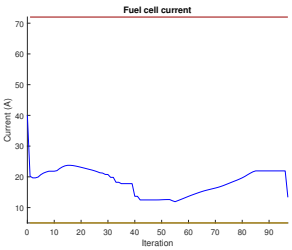

(c) Fuel cell current on a day of January

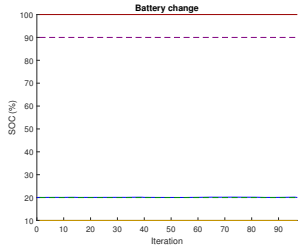

(d) Electrical battery state of charge on a day of January

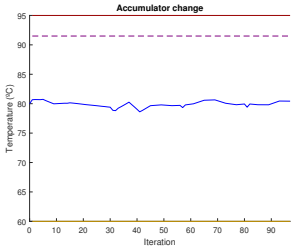

(e) Water accumulator temperature on a day of January

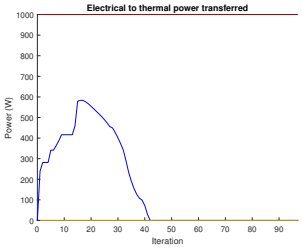

(f) Electrical power transferred to the thermal system on a day of January

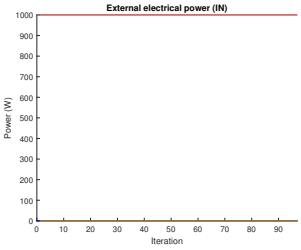

(g) Electrical power supplied by the grid on a day of January

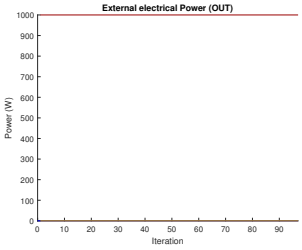

(h) Electrical power supplied to the grid on a day of January

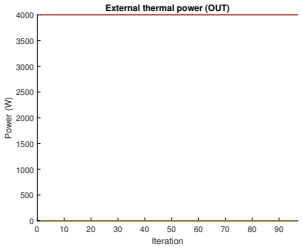

(i) Thermal power extracted as waste on a day of January

Figure 6.8: Results for a day of January (50 kg of oil in the tank)

Comparing these results from Figures 6.7 and 6.8, corresponding to a quarter and half the initial oil mass, to the initial ones seen in Figure 8.1 it can be seen that they are quite similar, showing that the amount of oil in the tank does not affect the system behaviour the way the amount of water in the accumulator does.

6.5.2.2 Main model's April results

Using the initial values of 200 kg of water and 100 of oil, results for a day of April are calculated as done in the case of January. Results are seen in Figure 8.4.

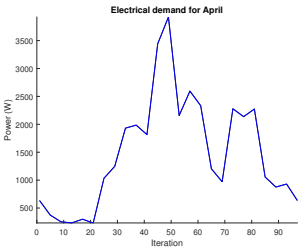

(a) Electrical demand on a day of April

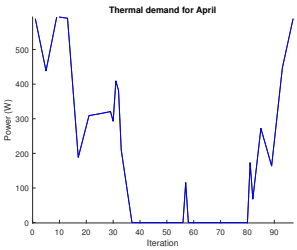

(b) Thermal demand on a day of April

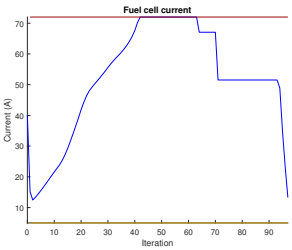

(c) Fuel cell current on a day of April

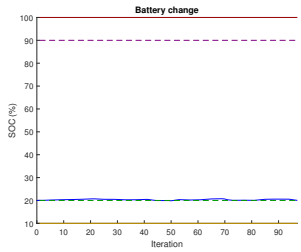

(d) Electrical battery state of charge on a day of April

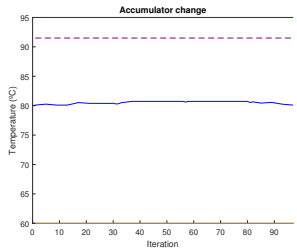

(e) Water accumulator temperature on a day of April

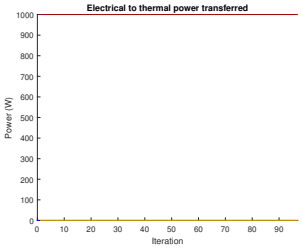

(f) Electrical power transferred to the thermal system on a day of April

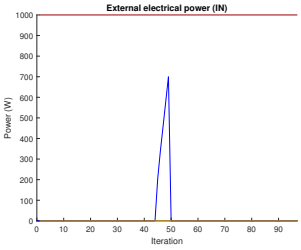

(g) Electrical power supplied by the grid on a day of April

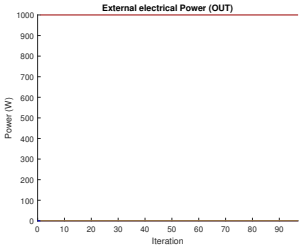

(h) Electrical power supplied to the grid on a day of April

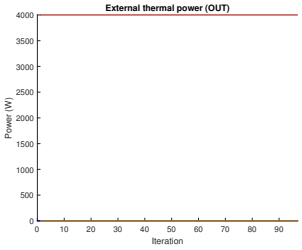

(i) Thermal power extracted as waste on a day of April

Figure 6.9: Results for a day of April (200 kg of water in the accumulator)

Comparing these results to the ones obtained in the case of the simplified model (Figure 6.2), the following differences can be noticed:

- Fuel cell current is much higher (reaching top constraints) in the case of the non simplified model (Figure 8.4c) and much lower in the case of the simplified one (Figure 6.2c).
- Battery state of change in the case of the simplified system (Figure 6.2d) compensates this low fuel cell current consumption by almost reaching the top level

allowed for the battery state of charge. In contrast, the state of charge corresponding to the main model barely changes (Figure 8.4d). This is something that needs to be fixed in following chapters adjusting the electrical converter controlling battery current as well as its weight function.

- Overheating in the water accumulator in the case of the simplified model (Figure 6.2e) forces the system to expel heat as waste (Figure 6.2i). This does not happen in the case of the main model, where the water temperature remains stable (Figure 8.4e) and extra heat is not produced in consequence (Figure 8.4i). However, extra heat coming from the transformation of part of the electrical power into heat is needed for the main model (Figure 8.4f), 0 in the case of the simplified model (Figure 6.2f).

- External electrical power coming from the grid is needed in the case of the main model (Figure 8.4g), but not in the case of the simplified model (Figure 6.2g).

6.5.2.3 Main model's October results

Additionally, extra escenarios have been simulated in the case of the main model. For instance, results for a day of October can be seen in Figure 6.10.

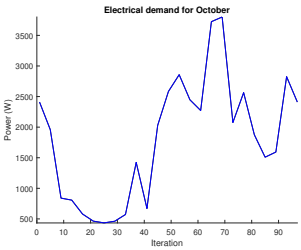

(a) Electrical demand on a day of October

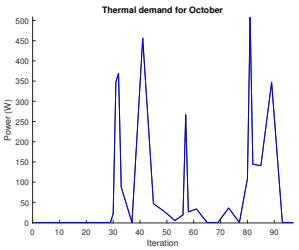

(b) Thermal demand on a day of October

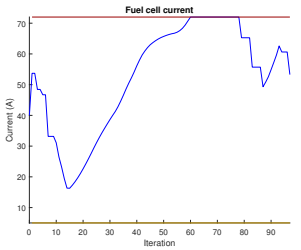

(c) Fuel cell current on a day of October

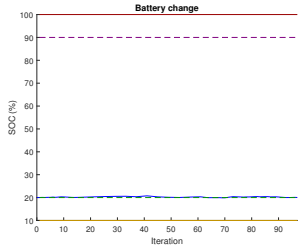

(d) Electrical battery state of charge on a day of October

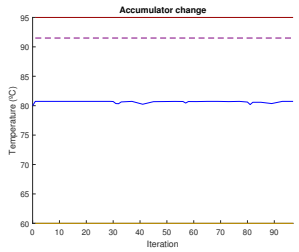

(e) Water accumulator temperature on a day of October

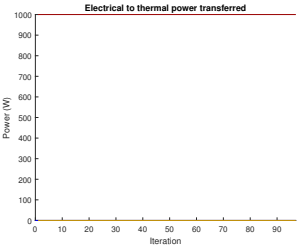

(f) Electrical power transferred to the thermal system on a day of October

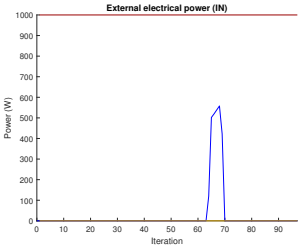

(g) Electrical power supplied by the grid on a day of October

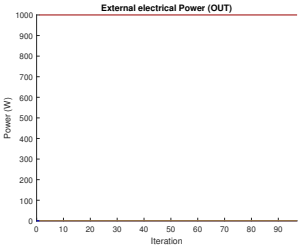

(h) Electrical power supplied to the grid on a day of October

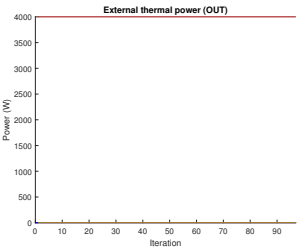

(i) Thermal power extracted as waste on a day of October

Figure 6.10: Results for a day of October (200 kg of water in the accumulator)

Due to similar whether conditions, April (first month of Spring) and October (first month of Autumn) have very similar results in all cases. For example, fuel cell current evolution is very similar (Figures 8.4c and 6.10c), as well as constant values in battery state of charge (Figures 8.4d and 6.10d) and the extra peak of electrical power from the grid needed (Figures 8.4g and 6.10g). In the following chapter, a tuning procedure prioritising some control objectives above others is presented, previously to integrating the system elements well adjusted and get final results in the final chapter.

Chapter 7

System objectives' tuning using Pareto fronts

No person can disobey reason, without giving up his claim to be a rational creature.

From *Gulliver's Travels*, by Jonathan Swift

In previous chapters, several control objectives combined in a single objective function have been presented. These objectives have been weighted to carry on simulations, but a more precise tuning is needed to ensure the system's performance. For doing so, a tuning strategy based on the concept of Pareto fronts is presented in this chapter. This approach has been tackled without taking into consideration electrolyser and solar panel, as their operation is not controlled by the optimisation problem carried on by the MPC.

7.1 System objectives' selection

Looking at results obtained in simulation results shown in the previous chapter, among objectives presented in equations (6.1) to (6.11), some of them can be considered more important, some of them can be combined and others them neglected to avoid redundancies. The following remarks can be done:

- Current and its variation are clearly related. Minimising one can undermine the minimisation of the other.

- Soft constraints in the ancillary systems (grid and water accumulator) should only be violated when necessary and just for brief periods.
- Ancillary systems (grid, battery and accumulator) are activated using binary variables, whose switching must be done just when it's necessary.

Considering this analysis, three subfunctions can be selected to proceed with the tuning process. These three subfunctions need to be weighted in a way that favours the whole objective function minimisation. This is done using an approach based on the concept of Pareto fronts, explained in the following section.

7.2 Pareto fronts: theoretical approach

The concept of Pareto front is one used in optimisation problems to define a set of solutions of an optimisation problem that satisfies minimum conditions [21]. They are defined in the space defined by functions (or subfunctions) $f_i(\overrightarrow{x})$ to be weighted (using weight functions w_i) to build a global objective function $f(\vec{x})$. The generic case is the following one:

$$f(\vec{x}) = \sum_{i=1}^{N} w_i f_i(\vec{x})$$
$$\sum_{i=1}^{N} w_i = 1 \tag{7.1}$$

A Pareto front is a trade-off surface of solutions obtained using the sorting rule based on the definition of domination. Let us imagine a problem with two objective functions with the following structure

- Minimize f_1 and f_2
- Under constraints $\overrightarrow{g}(\overrightarrow{x}) \leq 0$ and $\overrightarrow{h}(\overrightarrow{x}) = 0$

Knowing this, we denote:

- S as the set of values of the pair $(f_1(\overrightarrow{x}), f_2(\overrightarrow{x}))$ when $\overrightarrow{x}$ respects the constraints $\overrightarrow{g}(\overrightarrow{x}) \leq 0$ and $\overrightarrow{h}(\overrightarrow{x}) = 0$.

- P as the trade-off surface.

The concept of domination states that $(f_1(\overrightarrow{x}), f_2(\overrightarrow{x})) \leq (f_1(\overrightarrow{\hat{x}}), f_2(\overrightarrow{\hat{x}}))$, meaning that $f_1(\overrightarrow{x}) \leq f_1(\overrightarrow{\hat{x}})$ & $f_2(\overrightarrow{x}) \leq f_2(\overrightarrow{\hat{x}})$ but $(f_1(\overrightarrow{x}), f_2(\overrightarrow{x})) \neq (f_1(\overrightarrow{\hat{x}}), f_2(\overrightarrow{\hat{x}}))$. Pareto front P is formed by all $\overrightarrow{x^*}$ so that there is no $\overrightarrow{x}$ matching condition $(f_1(\overrightarrow{x}), f_2(\overrightarrow{x^*})) \leq (f_1(\overrightarrow{x}), f_2(\overrightarrow{x^*}))$. The schematic representation is the one seen in Figure 7.1.

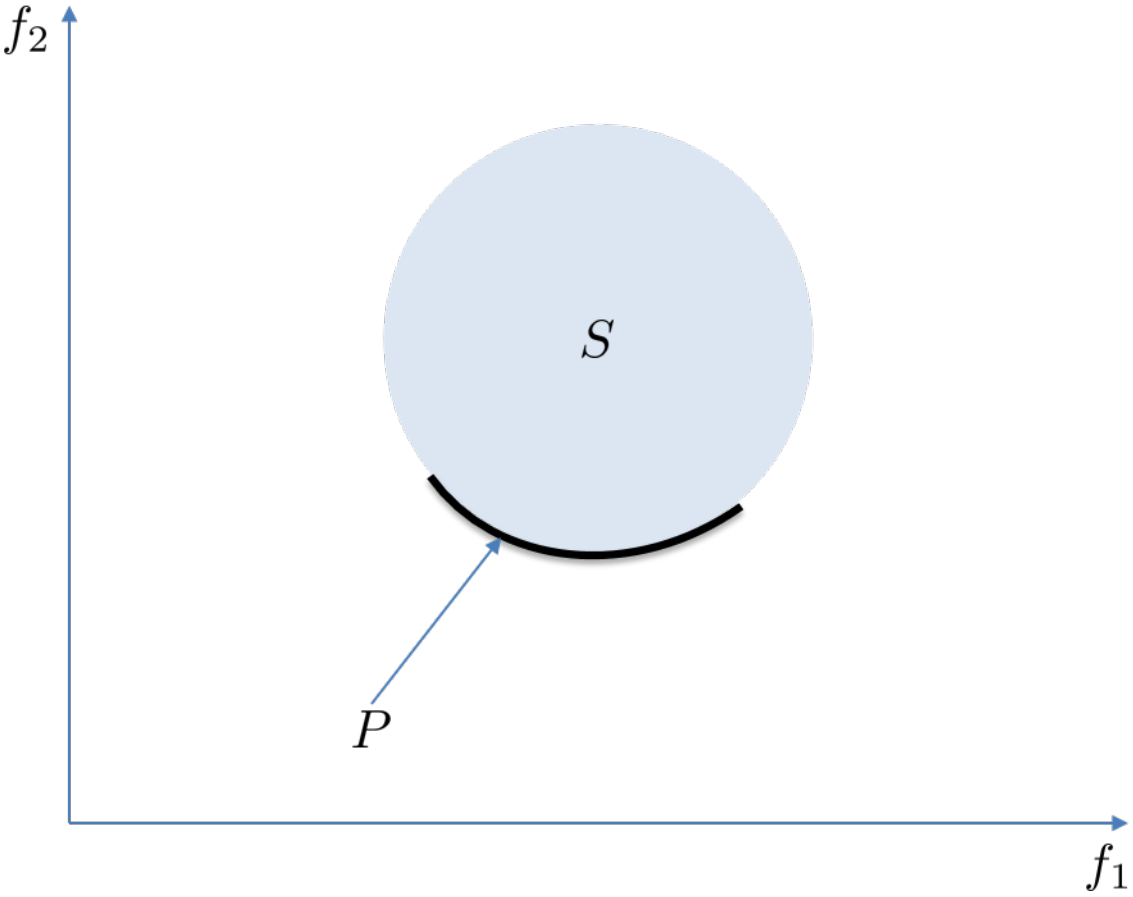

Figure 7.1: Scheme of a Pareto front P of a set S

7.2.1 Convexity

A set S is convex if, given two distinct points in this set, the segment which links these two points lies in the set S. This is illustrated in Figures 7.2a and 7.2b.

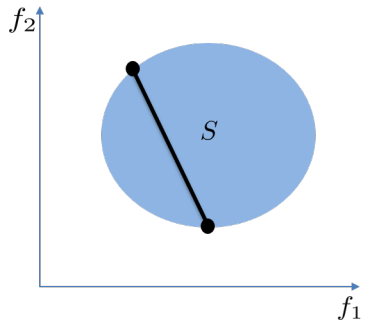

(a) A convex set

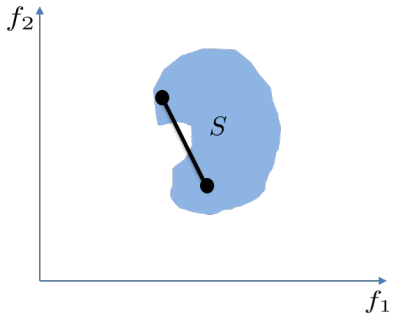

(b) A nonconvex set

Figure 7.2: Examples of convex and nonconvex sets in the space of functions f_1 and f_2

In the case of a multiobjective problem with a convex solution set (2 objective functions), common sets have the following shapes:

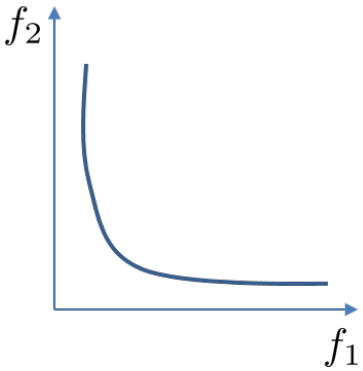

(a) Minimising f_1 and minimising f_2

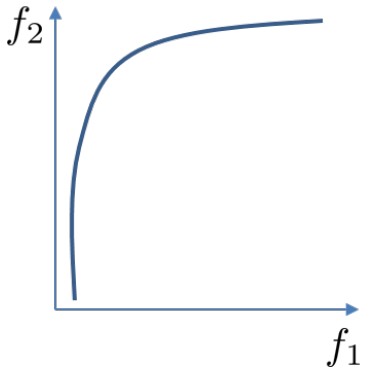

(b) Minimising f_1 and maximising f_2

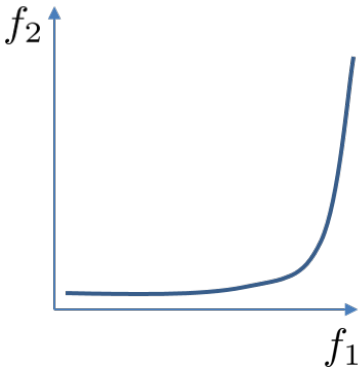

(c) Maximising f_1 and minimising f_2

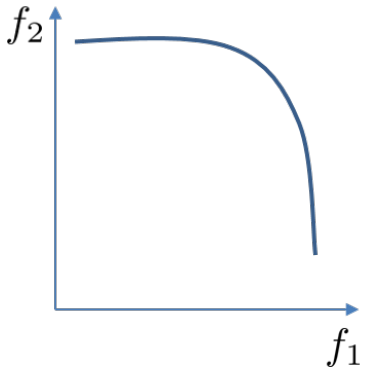

(d) Maximising f_1 and maximising f_2

Figure 7.3: Different combinations when minimising and maximising functions f_1 and f_2

7.2.2 Ideal point and Nadir point

In the space of functions f_1 and f_2, the following two points must be highlighted and defined:

- **Ideal point**: point whose coordinates are obtained by minimising each objective function separately.
- **Nadir point**: point whose coordinates correspond to the worst values obtained for each objective function when the solution set is restricted to the trade-off surface.

These two points are illustrated in Figure 7.4.

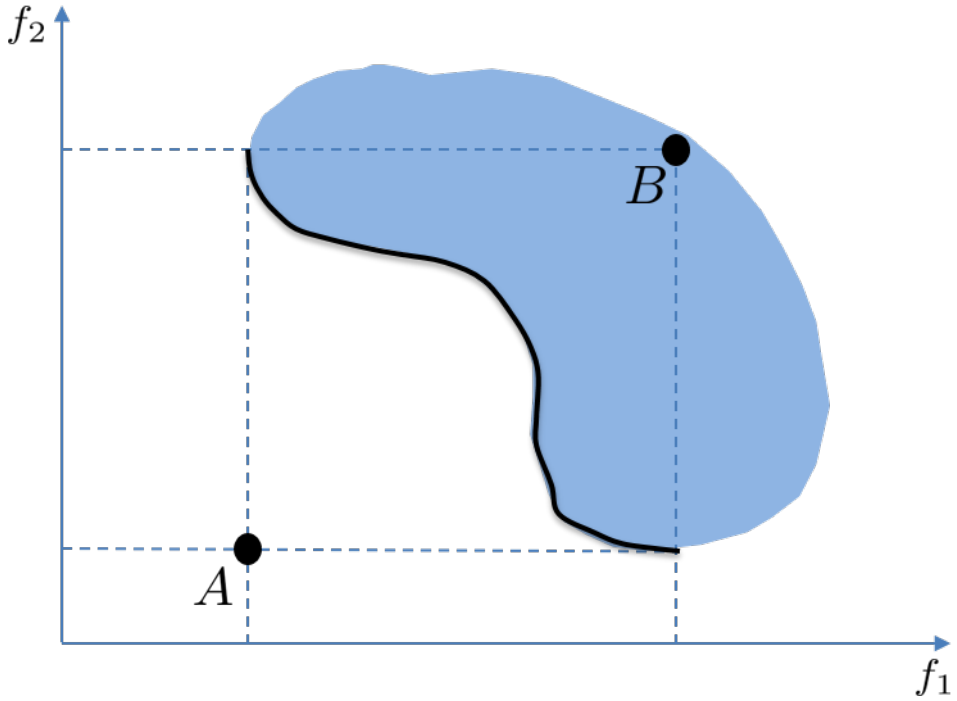

Figure 7.4: Ideal point A and Nadir point B of a certain set (in blue) with its Pareto front (in black)

7.3 Aproximation of a Pareto front for the case studied

In the case of the system studied, the three objective subfunctions considered are the ones mentioned earlier:

- Current plus its variation f_{C+CV}.
- Soft constraints in the ancillary systems f_{SC}.
- Security elements (ancillary systems) f_{SE}.

The aim of this procedure is selecting the weight functions corresponding to these three subfunctions to build the final objective function. For doing so, an approximation of the Pareto front in the space of these three subfunctions is defined. To do so, the following procedure is followed:

1. All three subfunctions f_{C+CV}, f_{SC} and f_{SE} are minimised and the set of variables minimising them u_k^* and e_k^* is obtained.
2. These minimising variables obtained for each subfunction f_{C+CV}, f_{SC} and f_{SE} are then evaluated in the other two subfunctions.
3. The resulting three groups of three coordinates each are depicted in a plot in the subfunctions' space.
4. A plane formed by all three points is defined as an approximation of the Pareto front.
5. Several scenarios with different combinations of weight functions W_{C+CV}, W_{SC} and W_{SE} are simulated and plotted in the same graph.
6. New points close to the plane are selected while checking those ones offering minimum objective function variables.
7. Several iterations choosing new points are carried on trying to see the pattern of minimisation when each weight function is varied.
8. Simulation results are checked to discard those not fulfilling system requirements not present in these subfunctions.

In the case of the scenario of January, plots with all these elements are the ones seen in Figure 7.5.

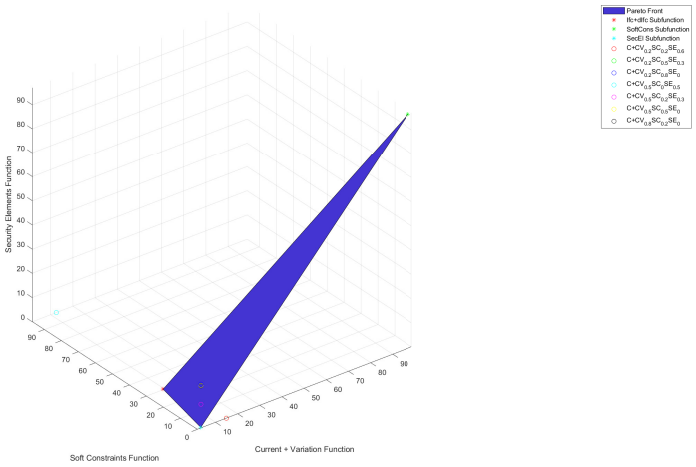

Figure 7.5: Pareto front and points for different weight functions in the subfunction space (January, 7 points)

It can be seen that one case, the one with weight function $W_{SC} = 0$ is not even close and must be discarded. The other points can be classified according to their position as:

- Points with weight function $W_{SE} = 0$ are almost identical and a bit far away from the plane compared to the other ones.
- Point with $(W_{C+CV}, W_{SC}, W_{SE}) = (0.5, 0.2, 0.3)$ is just above the plane.
- Points with $(W_{C+CV}, W_{SC}, W_{SE}) = (0.2, 0.2, 0.6)$ and $(W_{C+CV}, W_{SC}, W_{SE}) = (0.2, 0.5, 0.3)$ are just under the plane and almost identical.

This means an attempt to find points between those just below and just above the plane is the next step to be followed. For doing so, two extra points corresponding to weight functions $(W_{C+CV}, W_{SC}, W_{SE}) = (0.35, 0.2, 0.45)$ and $(W_{C+CV}, W_{SC}, W_{SE}) = (0.35, 0.5, 0.15)$. These are added to the previous plot and can be seen in Figure 7.6.

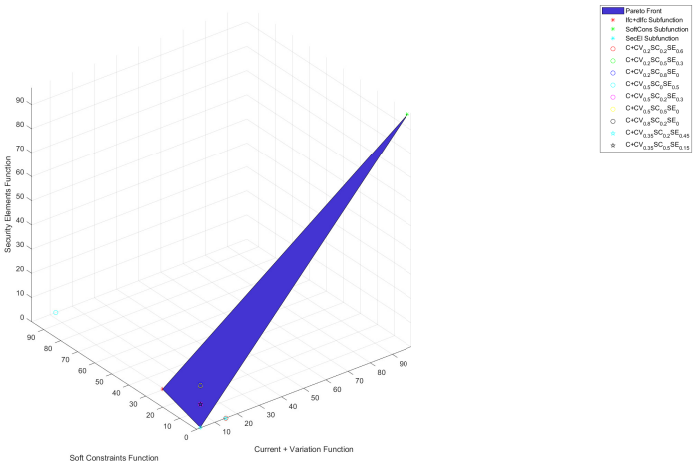

Figure 7.6: Pareto front and points for different weight functions in the subfunction space (January, 9 points)

In Figure 7.6 it can be seen that these two extra points almost overlap with the ones obtained previously: the one with $(W_{C+CV}, W_{SC}, W_{SE}) = (0.35, 0.2, 0.45)$ is almost identical to the one just below the plane and the one with $(W_{C+CV}, W_{SC}, W_{SE}) = (0.35, 0.5, 0.15)$ almost coincides with the one just above the plane. A final attempt to find different points closer to the plane is done adding two points with weight functions $(W_{C+CV}, W_{SC}, W_{SE}) = (0.35, 0.35, 0.3)$ and $(W_{C+CV}, W_{SC}, W_{SE}) = (0.35, 0.05, 0.6)$ and they are added to the plot, as seen in Figure 7.7.

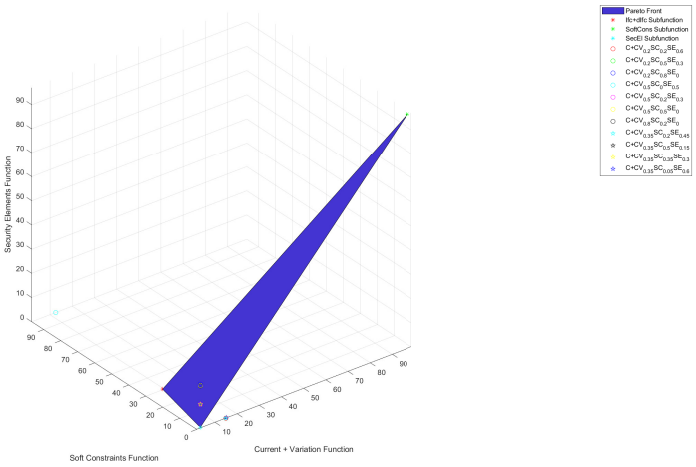

Figure 7.7: Pareto front and points for different weight functions in the subfunction space (January, 11 points)

It can be seen that these final points also overlap with the ones just above and just below the plane, meaning that finding points between those two fixed positions just above and just below seems difficult due to system nonlinearities, even if weight functions are interpolated several times as done in the previous two steps. In order to decide which set of weight functions is good enough, an analysis of their objective functions and the simulation results in general is needed. This will be done after exploring other scenarios (other months for simulation). For instance, in the case of April, similar points to the ones already analyse are plotted (discarding the one with $W_{SC} = 0$, based on the previous analysis based on January results). All these, together with the slightly different plane are plotted in Figure 7.8.

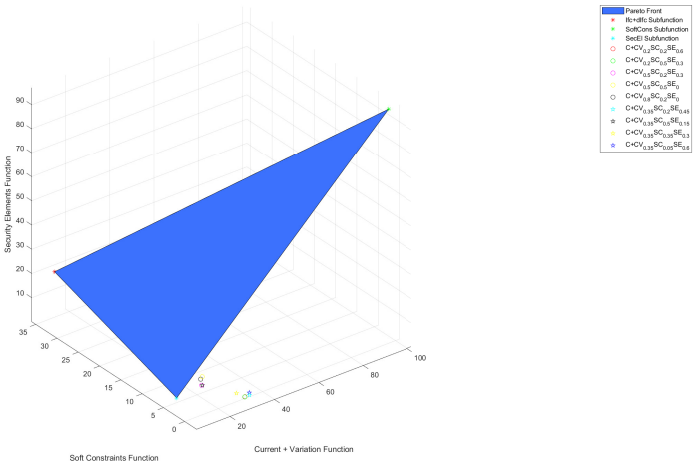

Figure 7.8: Pareto front and points for different weight functions in the subfunction space (April, 9 points)

From Figure 7.8 it can be extracted that general behaviour of weight functions is similar to the one obtained for January (once the point with $W_{SC} = 0$ has been discarded). For this reason, results for both months need to be carefully analysed using objective function's values and simulation values. In the case of January, objective functions have the following values for different the weight functions studied:

- $(W_{C+CV}, W_{SC}, W_{SE}) = (0.35, 0.5, 0.15)$ has $f = 2.6481$, but does not apply the energy transfer variable as needed in terms of energy efficiency.
- $(W_{C+CV}, W_{SC}, W_{SE}) = (0.2, 0.2, 0.6)$ has $f = 2.9678$ and $(W_{C+CV}, W_{SC}, W_{SE}) = (0.2, 0.5, 0.3)$ has $f = 2.9710$. Both have fuel cell current as the main energy source, as expected. These would be the ideal points.
- $(W_{C+CV}, W_{SC}, W_{SE}) = (0.35, 0.35, 0.3)$ has $f = 4.1174$ and $(W_{C+CV}, W_{SC}, W_{SE}) = (0.5, 0.2, 0.3)$ has $f = 4.6225$. Both use too much energy from the grid and transferred from the electrical part to the thermal part of the system.
- $(W_{C+CV}, W_{SC}, W_{SE}) = (0.35, 0.2, 0.45)$ has $f = 5.1701$ and $(W_{C+CV}, W_{SC}, W_{SE}) = (0.35, 0.05, 0.6)$ has $f = 5.3651$. Both are similar to the ideal ones but have objective functions much greater.

- $(W_{C+CV}, W_{SC}, W_{SE}) = (0.5, 0, 0.5)$ has $f = 6.2656$. This one is really bad and, in addition, energy transferred from the electrical part to the thermal one is to high.

The two ideal points detected have a similar behaviour in terms of fuel cell current, as well as objective function. To proceed with the analysis to select the best combination of weight functions with the values of objective functions in the April scenario:

- $(W_{C+CV}, W_{SC}, W_{SE}) = (0.35, 0.5, 0.15)$ has $f = 6.3300$ and $(W_{C+CV}, W_{SC}, W_{SE}) = (0.5, 0.5, 0)$ has $f = 6.4260$. These are the ones with minimum objective function, but switching between energy sources (grid, energy transferred, etc.) is constant and abrupt, as their constraints are not taken into consideration.

- $(W_{C+CV}, W_{SC}, W_{SE}) = (0.2, 0.5, 0.3)$ has $f = 6.6108$ and $(W_{C+CV}, W_{SC}, W_{SE}) = (0.2, 0.2, 0.6)$ has $f = 6.8186$. These ones are the best ones and have the fuel cell current as the main energy source as expected.

- $(W_{C+CV}, W_{SC}, W_{SE}) = (0.5, 0.2, 0.3)$ has $f = 10.0703$. Its grid energy consumption is too high and its fuel cell current variation is too high.

- $(W_{C+CV}, W_{SC}, W_{SE}) = (0.8, 0.2, 0)$ has $f = 10.2161$. Security elements constraint is not taken into consideration, with constant switching between energy sources as a consequence.

- $(W_{C+CV}, W_{SC}, W_{SE}) = (0.35, 0.35, 0.3)$ has $f = 10.9625$. Its grid energy consumption is too high.

- $(W_{C+CV}, W_{SC}, W_{SE}) = (0.35, 0.2, 0.45)$ has $f = 12.2827$ and $(W_{C+CV}, W_{SC}, W_{SE}) = (0.35, 0.05, 0.6)$ has $f = 12.6828$. Their fuel cell current variation is too high.

Once these analysis has been done, it can be stated that combinations of weights $(W_{C+CV}, W_{SC}, W_{SE}) = (0.2, 0.2, 0.6)$ and $(W_{C+CV}, W_{SC}, W_{SE}) = (0.2, 0.5, 0.3)$ are almost the best ones in both scenarios (January and April). However, in the case of January they have an almost identical objective function value. For this reason, the best one for April, $(W_{C+CV}, W_{SC}, W_{SE}) = (0.2, 0.5, 0.3)$, is the one selected as the most adequate.

Finally a final adjust needs to be done regarding the importance given to fuel cell current minimisation compared to its variation. In the analysis done, both current and its variation have been considered part of the same subfunction $f_{C+CV} = W_C f_C + W_{CV} f_{CV}$ to ensure ideal points used to form the plane in the subfunction space has the desired coordinates from a mathematical perspective. Once the global weight function has been decided as $W_{C+CV} = 0.2$ with the same internal weight functions $W_C = W_{CV} = 0.1$, a manual tuning can be done to fulfil both minimisations better. For doing so, the analysis is done in the case of April, provided that January's fuel cell current is almost flat and does not show much differences for different values of $W_C, W_{CV} \in [0, 0.2]$. In the case of April, the following values are analysed looking at the current shape along time:

- $W_C = 0.04$ and $W_{CV} = 0.16$ has $f = 3.4928$. Its current is too flat followed by sudden variations too sudden, affecting fuel cell degradation (Figure 7.9).
- $W_C = 0.06$ and $W_{CV} = 0.14$ has $f = 4.2406$. It represents the best combination, with good trade-off between current minimisation and its variation based on results (Figure 7.10).
- $W_C = 0.08$ and $W_{CV} = 0.12$ has $f = 5.6213$. It offers worst performance than the previous two cases when results are analysed (Figure 7.11).
- $W_C = 0.14$ and $W_{CV} = 0.06$ has $f = 9.7631$. It presents abrupt changes of up to 40 A, which is really bad for degradation purposes (Figure 7.12).

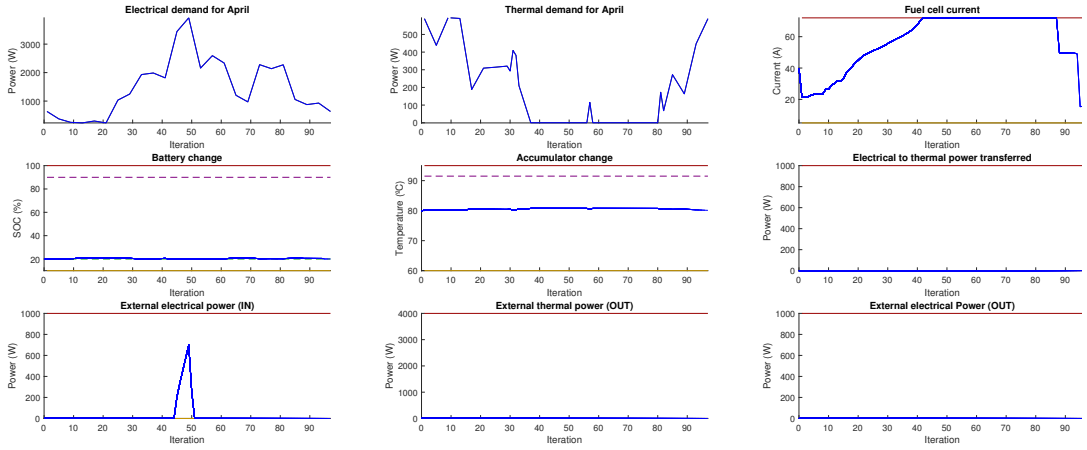

Figure 7.9: System variables evolution for an average April day ($W_C = 0.04$ and $W_{CV} = 0.16$

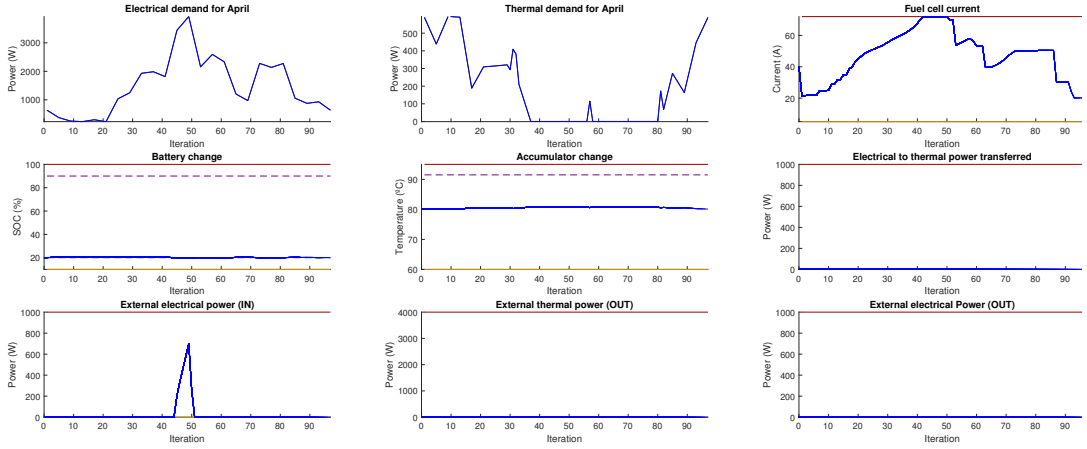

Figure 7.10: System variables evolution for an average April day ($W_C = 0.06$ and $W_{CV} = 0.14$

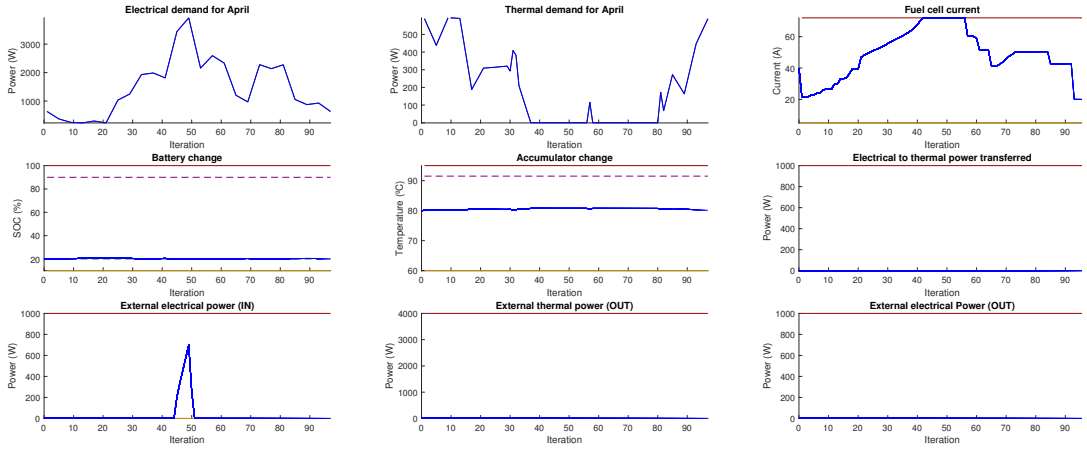

Figure 7.11: System variables evolution for an average April day ($W_C = 0.08$ and $W_{CV} = 0.12$

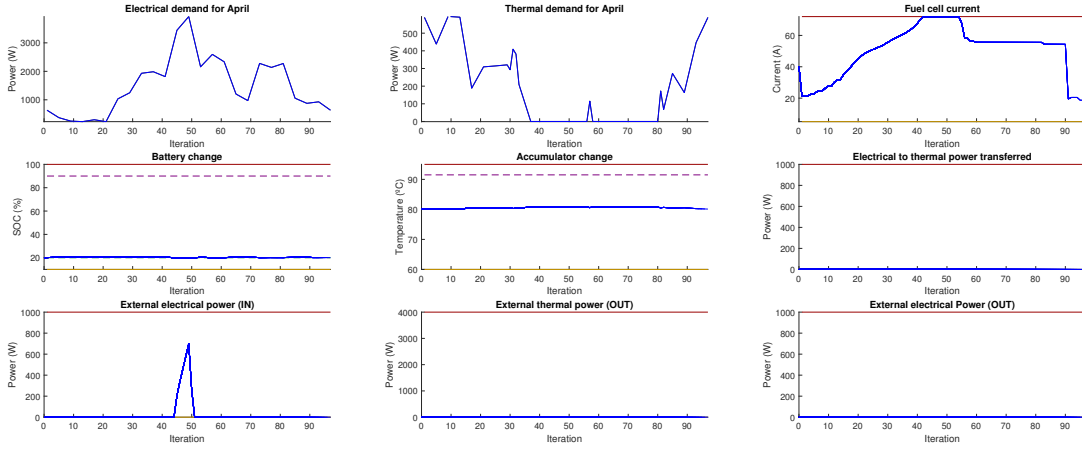

Figure 7.12: System variables evolution for an average April day ($W_C = 0.14$ and $W_{CV} = 0.06$

When these results are compared with the case of January, they all have almost the same behaviour, no matter which weight functions in the range $W_C, W_{CV} \in [0, 0.2]$ are selected. Consequently, the final weight functions to be selected for both scenarios are $W_C = 0.06$, $W_{CV} = 0.14$, $W_{SC} = 0.5$ and $W_{SE} = 0.3$. These are the ones to be used to obtain the thesis' final results in the following chapter.

Chapter 8

Results and discussion

And my soul from out that shadow that lies floating on the floor

Shall be lifted—nevermore!

From *The Raven*, by Edgar Allan Poe

Once the whole system has been integrated in the simulation, final results can be computed. These results include all elements already presented in chapter 4:

- HT-PEMFC
- Electrical battery
- Water accumulator
- Electrolyser
- Solar panel
- Thermal and electrical loads

Prediction is included considering that the demand is known 5 hours in advance, as this is the typical knowledge one has of residential consumption based on daily habits. In the following sections, final simulations including a final adjustment of some element's dimensions are presented.

8.1 January results

With battery dimensions as established along the thesis (160 Ah capacity), results for a typical day of January are obtained and shown in Figure 8.1:

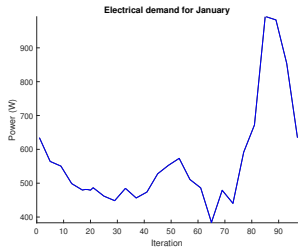

(a) Electrical demand on a day of January (complete model)

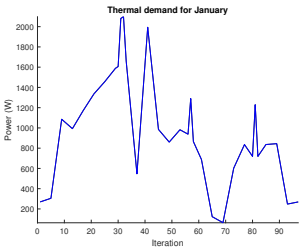

(b) Thermal demand on a day of January (complete model)

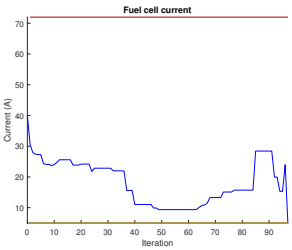

(c) Fuel cell current on a day of January (complete model)

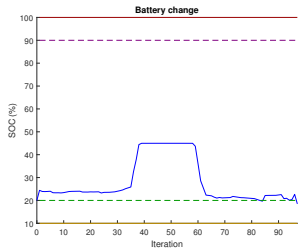

(d) Electrical battery state of charge on a day of January (complete model)

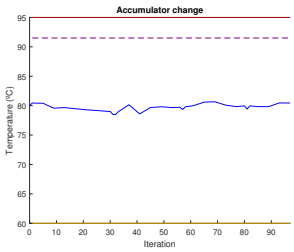

(e) Water accumulator temperature on a day of January (complete model)

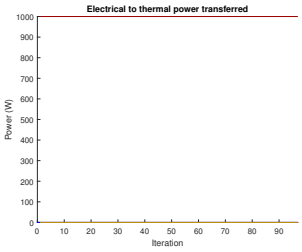

(f) Electrical power transferred to the thermal system on a day of January (complete model)

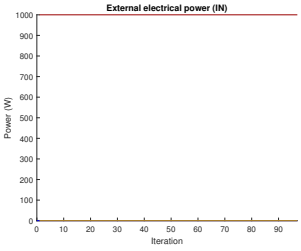

(g) Electrical power supplied by the grid on a day of January (complete model)

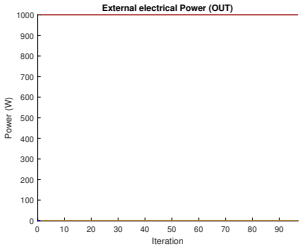

(h) Electrical power supplied to the grid on a day of January (complete model)

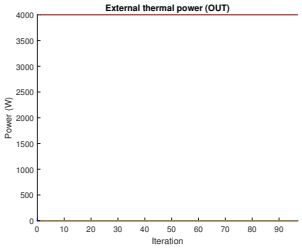

(i) Thermal power extracted as waste on a day of January (complete model)

Figure 8.1: Complete model's results for a day of January

It can be seen that battery's SOC (state of charge) does not reach top soft constraints. This implies that a smaller, and thus cheaper, battery capacity could be selected. A study with a couple of simulations with these different battery examples

are consequently plotted.

8.1.1 Battery dimensioning for January

If battery capacity is halved (80 Ah), the following results are obtained (Figure 8.2):

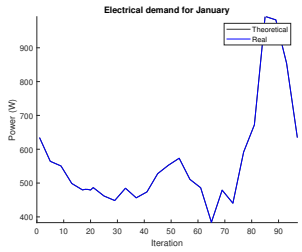

(a) Electrical demand on a day of January (battery capacity of 80 Ah)

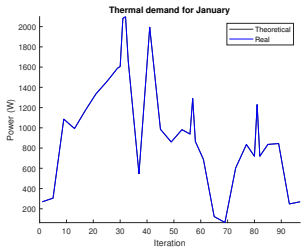

(b) Thermal demand on a day of January (battery capacity of 80 Ah)

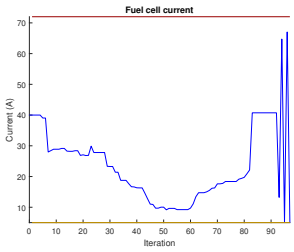

(c) Fuel cell current on a day of January (battery capacity of 80 Ah)

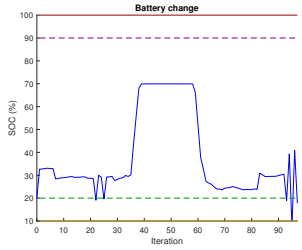

(d) Electrical battery state of charge on a day of January (battery capacity of 80 Ah)

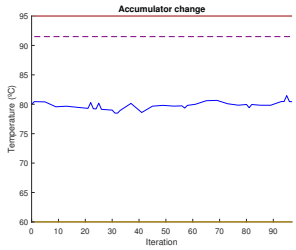

(e) Water accumulator temperature on a day of January (battery capacity of 80 Ah)

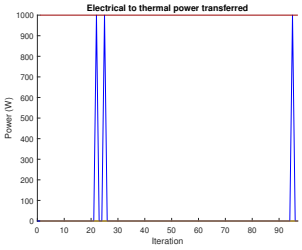

(f) Electrical power transferred to the thermal system on a day of January (battery capacity of 80 Ah)

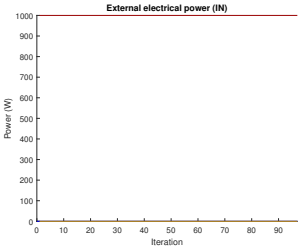

(g) Electrical power supplied by the grid on a day of January (battery capacity of 80 Ah)

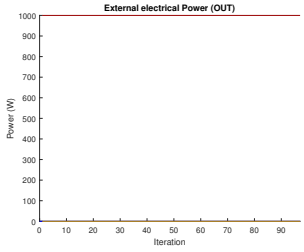

(h) Electrical power supplied to the grid on a day of January (battery capacity of 80 Ah)

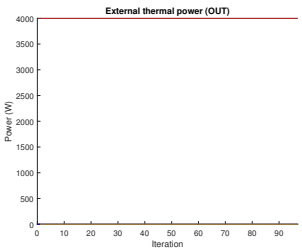

(i) Thermal power extracted as waste on a day of January (battery capacity of 80 Ah)

Figure 8.2: Complete model's results for a day of January (battery capacity of 80 Ah)

After halving battery capacity, certain emergency elements to match demands have

been triggered. For this reason, a value between the first one imposed (160 Ah) and this one (80 Ah) should be explored.Consequently, the same simulation is done with a battery capacity with an intermediate value of 107 Ah. Results for this case can be seen in Figure 8.3

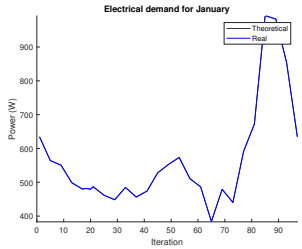

(a) Electrical demand on a day of January (battery capacity of 80 Ah)

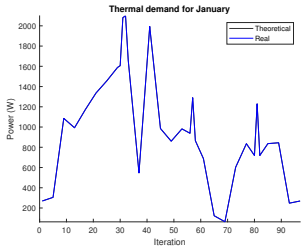

(b) Thermal demand on a day of January (battery capacity of 107 Ah)

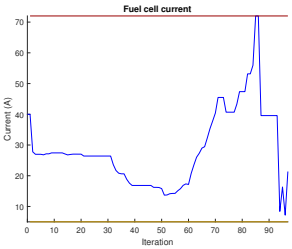

(c) Fuel cell current on a day of January (battery capacity of 80 Ah)

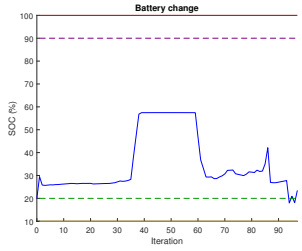

(d) Electrical battery state of charge on a day of January (battery capacity of 107 Ah)

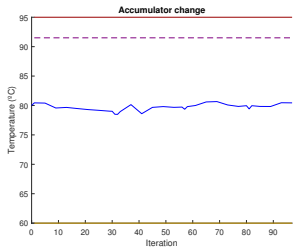

(e) Water accumulator temperature on a day of January (battery capacity of 107 Ah)

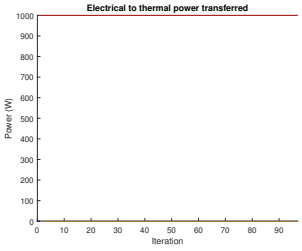

(f) Electrical power transferred to the thermal system on a day of January (battery capacity of 107 Ah)

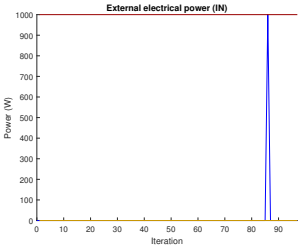

(g) Electrical power supplied by the grid on a day of January (battery capacity of 107 Ah)

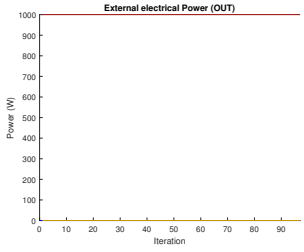

(h) Electrical power supplied to the grid on a day of January (battery capacity of 107 Ah)

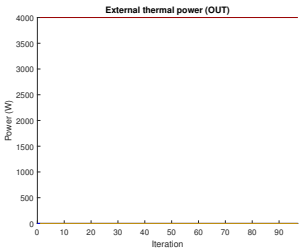

(i) Thermal power extracted as waste on a day of January (battery capacity of 107 Ah)

Figure 8.3: Complete model's results for a day of January (battery capacity of 107 Ah)

This means that 107 Ah would correspond to a good battery capacity. It can be seen that battery works properly, thus helping fuel cell overcome demand variations. Fuel cell

current is flat enough, proving that degradations during winter is mitigated. It is true that a punctual connection to grid arises, while results for first value of battery capacity (Figure 8.1) require a bigger and more expensive battery, but less grid-depending. After the same analysis for April is done, a conclusion will be reached. to select the definitive battery capacity.

8.2 April results

A similar study is carried on for the case of a typical day of April. As done before, simulations with the initial battery capacity (160 Ah) are carried on. These simulation's results are shown on Figure 8.4:

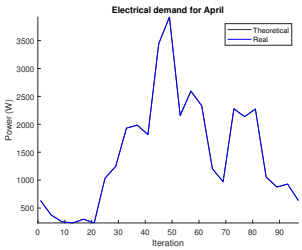

(a) Electrical demand on a day of April (battery capacity of 160 Ah)

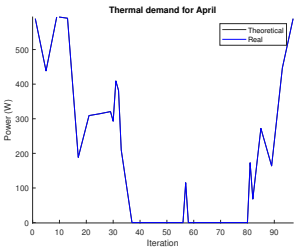

(b) Thermal demand on a day of April (battery capacity of 160 Ah)

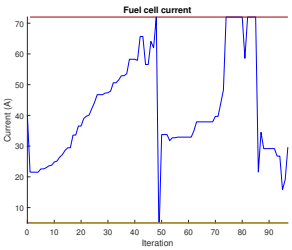

(c) Fuel cell current on a day of April (battery capacity of 160 Ah)

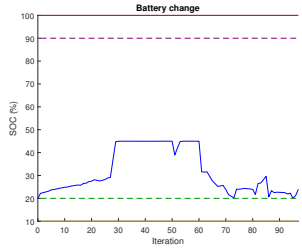

(d) Electrical battery state of charge on a day of April (battery capacity of 160 Ah)

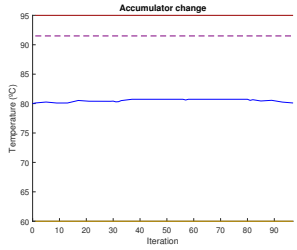

(e) Water accumulator temperature on a day of April (battery capacity of 160 Ah)

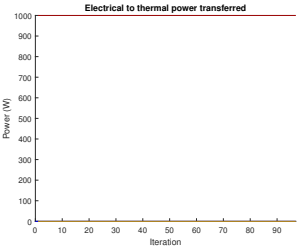

(f) Electrical power transferred to the thermal system on a day of April (battery capacity of 160 Ah)

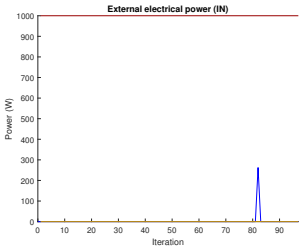

(g) Electrical power supplied by the grid on a day of April (battery capacity of 160 Ah)

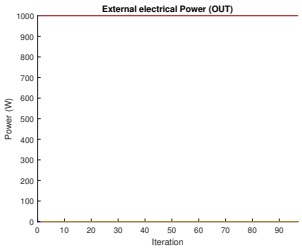

(h) Electrical power supplied to the grid on a day of April (battery capacity of 160 Ah)

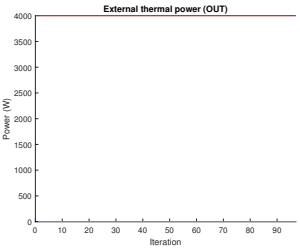

(i) Thermal power extracted as waste on a day of April (battery capacity of 160 Ah)

Figure 8.4: Complete model's results for a day of April (battery capacity of 160 Ah)

Results seem reliable enough, as emergency systems such as grid connection and thermal energy produced transforming electrical energy are hardly ever needed. Fuel cell current is more variable that January results, so a highest capacity for the battery is explored to look for possible improvements.

8.2.1 Battery dimensioning for April

In order to see if a cheaper, i.e. with lower capacity, battery can be used, a similar simulation is done using a battery with half its capacity (80 Ah). These results can be seen in Figure 8.5:

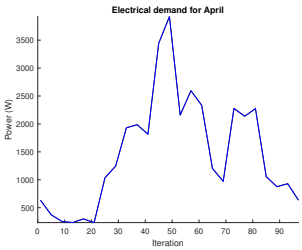

(a) Electrical demand on a day of April (battery capacity of 80 Ah)

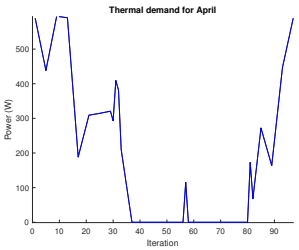

(b) Thermal demand on a day of April (battery capacity of 80 Ah)

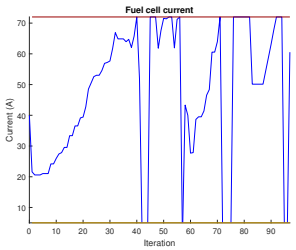

(c) Fuel cell current on a day of April (battery capacity of 80 Ah)

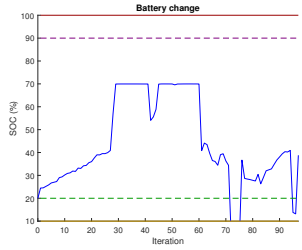

(d) Electrical battery state of charge on a day of April (battery capacity of 80 Ah)

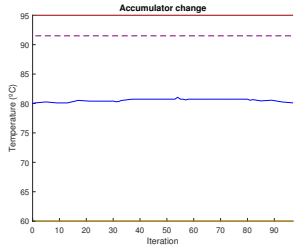

(e) Water accumulator temperature on a day of April (battery capacity of 80 Ah)

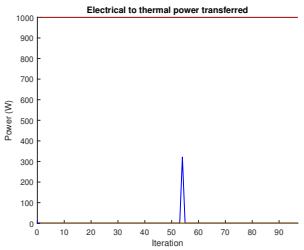

(f) Electrical power transferred to the thermal system on a day of April (battery capacity of 80 Ah)

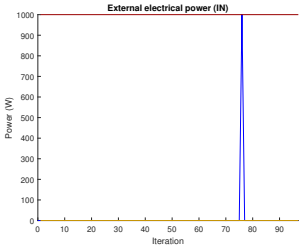

(g) Electrical power supplied by the grid on a day of April (battery capacity of 80 Ah)

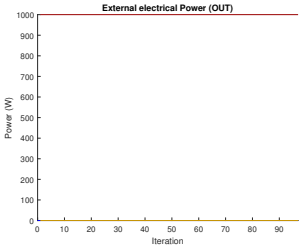

(h) Electrical power supplied to the grid on a day of April (battery capacity of 80 Ah)

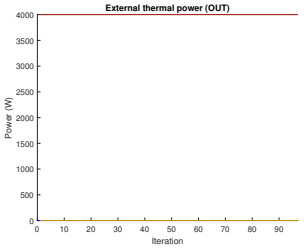

(i) Thermal power extracted as waste on a day of April (battery capacity of 80 Ah)

Figure 8.5: Complete model's results for a day of April (battery capacity of 80 Ah)

In this case, it can be seen that extra grid power is needed to match demand, and fuel cell currents presents too abrupt changes, which could be damaging for the fuel cell.

For this reason, the same conclusion is reached for both January and April scenarios: the initial 160 Ah battery is the one to be selected (Figures 8.1 and 8.4. To finish with results, a monitoring of hydrogen production by the electrolyser (propelled by the solar panel) is tackled in the next section.

8.3 Hydrogen production monitoring

To finish results, a simple monitoring procedure of the hydrogen produced by the electrolyser is done. As mentioned in previous chapters, solar panel and electrolyser are not included in the MPC strategy for simplicity. What has been done is dimensioning both elements so that simulations in the previous sections can be carried on while generating enough hydrogen for the fuel cell to work. The reason for doing so is avoiding using hydrogen coming from non-sustainable sources like gas reforming, usually sold in pressurised bottles. Results for the case of January presented before in Figure 8.1 correspond to an amount of hydrogen moles inside the hydrogen tank, the difference between the one produced and the one used by the fuel cell to make the system work, seen in Figure 8.6:

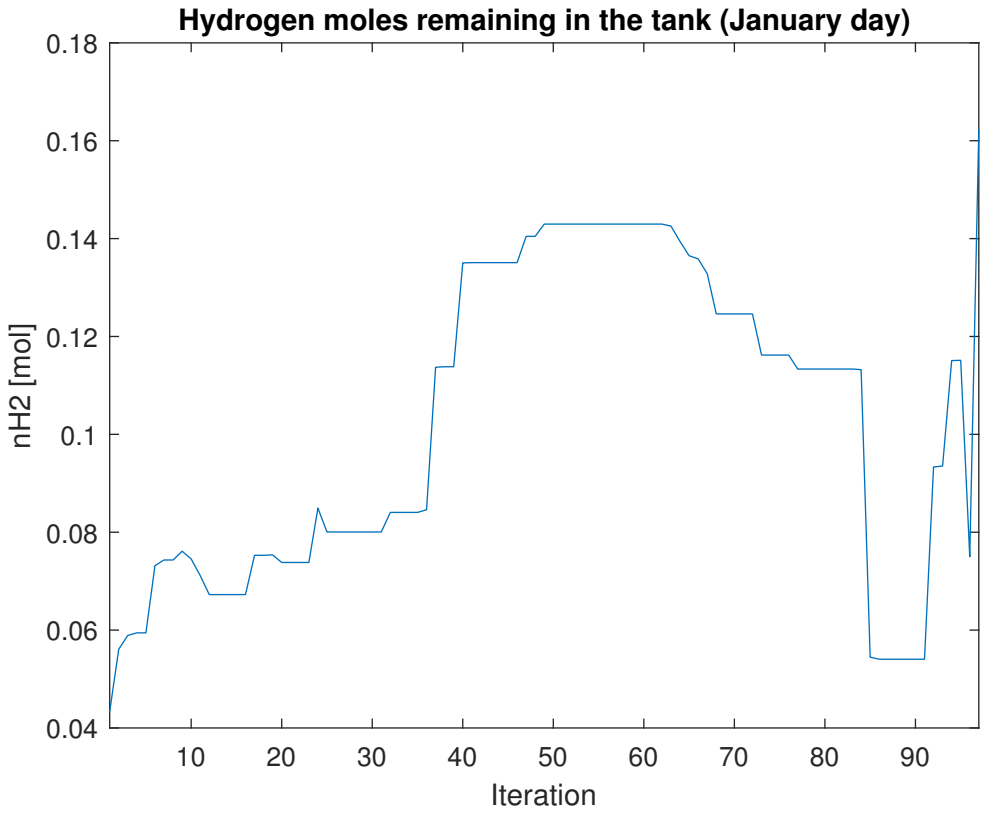

Figure 8.6: Hydrogen remaining in the tank during a typical day of January

It can be seen that enough hydrogen is produced to make the system work during January. This implies that the solar panel is able to generate enough power to make the electrolyser work properly. The same is done in the case of April, with the following results (Figure 8.7):

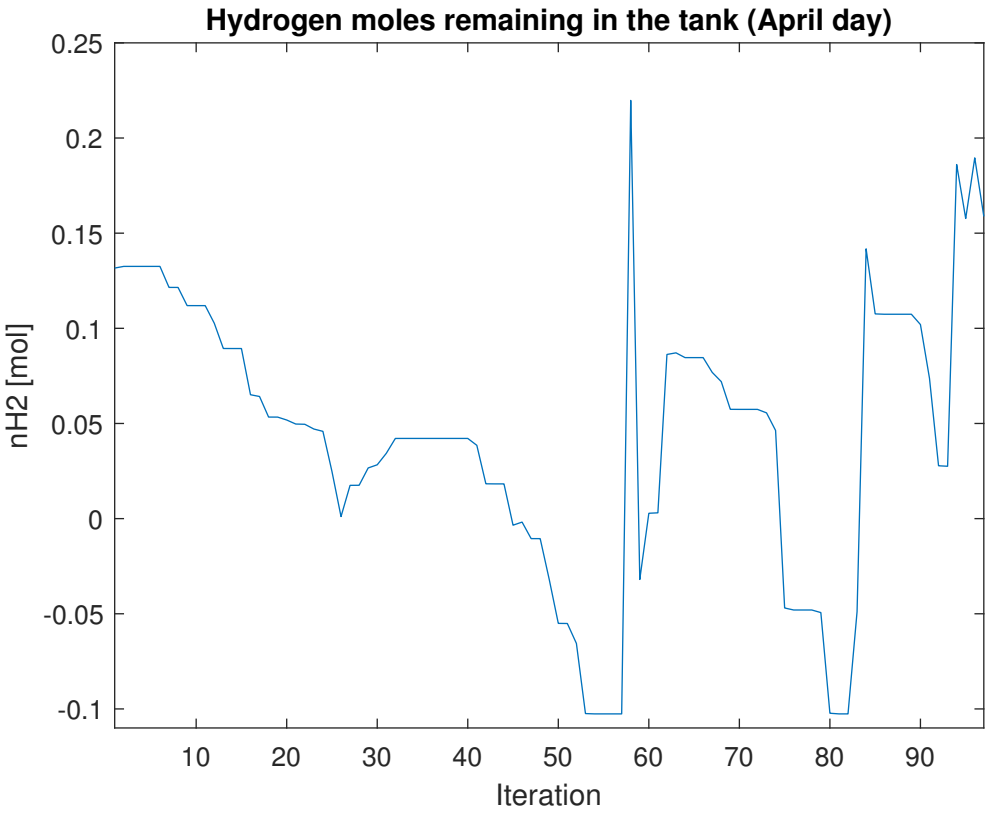

Figure 8.7: Hydrogen remaining in the tank during a typical day of April

As this simulation corresponds to a whole April day (from 0 a.m. to 0 a.m. the following day), the final value of hydrogen in the tank is fed would correspond to the first iteration of the following day. For this reason, as the minimum value along the day is -0.1 moles and the final one is 0.15 moles, the whole plot would be displaced 0.15 moles upwards and all values in the plot would end up being positive. Summarising, the amount of hydrogen generated by the electrolyser during an April day would be enough to make the fuel cell work and match demands for that day.

Chapter 9

Conclusions

The curfew tolls the knell of parting day

From *Elegy Written in a Country Churchyard*, by Thomas Gray

The global objective of designing and implementing suitable control strategies for a combined heat and power PEM fuel cell system for a prototypical house has been achieved. More specifically, the main two objectives envisaged have been fulfilled:

- *Energy efficiency*: energy losses have been mitigated, external grid consumption has been reduced to its minimum and emergency energy sources like producing heat from electrical energy conversion have been scarcely used.
- *Lifetime*: fuel cell degradation strategies have been successfully implemented to reduce abrupt fuel cell current variations.

To attain this global conclusion, the following solutions to step-by-step objectives proposed have been found:

1. A mathematical model to describe the fuel cell's behaviour has been defined. This model has been used to find operation points, but its low reliability around boundary conditions and difficulty to be manipulated and computed due to the high number of variables of the distributed system has made it a bad solution to include in the CHP system studied. For this reason, a simpler concentrated-parameters-based model has been implemented in the global CHP system to implement control.

2. A global simulation model of the CHP system with its components, i.e. HT-PEMFC, electrical battery, solar panel, electrolyser and water tanks for heating purposes have been defined and implemented in simulation. Local converters and controllers have been included for these elements.

3. A model predictive control strategy has been designed and implemented to control the CHP system. This has been done to match comfort specifications, enhance efficiency and reduce fuel cell degradation.

4. A control index has been designed. This index has the shape of an objective function including terms affecting the HT-PEMFC's degradation and its related variables such as cell voltage, current and temperature. This index also includes terms governing the activation of battery, water accumulator, grid and extra elements to be activated to ensure efficiency and sustainability.

5. A tuning Pareto-fronts-based procedure has been designed to stablish good values to prioritise some objectives of this index, working as objective function, above others.

6. Energy (heat and electrical power) profiles to be achieved by the CHP-HT-PEMFC in an specific house have been established. This has been done so that the defined comfort conditions, thermal and electrical, are met.

7. Simulation results using the proposed control strategy have reached those expected for equivalent housing facilities.

All these objectives have been fulfilled along the thesis, but there are still some challenges to be tackled so that research in this topic can be improved in the future.

9.1 Future Work

Once conclusions obtained along this thesis have been detailed, the following targets to be tackled remain:

1. A way to integrate complex distributed fuel cell models in online control strategies reducing computational effort should be implemented, thus getting to know more about fuel cell operation in a CHP system as the one proposed.

2. A complex thermal model of the house to better define comfort conditions and make the simulation closer to reality needs to be explored, using knowledge from others fields of study.

3. The global optimisation index should incorporate control of the hydrogen produced by that electrolyser making it intelligent enough so that the amount generated is the exact one, without overdimensioning the electrolyser. This would reduce economical cost related to this device.

4. Implementing the proposed control strategy in a prototypical house would be something good to be done in the future.

Bibliography

[1] Alireza Abbaspour, Arash Khalilnejad, and Zheng Chen. Robust adaptive neural network control for PEM fuel cell. *International Journal of Hydrogen Energy*, 41(44):20385–20395, 2016.

[2] Raj Kamal Abdul Rasheed and Siew Hwa Chan. Transient carbon monoxide poisoning kinetics during warm-up period of a high-temperature PEMFC - Physical model and parametric study. *Applied Energy*, 140:44–51, 2015.

[3] Raj Kamal Abdul Rasheed, Quan Liao, Zhang Caizhi, and Siew Hwa Chan. A review on modelling of high temperature proton exchange membrane fuel cells (HT-PEMFCs). *International Journal of Hydrogen Energy*, 42(5):3142–3165, 2017.

[4] Ahmad Abdallah Mohammad Aljabery, Hasan Mehrjerdi, Sajad Mahdavi, and Reza Hemmati. Multi carrier energy systems and energy hubs: Comprehensive review, survey and recommendations. *International Journal of Hydrogen Energy*, 46(46):23795–23814, 2021.

[5] Samuel Simon Araya, Ionela Florentina Grigoras, Fan Zhou, Soren Juhl Andreasen, and Soren Knudsen Kaer. Performance and endurance of a high temperature PEM fuel cell operated on methanol reformate. *International Journal of Hydrogen Energy*, 39(32):18343–18350, 2014.

[6] Suthida Authayanun, Mohamed Mamlouk, Keith Scott, and Amornchai Arpornwichanop. Comparison of high-temperature and low-temperature polymer electrolyte membrane fuel cell systems with glycerol reforming process for stationary applications. *Applied Energy*, 109:192–201, 2013.

[7] Félix Barreras, Antonio Lozano, Vicente Roda, Jorge Barroso, and Jesús Martín. Optimal design and operational tests of a high-temperature PEM fuel cell for a combined heat and power unit. *International Journal of Hydrogen Energy*, 39(10):5388–5398, 2014.

[8] Carles Batlle and Néstor Roqueiro. Balanced Model Order Reduction Method for Systems Depending on a Parameter. *IFAC-PapersOnLine*, 52(June 2019):412–417, 2019.

[9] Tomasz Bednarek and Georgios Tsotridis. Issues associated with modelling of proton exchange membrane fuel cell by computational fluid dynamics. *Journal of Power Sources*, 343:550–563, 2017.

[10] Hamed Beirami, Ali Zargar Shabestari, and Mohammad Mahdi Zerafat. Optimal PID plus fuzzy controller design for a PEM fuel cell air feed system using the self-adaptive differential evolution algorithm. *International Journal of Hydrogen Energy*, 40(30):9422–9434, 2015.

[11] P V Belyaev, Omsk State Technical, V S Mischenko, Omsk State Technical, D A Podberezkin, Omsk State Technical, and Omsk State Technical. Simulation modeling of proton exchange membrane fuel cells. *2016 Dynamics of Systems, Mechanisms and Machines (Dynamics)*, 1(3):1–5, 2016.

[12] A. Bergmann, D. Gerteisen, and T. Kurz. Modelling of CO poisoning and its dynamics in HTPEM fuel cells. *Fuel Cells*, 10(2):278–287, 2010.

[13] Fernando D Bianchi, Cristian Kunusch, Carlos Ocampo-Martinez, Senior Member, Ricardo S Sánchez-peña, and Senior Member. A Gain-Scheduled LPV Control for Oxygen Stoichiometry Regulation in PEM Fuel Cell Systems. *IEEE Transactions on Control Systems Technology*, 22(5):1837–1844, 2014.

[14] Adrian Bürger, Daniel Bull, Parantapa Sawant, Markus Bohlayer, Andreas Klotz, Daniel Beschütz, Angelika Altmann-Dieses, Marco Braun, and Moritz Diehl. Experimental operation of a solar-driven climate system with thermal energy storages using mixed-integer nonlinear model predictive control. *Optimal Control Applications and Methods*, 42(March), 2021.

[15] Mei Cai, Martin S. Ruthkosky, Belabbes Merzougui, Swathy Swathirajan, Michael P. Balogh, and Se H. Oh. Investigation of thermal and electrochemical degradation of fuel cell catalysts. *Journal of Power Sources*, 160(2 SPEC. ISS.):977–986, 2006.

[16] Mauro G. Carignano, Ramon Costa-Castelló, Vicente Roda, Norberto M. Nigro, Sergio Junco, and Diego Feroldi. Energy management strategy for fuel cell-supercapacitor hybrid vehicles based on prediction of energy demand. *Journal of Power Sources*, 360:419–433, 2017.

[17] M. Chandesris, R. Vincent, L. Guetaz, J.-S. Roch, D. Thoby, and M. Quinaud. Membrane degradation in PEM fuel cells: From experimental results to semi-empirical degradation laws. *International Journal of Hydrogen Energy*, pages 1–11, 2017.

[18] Huawei Chang, Zhongmin Wan, Yao Zheng, Xi Chen, Shuiming Shu, Zhengkai Tu, Siew Hwa Chan, Rui Chen, and Xiaodong Wang. Energy- and exergy-based working fluid selection and performance analysis of a high-temperature PEMFC-based micro combined cooling heating and power system. *Applied Energy*, 204:446–458, 2017.

[19] Raphaël Chattot and Sylvie Escribano. Ageing studies of a PEM Fuel Cell stack developed for reformate fuel operation in μCHP units: Development of an accelerated degradation procedure. *International Journal of Hydrogen Energy*, 0:1–8, 2014.

[20] Zhonglin Cheng, Guangchao Geng, Quanyuan Jiang, and Josep M. Guerrero. Energy Management of CHP-Based Microgrid with Thermal Storage for Reducing Wind Curtailment. *Journal of Energy Engineering*, 144(6):04018066, 2018.

[21] Y. Collette and P. Siarry. *Principles and Case Studies*, page 293. Springer-Verlag, 2003.

[22] Susanta K Das and Hilniqua A Gibson. Three dimensional multi-physics modeling and simulation for assessment of mass transport impact on the performance of a high temperature polymer electrolyte membrane fuel cell. *Journal of Power Sources*, 499(March):229844, 2021.

[23] Vipin Das, Sanjeevikumar Padmanaban, Karthikeyan Venkitusamy, Rajasekar Selvamuthukumaran, Frede Blaabjerg, and Pierluigi Siano. Recent advances and challenges of fuel cell based power system architectures and control â A review. *Renewable and Sustainable Energy Reviews*, 73(November 2016):10–18, 2017.

[24] F. A. De Bruijn, V. A T Dam, and G. J M Janssen. Review: Durability and degradation issues of PEM fuel cell components. *Fuel Cells*, 8(1):3–22, 2008.

[25] A. De las Heras, F. J. Vivas, F. Segura, M. J. Redondo, and J. M. Andújar. Air-cooled fuel cells: Keys to design and build the oxidant/cooling system. *Renewable Energy*, 125:1–20, 2018.

[26] S. De Lira, V. Puig, J. Quevedo, and A. Husar. LPV observer design for PEM fuel cell system: Application to fault detection. *Journal of Power Sources*, 196(9):4298–4305, 2011.

[27] Jenny L. Diaz C., Carlos Ocampo-Martinez, Niklas Panten, Thomas Weber, and Eberhard Abele. Optimal operation of combined heat and power systems: An optimization-based control strategy. *Energy Conversion and Management*, 199(April):111957, 2019.

[28] Laetitia Dubau, Luis Castanheira, Frédéric Maillard, Marian Chatenet, Olivier Lottin, Gaël Maranzana, Jérôme Dillet, Adrien Lamibrac, Jean Christophe Perrin, Eddy Moukheiber, Assma Elkaddouri, Gilles De Moor, Corine Bas, Lionel Flandin, and Nicolas Caqué. A review of PEM fuel cell durability: Materials degradation, local heterogeneities of aging and possible mitigation strategies. *Wiley Interdisciplinary Reviews: Energy and Environment*, 3(6):540–560, 2014.

[29] Nikolaos A. Efkarpidis, Styliani A. Vomva, Georgios C. Christoforidis, and Grigoris K. Papagiannis. Optimal day-to-day scheduling of multiple energy assets in residential buildings equipped with variable-speed heat pumps. *Applied Energy*, 312(February):118702, 2022.

[30] Harikishan R. Ellamla, Iain Staffell, Piotr Bujlo, Bruno G. Pollet, and Sivakumar Pasupathi. Current status of fuel cell based combined heat and power systems for residential sector. *Journal of Power Sources*, 293:312–328, 2015.

[31] Theo Elmer, Mark Worall, Shenyi Wu, and Saffa B. Riffat. Fuel cell technology for domestic built environment applications: State of-the-art review. *Renewable and Sustainable Energy Reviews*, 42:913–931, 2015.

[32] Mark Embree. Unstable modes in projection-based reduced-order models: How many can there be, and what do they tell you? *Systems & Control Letters*, 124:49–59, 2017.

[33] Eiji Endoh, Shinji Terazono, Hardiyanto Widjaja, and Yasuyuki Takimoto. Degradation Study of MEA for PEMFCs under Low Humidity Conditions. *Electrochemical and Solid-State Letters*, 7(7):A209–A211, 2004.

[34] Y. M. Ferng, A. Su, and J. Hou. Parametric investigation to enhance the performance of a PBI-based high-temperature PEMFC. *Energy Conversion and Management*, 78:431–437, 2014.

[35] Guillaume Fontès. *Modélisation et caractérisation de la pile PEM pour l 'étude des interactions avec les convertisseurs statiques.* PhD thesis, Institut National Polytechnique de Toulouse, 2005.

[36] Peter J. Gawthrop and Geraint P. Bevan. Bond-graph modelling: A tutorial introduction for control engineers. *IEEE Control Systems Magazine*, 27(2):24–45, 2007.

[37] Sebastien Gros, Damir Jakus, Josip Vasilj, and Mario Zanon. Day-ahead scheduling and real-time economic MPC of CHP unit in microgrid with smart buildings. *IEEE Transactions on Smart Grid*, 10(2):1992–2001, 2019.

[38] Patrick Haase and Bernd Thomas. Test and optimization of a control algorithm for demand-oriented operation of CHP units using hardware-in-the-loop. *Applied Energy*, 294(March):116974, 2021.

[39] Khawaja Shafiq Haider, Abdul Ghafoor, Muhammad Imran, and Fahad Mumtaz Malik. Model Reduction of Large Scale Descriptor Systems Using Time Limited Gramians. *Asian Journal of Control*, 19(3):1217–1227, 2017.

[40] Adam Hawkes, Iain Staffell, Dan Brett, and Nigel Brandon. Fuel cells for micro-combined heat and power generation. *Energy & Environmental Science*, 2(7):729, 2009.

[41] Liangce He, Zhigang Lu, Lili Pan, Hao Zhao, Xueping Li, and Jiangfeng Zhang. Optimal economic and emission dispatch of a microgrid with a combined heat and power system. *Energies*, 12(4), 2019.

[42] Mohammad Hemmati, Mohammad Amin, Mehdi Abapour, and Kazem Zare. Economic-environmental analysis of combined heat and power-based reconfigurable microgrid integrated with multiple energy storage and demand response program. *Sustainable Cities and Society*, 69(September 2020):102790, 2021.

[43] D. Hissel and M.C. Péra. Diagnostic & health management of fuel cell systems: Issues and solutions. *Annual Reviews in Control*, 42:201–211, 2016.

[44] Maximilian Hoffmann, Leander Kotzur, and Detlef Stolten. The Pareto-Optimal Temporal Aggregation of Energy System Models. *Applied Energy*, 315(December 2021):119029, 2021.

[45] Vikas Jaggi and S. Jayanti. A conceptual model of a high-efficiency, stand-alone power unit based on a fuel cell stack with an integrated auto-thermal ethanol reformer. *Applied Energy*, 110:295–303, 2013.

[46] T. Jahnke, G. Futter, A. Latz, T. Malkow, G. Papakonstantinou, G. Tsotridis, P. Schott, M. Gérard, M. Quinaud, M. Quiroga, A. A. Franco, K. Malek, F. Calle-Vallejo, R. Ferreira De Morais, T. Kerber, P. Sautet, D. Loffreda, S. Strahl, M. Serra, P. Polverino, C. Pianese, M. Mayur, W. G. Bessler, and C. Kompis. Performance and degradation of Proton Exchange Membrane Fuel Cells: State of the art in modeling from atomistic to system scale. *Journal of Power Sources*, 304:207–233, 2016.

[47] Fei Jia, Liejin Guo, and Hongtan Liu. Mitigation strategies for hydrogen starvation under dynamic loading in proton exchange membrane fuel cells. *Energy Conversion and Management*, 139:175–181, 2017.

[48] Ahrae Jo, Kyeongmin Oh, Junhee Lee, Donghee Han, Dowan Kim, Jinwook Kim, Bonggyu Kim, Jaedong Kim, Dalryung Park, Minjin Kim, Young-Jun Sohn, Duhee Kim, Hosuk Kim, and Hyunchul Ju. Modeling and analysis of a 5 kWe HT-PEMFC system for residential heat and power generation. *International Journal of Hydrogen Energy*, pages 1–17, 2016.

[49] Shinji Jomori, Nobuaki Nonoyama, and Toshihiko Yoshida. Analysis and modeling of PEMFC degradation: Effect on oxygen transport. *Journal of Power Sources*, 215:18–27, 2012.

[50] Marine Jouin, Mathieu Bressel, Simon Morando, Rafael Gouriveau, Daniel Hissel, Marie-Cécile Péra, Noureddine Zerhouni, Samir Jemei, Mickael Hilairet, and Belkacem Ould Bouamama. Estimating the end-of-life of PEM fuel cells: Guidelines and metrics. *Applied Energy*, 177:87–97, 2016.

[51] Marine Jouin, Rafael Gouriveau, Daniel Hissel, Marie-Cécile Péra, and Noureddine Zerhouni. Prognostics and Health Management of PEMFC - State of the art and remaining challenges. *International Journal of Hydrogen Energy*, 38(35):15307–15317, 2013.

[52] Marine Jouin, Rafael Gouriveau, Daniel Hissel, Marie-Cécile Péra, and Noureddine Zerhouni. Degradations analysis and aging modeling for health assessment and prognostics of PEMFC. *Reliability Engineering and System Safety*, 148:78–95, 2016.

[53] Hyunchul Ju, Hua Meng, and Chao Yang Wang. A single-phase, non-isothermal model for PEM fuel cells. *International Journal of Heat and Mass Transfer*, 48(7):1303–1315, 2005.

[54] Dean Karnopp. Retaining analog intuition in a digital world with bond graphs. *Mathematics and Computers in Simulation*, 53(4-6):219–226, 2000.

[55] Juliane Kätzel, Henning Markötter, Tobias Arlt, Merle Klages, Jan Haußmann, Matthias Messerschmidt, Nikolay Kardjilov, Joachim Scholta, John Banhart, and Ingo Manke. Effect of ageing of gas diffusion layers on the water distribution in flow field channels of polymer electrolyte membrane fuel cells. *Journal of Power Sources*, 301:386–391, 2016.

[56] Jintae Kim, Minjin Kim, Taegon Kang, Young Jun Sohn, Taewon Song, and Kyoung Hwan Choi. Degradation modeling and operational optimization for improving thelifetime of high-temperature PEM (proton exchange membrane) fuel cells. *Energy*, 66:41–49, 2014.

[57] Jintae Kim, Minjin Kim, Bong Gu Lee, and Young Jun Sohn. Durability of high temperature polymer electrolyte membrane fuel cells in daily based start/stop operation mode using reformed gas. *International Journal of Hydrogen Energy*, 40(24):7769–7776, 2015.

[58] A. A. Kulikovsky. The effect of stoichiometric ratio on the performance of a polymer electrolyte fuel cell. *Electrochimica Acta*, 49(4):617–625, 2014.

[59] Deepak Kumar and Victor Sreeram. Factorization-based frequency-weighted optimal Hankel-norm model reduction. *Asian Journal of Control*, 22(December 2017):1–13, 2019.

[60] Hugo Lambert, Robin Roche, Samir Jemeï, Pascal Ortega, and Daniel Hissel. Combined Cooling and Power Management Strategy for a Standalone House Using Hydrogen and Solar Energy. *Hydrogen*, 2(2):207–224, 2021.

[61] Gunn K.H. Larsen, Nicky D. Van Foreest, and Jacquelien M.A. Scherpen. Distributed MPC applied to a network of households with Micro-CHP and heat storage. *IEEE Transactions on Smart Grid*, 5(4):2106–2114, 2014.

[62] Elodie Lechartier, Rafael Gou, Marie-Cécile Péra, and Daniel Hissel. Static and dynamic modeling of a PEMFC for prognostics purpose. *2014 IEEE Vehicle Power and Propulsion Conference (VPPC)*, pages 1–5, 2014.

[63] Elodie Lechartier, Elie Laffly, Marie-Cécile Péra, Rafael Gouriveau, Daniel Hissel, and Noureddine Zerhouni. Proton exchange membrane fuel cell behavioral model suitable for prognostics. *International Journal of Hydrogen Energy*, 40(26):8384–8397, 2015.

[64] Leonard Efrén Dueñas Gutíerrez. *Simulación numérica 3D no-isoterma de una pila de combustible de membrana polimérica de alta temperatura.* PhD thesis, Laboratorio de Investigación en Fluidodinámica y Tecnologías de la Combustión (LIFTEC-CSIC/UZ), 2015.

[65] Dazi Li, Yadi Yu, Qibing Jin, and Zhiqiang Gao. Maximum power efficiency operation and generalized predictive control of PEM (proton exchange membrane) fuel cell. *Energy*, 68:210–217, 2014.

[66] Li Li, Jing Wang, Xiaoyi Zhong, Jian Lin, Nianyuan Wu, Zhihui Zhang, Chao Meng, Xiaonan Wang, Nilay Shah, Nigel Brandon, Shan Xie, and Yingru Zhao. Combined multi-objective optimization and agent-based modeling for a 100% renewable island energy system considering power-to-gas technology and extreme weather conditions. *Applied Energy*, 308(November 2021), 2022.

[67] Zhen Li, Yaolin Jiang, and Kangli Xu. Non-linear model-order reduction based on tensor decomposition and matrix product. *IET Control Theory & Applications*, 12(16):2253–2262, 2018.

[68] Zhongliang Li, Rachid Outbib, Daniel Hissel, and Stefan Giurgea. Control Engineering Practice Data-driven diagnosis of PEM fuel cell : A comparative study. *Control Engineering Practice*, 28:1–12, 2014.

[69] Yongfeng Liu, Werner Lehnert, Holger Janßen, Remzi Can Samsun, and Detlef Stolten. A review of high-temperature polymer electrolyte membrane fuel-cell (HT-PEMFC)-based auxiliary power units for diesel-powered road vehicles. *Journal of Power Sources*, 311:91–102, 2016.

[70] Yannik Löhr, Daniel Wolf, Clemens Pollerberg, Alexander Hörsting, and Martin Mönnigmann. Supervisory model predictive control for combined electrical and thermal supply with multiple sources and storages. *Applied Energy*, 290(February):116742, 2021.

[71] Julio Luna Pacho, Elio Usai, Attila Husar, and Maria Serra Prat. Enhancing the Efficiency and Lifetime of a Proton Exchange Membrane Fuel Cell using Nonlinear Model Predictive Control with Nonlinear Observation. *IEEE Transactions on Industrial Electronics*, 0046(c):1–1, 2017.

[72] Kourosh Malek and Alejandro A. Franco. Microstructure-based modeling of aging mechanisms in catalyst layers of polymer electrolyte fuel cells. *Journal of Physical Chemistry B*, 115(25):8088–8101, 2011.

[73] Michael Mangold, Andreas Bück, and Richard Hanke-Rauschenbach. Passivity based control of a distributed PEM fuel cell model. *Journal of Process Control*, 20(3):292–313, 2010.

[74] Tetsuya Mashio, Hiroshi Iden, Atsushi Ohma, and Takashi Tokumasu. Modeling of local gas transport in catalyst layers of PEM fuel cells. *Journal of Electroanalytical Chemistry*, 790:27–39, 2017.

[75] Behzad Najafi, Alireza Haghighat Mamaghani, Fabio Rinaldi, and Andrea Casalegno. Long-term performance analysis of an HT-PEM fuel cell based micro-CHP system: Operational strategies. *Applied Energy*, 147:582–592, 2015.

[76] Santiago Navarro Gimenez, Juan Manuel Herrero Dura, Francesc Xavier Blasco Ferragud, and Raul Simarro Fernandez. Control-Oriented Modeling of the Cooling Process of a PEMFC-Based $$ -CHP System. *IEEE Access*, 7:95620–95642, 2019.

[77] Wolfgang Neubrand. *Modellbildung und Simulation von Elektromembranverfahren*. PhD thesis, Institut für Chemische Verfahrenstechnik der Universität Stuttgart, 1999.

[78] D A Notter, K Kouravelou, T Karachalios, M K Daletou, and N T Haberland. Life cycle assessment of PEM FC applications: Electric mobility and μ-CHP. *Energy and Environmental Science*, 8(7):1969–1985, 2015.

[79] B. Ould Bouamama, G. Dauphin-Tanguy, M. Staroswiecki, and D. Del Amo Bravo. Bond-Graph Analysis of Structural FDI Properties in Mechatronics System. *IFAC Proceedings Volumes*, 33(26):989–994, 2017.

[80] Alberto Pajares, Xavier Blasco, Juan M. Herrero, and Raúl Simarro. Multivariable Controller Design for the Cooling System of a PEM Fuel Cell by considering Nearly Optimal Solutions in a Multiobjective Optimization Approach. *Complexity*, 2020, 2020.

[81] Julio Pascual, Diego Arcos-Aviles, Alfredo Ursúa, Pablo Sanchis, and Luis Marroyo. Energy management for an electro-thermal renewableâbased residential microgrid with energy balance forecasting and demand side management. *Applied Energy*, 295:117062, 2021.

[82] Marina Petrelli, Davide Fioriti, Alberto Berizzi, Cristian Bovo, and Davide Poli. A novel multi-objective method with online Pareto pruning for multi-year optimization of rural microgrids. *Applied Energy*, 299(February):117283, 2021.

[83] R. Petrone, D. Hissel, M. C. Péra, D. Chamagne, and R. Gouriveau. Accelerated stress test procedures for PEM fuel cells under actual load constraints: State-of-art and proposals. *International Journal of Hydrogen Energy*, 40(36):12489–12505, 2015.

[84] Piotr Piela and Jens Mitzel. Polymer electrolyte membrane fuel cell efficiency at the stack level. *Journal of Power Sources*, 292:95–103, 2015.

[85] I. Pontes Duff, C. Poussot-Vassal, and C. Seren. H2-optimal model approximation by input/output-delay structured reduced order models. *Systems and Control Letters*, 117:60–67, 2018.

[86] Julien Ramousse, Olivier Lottin, Sophie Didierjean, and Denis Maillet. Heat sources in proton exchange membrane (PEM) fuel cells. *Journal of Power Sources*, 192(2):435–441, 2009.

[87] Christophe Robin, Mathias Gerard, Alejandro A. Franco, and Pascal Schott. Multi-scale coupling between two dynamical models for PEMFC aging prediction. *International Journal of Hydrogen Energy*, 38(11):4675–4688, 2013.

[88] Vicente Roda and Paul F Puleston. Thermal Dynamic modelling for a highâtemperature PEM fuel cell. *IV Symposium on Hydrogen, Fuel Cells and Advanced Batteries, HYCELTEC 2013*, 2:911767, 2011.

[89] R J Romero, S A Serna Barquera, A Rodríguez Martínez, S Silva Sotelo, M A Cruz Chavez, M A Basurto Pensado, J C García, and J A Rodríguez. Waste Heat Revalorization with Electric Generation Based on Fuel Cell. *American Journal of Environmental Engineering*, 4(4A):11–18, 2014.

[90] R. E. Rosli, A. B. Sulong, W. R.W. Daud, M. A. Zulkifley, T. Husaini, M. I. Rosli, E. H. Majlan, and M. A. Haque. A review of high-temperature proton exchange membrane fuel cell (HT-PEMFC) system. *International Journal of Hydrogen Energy*, 42(14):9293–9314, 2017.

[91] Marek Rydel and Rafał Stanisławski. A new frequency weighted Fourier-based method for model order reduction. *Automatica*, 88:107–112, 2018.

[92] Marcelo Salgado, Matias Negrete-Pincetic, Álvaro Lorca, and Daniel Olivares. A low-complexity decision model for home energy management systems. *Applied Energy*, 294(September 2020):116985, 2021.

[93] Giordano Scarciotti and Alessandro Astolfi. Nonlinear Model Reduction by Moment Matching. *Foundations and Trends® in Systems and Control*, 4(3-4):224–409, 2017.

[94] Wolfgang Schmittinger and Ardalan Vahidi. A review of the main parameters influencing long-term performance and durability of PEM fuel cells. *Journal of Power Sources*, 180(1):1–14, 2008.

[95] M Schultze, C Hähnel, and J Horn. Nonlinear Model Predictive Control of a PEM Fuel Cell System for Cathode Exhaust Gas Generation. *IFAC Proceedings Volumes*, 47(3):9432–9437, 2014.

[96] Yuyao Shan and Song-Yul Choe. A high dynamic PEM fuel cell model with temperature effects. *Journal of Power Sources*, 145(1):30–39, 2005.

[97] Yuyan Shao, Geping Yin, and Yunzhi Gao. Understanding and approaches for the durability issues of Pt-based catalysts for PEM fuel cell. *Journal of Power Sources*, 171(2):558–566, 2007.

[98] Ahmed Azmi Sherif Imam. Sizing and Economic Analysis of Standalone PEM Fuel Cell Systems for Residential Utilization. *International Review of Applied Sciences and Engineering*, 2(1):1–10, 2015.

[99] Jason B. Siegel. Experiments and Modeling of PEM Fuel Cells for Dead-Ended Anode Operation. *PhD Thesis*, pages 1–77, 2010.

[100] Young-Jun Sohn, Sung-Dae Yim, Gu-Gon Park, Minjin Kim, Suk-Won Cha, and Kyoungyoun Kim. PEMFC modeling based on characterization of effective diffusivity in simulated cathode catalyst layer. *International Journal of Hydrogen Energy*, pages 2–9, 2017.

[101] S. Sondergaard, L.N. Cleemann, J.O. Jensen, and N.J. Bjerrum. Influence of carbon monoxide on the cathode in high-temperature polymer electrolyte membrane fuel cells. *International Journal of Hydrogen Energy*, 42(5):1–7, 2017.

[102] D. A. Stevens and J. R. Dahn. Thermal degradation of the support in carbon-supported platinum electrocatalysts for PEM fuel cells. *Carbon*, 43(1):179–188, 2005.

[103] J. Torreglosa, P. Garcia, L. Fernandez, and F. Jurado. Predictive Control for the Energy Management of a Fuel Cell-Battery-Supercapacitor Tramway. *IEEE Transactions on Industrial Informatics*, 10(1):1–1, 2013.

[104] Xing Jin, Ashish P Vora, Vaidehi Hoshing, Tridib Saha, Gregory M Shaver, Oleg Wasynczuk, and Subbarao Varigonda. Comparison of Li-ion battery degradation models for system design and control algorithm development. *2017 American Control Conference (ACC)*, 4(February 2017):74–79, 2017.

[105] Ting Yang, Liyuan Zhao, Wei Li, Jianzhong Wu, and Albert Y. Zomaya. Towards healthy and cost-effective indoor environment management in smart homes: A deep reinforcement learning approach. *Applied Energy*, 300(March):117335, 2021.

[106] N. Yousfi-Steiner, P. Moçotéguy, D. Candusso, and D. Hissel. A review on polymer electrolyte membrane fuel cell catalyst degradation and starvation issues: Causes, consequences and diagnostic for mitigation. *Journal of Power Sources*, 194(1):130–145, 2009.

[107] Caizhi Zhang, Tao Yu, Jun Yi, Zhitao Liu, Kamal Abdul Rasheedj Raj, Lingchao Xia, Zhengkai Tu, and Siew Hwa Chan. Investigation of heating and cooling in a stand-alone high temperature PEM fuel cell system. *Energy Conversion and Management*, 129:36–42, 2016.

[108] Yan Zhang, Fanlin Meng, Rui Wang, Behzad Kazemtabrizi, and Jianmai Shi. Uncertainty-resistant stochastic MPC approach for optimal operation of CHP microgrid. *Energy*, 179:1265–1278, 2019.